STUDIES ON THE EFFECT OF MAGNETIC FIELD INDUCED AGGREGATION ON PHYSICAL PROPERTIES OF FERROFLUIDS

By

SITHARA VINOD

PHYS 02 2014 04 001

Indira Gandhi Centre for Atomic Research, Kalpakkam
Tamil Nadu, India 603102

A thesis submitted to the

Board of Studies Physical Sciences

In partial fulfillment of requirements

for the Degree of

DOCTOR OF PHILOSOPHY

of

HOMI BHABHA NATIONAL INSTITUTE

August, 2019

Homi Bhabha National Institute

Recommendations of the Viva Voce Committee

As members of the Viva Voce Committee, we certify that we have read the dissertation prepared by Sithara Vinod entitled "Studies on the effect of magnetic field induced aggregation on physical properties of ferrofluids" and recommend that it may be accepted as fulfilling the thesis requirement for the award of Degree of Doctor of Philosophy.

Chairman – Dr. T. R. Ravindran	T R Ravindran	Date 21/2/2020
Guide / Convener – Dr. John Philip	John Philip	Date 21.02.2020
Examiner – Dr. K. G. Suresh	Viva by Video conferencing (Dean, PS)	Date 21/02/2020
Member 1 – Dr. D. Ponraju	D. Ponraju	Date 21/2/2020
Member 2 – Dr. R. Ramaseshan	R. Ramaseshan	Date 21/2/20
Member 3 – Dr. S. Ningshen	S. Ningshen	Date 21/02/2020

Final approval and acceptance of this thesis is contingent upon the candidate's submission of the final copies of the thesis to HBNI.

I/We hereby certify that I/we have read this thesis prepared under my/our direction and recommend that it may be accepted as fulfilling the thesis requirement.

Date: 21.02.2020

Place: Kalpakkam

Signature

Guide John Philip

Homi Bhabha National Institute

Recommendations of the Viva Voce Committee

As members of the Viva Voce Committee, we certify that we have read the dissertation prepared by Sithara Vinod entitled "Studies on the effect of magnetic field induced aggregation on physical properties of ferrofluids" and recommend that it may be accepted as fulfilling the thesis requirement for the award of Degree of Doctor of Philosophy.

Chairman – Dr. T. R. Ravindran	T R Ravindran	Date 21/2/2020
Guide / Convener – Dr. John Philip	John Philip	Date 21.02.2020
Examiner – Dr. K. G. Suresh	Viva by Video conferencing (Dean, PS)	Date 21/02/2020
Member 1 – Dr. D. Ponraju	D. Ponraju	Date 21/2/2020
Member 2 – Dr. R. Ramaseshan	R. Ramaseshan	Date 21/2/20
Member 3 – Dr. S. Ningshen	S. Ningshen	Date 21/02/2020

Final approval and acceptance of this thesis is contingent upon the candidate's submission of the final copies of the thesis to HBNI.

I/We hereby certify that I/we have read this thesis prepared under my/our direction and recommend that it may be accepted as fulfilling the thesis requirement.

Date: 21.02.2020

Place: Kalpakkam

Signature

Guide John Philip

STATEMENT BY AUTHOR

This dissertation has been submitted in partial fulfillment of requirements for an advanced degree at Homi Bhabha National Institute (HBNI) and is deposited in the Library to be made available to borrowers under rules of the HBNI.

Brief quotations from this dissertation are allowable without special permission, provided that accurate acknowledgement of source is made. Requests for permission for extended quotation from or reproduction of this manuscript in whole or in part may be granted by the Competent Authority of HBNI when in his or her judgment the proposed use of the material is in the interests of scholarship. In all other instances, however, permission must be obtained from the author.

21/2/2020

(Sithara Vinod)

DECLARATION

I, hereby declare that the investigation presented in the thesis has been carried out by me. The work is original and has not been submitted earlier as a whole or in part for a degree / diploma at this or any other Institution / University.

21/2/2020

(Sithara Vinod)

List of Publications arising from the thesis

Journals

1. "Impact of field ramp rate on magnetic field assisted thermal transport in ferrofluids", Sithara Vinod, John Philip, *J. Mol. Liq.*, **2020**, *298*, 112047.

2. "Field induced deformation of sessile ferrofluid droplets: Effect of particle size distribution on magnetowetting", Sithara Vinod, John Philip, *J. Magn. Magn. Mater.*, **2018**, *466*, 295-300.

3. "Experimental evidence for the significant role of initial cluster size and liquid confinement on thermo-physical properties of magnetic nanofluids under applied magnetic field", Sithara Vinod, John Philip, *J. Mol. Liq.*, **2018**, *257*, 1-11.

4. "Role of field-induced nanostructures, zippering and size polydispersity on effective thermal transport in magnetic fluids without significant viscosity enhancement", Sithara Vinod, John Philip, *J. Magn. Magn. Mater.*, **2017**, *444*, 29-42.

5. "Observation of soft glassy dynamics in a magnetic colloid during fast magnetic field quenches", Sithara Vinod, John Philip, Philip J. Camp, *under review*.

Conferences

1. *"*Probing effect of magnetic field ramp rate on aggregation kinetics of a ferrofluid using rheology", Sithara Vinod and John Philip, *at Compflu,* organized by IIT Madras, Chennai, India during *18-20 December, 2017.*

2. *"*Role of field induced nanostructures and polydispersity on effective thermal transport in magnetic fluids", Sithara Vinod and John Philip, *at ISAN,* organized by Madras University, Chennai, India during *27-28 February, 2018.*

*3. "*Magnetic field tunable thermal transport in ferrofluids: Effect of polydispersity", Sithara Vinod and John Philip *at COMPFLU,* organized by IIT, Roorkee, India during *06-09 December, 2018.*

4. Indo-US Workshop on Soft Matter (IUWSM) at IIT Roorkee, during 9-11, December

Other publications not included in the thesis

1. "Magnetorheological properties of sodium sulphonate capped electrolytic iron based MR fluid: a comparison with CI based MR fluid", Sithara Vinod, Reji John, John Philip, *Smart Mater. Struct.*, **2017**, *26*, 025003.

2. "Stability and rheological property of γ-Al_2O_3 nanofluid with cationic polyelectrolyte additive", R. Kiruba, Sithara Vinod, A. W. Zaibudeen, R. Vijay Solomon, John Philip, *Colloids Surf. A,* **2018**, *555*, 63-71.

3. "Recent Advances in Magnetorheology of Ferrofluids (Magnetic Nanofluids)—A Critical Review", Leona J. Felicia, Sithara Vinod, John Philip, *J. Nanofluids*, **2016**, *5*, 1-22.

4. "Effect of initial susceptibility and relaxation dynamics on radio frequency alternating magnetic field induced heating in superparamagnetic nanoparticle dispersions", Surojit Ranoo, B. B. Lahiri, Sithara Vinod, John Philip, *J. Magn. Magn. Mater.*, **2019,** *486*, 165267.

5. "Synthesis, characterization, thermal conductivity and rheological studies in magnetite-decorated graphene oxide nanofluids", G. Vinodha, L. Cindrella, Sithara Vinod, John Philip, P. D. Shima, *J. Nanofluids*, **2018**, *7*, 11-20.

21/2/2020

(Sithara Vinod)

DEDICATIONS

To my Parents, Leena Vinod and Vinod Kumar,

and husband, Gautam Ravi.

I am forever grateful for your love, support and encouragement.

ACKNOWLEDGEMENTS

First and foremost, I express my deepest gratitude to my advisor, Dr. John Philip, for his guidance and insightful suggestions. I'm grateful to him for motivating me to aim higher and for being understanding and patient with me throughout my PhD tenure. I am thankful to him for giving me independence to pursue my ideas and at the same time preventing me from wasting time on infeasible ones.

I am extremely thankful to my doctoral committee chairman, Dr. T. R. Ravindran and members, Dr. D. Ponraju, Dr. S. Ningshen and Dr. R. Ramaseshan for their insightful comments and kind words of encouragement. I also thank my former doctoral committee members, particularly Dr. B. V. R. Tata, for their valuable suggestions.

I thank Dr. A. K. Bhaduri, Director of IGCAR, and Dr. G. Amarendra, Director of Metallurgy and Materials Group, for giving me the opportunity to carry out research at Indira Gandhi Centre for Atomic Research (IGCAR). I express my gratitude to all the former centre Directors for their support.

I thank all members of SMART section for their help and encouragement. I am particularly thankful to Dr. Leona J. Felicia for training me in rheology and for her valuable suggestions. I thank all the research scholars of SMART section and my batch mates for all the fun and lively discussions we had.

Last, but not the least, I thank my parents, brother and sister, my husband and parents-in-law for their love, encouragement and prayers. I am forever in your debt for everything you have done for me. I thank my brother, Sachin Vinod, for carefully proof reading my thesis.

CONTENTS

LIST OF FIGURES

LIST OF TABLES

LIST OF ABBREVIATIONS

DNA	Deoxyribonucleic acid
Fig.	Figure
Eqn.	Equation
vol.%	Volume percentage
MVE	Magnetoviscous effect
wt.%	Weight percentage
CSR	Controlled shear rate
CSS	Controlled shear stress
XRD	X-ray diffraction
JCPDS	Joint Committee on Powder Diffraction Standards
DLS	Dynamic light scattering
VSM	Vibrating sample magnetometer
TGA	Thermogravimetric analysis
CCD	Charge coupled device
LED	Light-emitting diode
SAM	Self assembled monolayer
H-S	Hashin-Shtrikman
LVE	Linear viscoelastic
PDI	Polydispersity index

LIST OF SYMBOLS

k_B	Boltzmann constant
T	Temperature
L_{side}	Length of cube
l	Displacement
G	Shear modulus
τ	Shear stress
T_B	Blocking temperature
m	Magnetic moment
H	Magnetic field strength
d	Diameter of the particle
χ	Magnetic susceptibility
$\tau_{Brownian}$	Brownian relaxation time
η_c	Viscosity of the base fluid
V_H	Hydrodynamic volume
τ_{Neel}	Neel relaxation time
τ_0	Attempt time
K	Effective uniaxial anisotropy energy density
V_p	Volume of the particle
τ_{eff}	Effective relaxation time
U_{ij}	Magnetic interaction energy between particles i and j
μ_0	Absolute magnetic permeability
r_{ij}	Distance between particles i and j
N^*	Aggregation parameter
Φ	Volume fraction
mf	Mass fraction
ρ_{bf}	Density of base fluid
ρ_p	Density of particle

λ	Magnetic coupling constant for a monodisperse ferrofluid
$\langle l_{chain} \rangle$	Average chain length
t	Time
$t_{critical}$	Cross-over time between tip-to-tip aggregation and lateral coalescence
ρ	Lateral distance between the chains
$\frac{dN_k}{dt}$	Rate of change in the number of aggregates containing k particles
K_{ij}	Reaction kernel
N_i	Number of aggregates containing i particles
J	Particle flux towards the aggregate
N	Number of particles in the aggregate
V	Volume of the aggregate
n_i	Number of particles within an aggregate
n_s	Number of particles near the vicinity of the aggregate
V_c	Critical volume of nuclei
v	Volume of a single particle
Φ_{dilute}	Volume fraction of particles in the dilute phase in the vicinity of an aggregate
Φ_{dense}	Volume fraction of particles within an aggregate
Δ	Supersaturation
Φ_∞	Volume fraction of particles far away from the aggregate
σ	Interfacial tension
S	Surface area of the aggregate
Λ	Magnetic coupling constant for a polydisperse ferrofluid
M_i	Number of particles having magnetic moment m_i
$\chi_{polydisperse}$	Magnetic susceptibility of polydisperse ferrofluid
χ_L	Langevin susceptibility
η	Viscosity of the ferrofluid
η_c	Viscosity of the base fluid
α	Angle between the direction of applied magnetic field and the angular velocity of rotation

Ω	Angular velocity of rotation
F_M	Magnetic force between two dipoles
M_0	Spontaneous magnetization
$d_{hydrodynamic}$	Hydrodynamic diameter of particle
F_H	Hydrodynamic c force
$\dot{\gamma}$	Shear rate
N_{max}	Maximum number of particles in a chain
D	Diffusion coefficient
Mn	Mason number
μ_c	Relative magnetic permeability of the base fluid
$\langle M_p \rangle$	Mean magnetization of the dispersed phase
η_F	Field specific viscosity
η_∞	Infinite shear viscosity in the absence of magnetic field
τ	Shear stress
τ_y	Yield stress
η_{Casson}	Casson viscosity
K'	Consistency index
n	Degree of shear thinning
M_s	Saturation magnetization
k	Effective thermal conductivity of the suspension
k_f	Thermal conductivity of the base fluid
k_p	Thermal conductivity of the nanoparticle
θ_C	Contact angle
Υ_{LG}	Interfacial tension between liquid-gas
Υ_{SG}	Interfacial tension between solid-gas
Υ_{SL}	Interfacial tension between solid-liquid
N_B	Magnetic Bond number
R	Diameter of the droplet
Υ	Surface tension of the droplet

F	Shear force applied per unit area
A	Area of the rheometer shearing plate
v	Velocity of the upper plate
h	Gap height between rheometer plates
γ	Strain
ω	Oscillation frequency of applied strain
γ_0	Amplitude of the applied strain
δ	Phase lag
G'	Storage or elastic modulus
$G"$	Loss or viscous modulus
G^*	Complex shear modulus
R_{plate}	Radius of the shearing plate
α_{cone}	Cone angle of cone and plate geometry
R_i	Radius of the inner rotating cylinder of the concentric cylinder geometry
R_o	Radius of the outer cup of the concentric cylinder geometry
d_{hkl}	Spacing between lattice planes
θ	Bragg angle
n	Order of Bragg reflection
λ_{X-ray}	Wavelength of X-ray
$d_{crystallite}$	Crystallite size
β_{FWHM}	Full width at half maximum
$g^{(2)}(q,t)$	Intensity correlation function
q	Wave vector
$I(q,t)$	Scattered intensity at time t
$I(q,t+\delta t)$	Scattered intensity at time $t+\delta t$.
$g^{(1)}(q,t)$	Electric field correlation function
β'	Correction factor
Γ	Rate of relaxation
a_s	Head area of a single surfactant molecule

N_0	Avogadro number
ρ	Density of magnetite nanoparticle
M	Molecular weight of oleic acid
$V_{aggregate}$	Volume of aggregate
a'	Semi-major axis of ellipse
b'	Semi-minor axis of ellipse
J_Q	Heat flux across the interface
ΔT	Temperature drop across the interface
G_k	Kapitza conductance
R_{vib}	Vibrational relaxation rate
$\rho_{r',r"}$	Density of states
r'	Initial state of the vibrational mode that accepted energy
$r"$	Final state of the vibrational mode that accepted energy
σ'	Initial state of the excited vibrational mode
$\sigma"'$	Final state of the excited vibrational mode
$k^=$	Effective thermal conductivity in series mode of conduction
$k^{\parallel}$	Effective thermal conductivity in parallel mode of conduction
η_0	Viscosity in the absence of magnetic field
η_r	Relative increase in viscosity
k_r	Relative increase in thermal conductivity
τ_l	Time scale of lateral coalescence
η_∞	Field independent high shear viscosity
Φ_{max}	Maximum packing fraction
Mn^*	Critical Mason number
τ_m	Microscopic relaxation time associated with aging
μ'	Positive exponent
t_w	Waiting time
J	Creep compliance
τ_0	Constant relaxation time

E_S	Surface energy of a prolate ellipsoid
K'	Aspect ratio of elliptical droplet
a_d	Semi-major axis of the ellipsoidal droplet
ε'	Eccentricity of ellipsoidal droplet
E_M	Magnetic energy of ferrofluid droplet
V_{drop}	Volume of the elliptical droplet

Chapter 7 Conclusions and recommendations for future work

7.1 Summary and conclusions

The effect of field induced aggregation dynamics on thermal, rheological and wetting properties of oil-based ferrofluids that are similar in chemical composition and volume fraction but differ in their size distribution was studied systematically. The important results are summarized below.

Particle size distribution was found to drastically affect field tunable thermal conductivity and rheology of ferrofluids. Ferrofluid containing nanoparticles with most probable hydrodynamic size 11.6 nm and PDI 0.225 gave the highest enhancement in thermal conductivity with minimal viscosity enhancement while another ferrofluid composed of particles with most probable hydrodynamic size 21 nm and PDI 0.79 did not show notable enhancement in field tunable thermal conductivity but displayed pronounced increase in viscosity with increasing field strength. This drastic difference in thermal and rheological properties of ferrofluids is due to differences in field induced aggregation brought about by difference in particle size distribution. Narrow size distribution, without large aggregates, results in the occurrence of nucleation, the first step towards chain/column formation, over longer time scales and at higher field strengths owing to larger energy barrier height for aggregation because of lower dipolar interaction. Additionally, presence of modest amount of smaller particles prevented extensive zippering transitions. Thereby, the reduction of heat conducting pathways is averted. In the optical microscopy images, even for field strengths as high as 625 G, observable aggregates were absent in ferrofluids with narrow size distribution without large aggregates, confirming that most of the aggregates were nanosized. At the same time, in such systems

notable viscosity enhancement was not observed as the field induced aggregates are fine. In ferrofluid systems with sizeable portion of larger particles, the nucleation stage is very short as the large particles themselves act as nucleation centers and micron sized aggregates were observed even at low field strengths in the optical microscopy images. Extensive zippering transitions lead to drastic decrease in the number density of aggregates and thermal conductivity did not show substantial improvement with increasing magnetic field strength. However, owing to the thick gap spanning columnar aggregates, viscosity enhancement in the polydisperse system was high with measurable yield stress. These results imply that by tailoring the particle size distribution efficient heat transfer can be achieved without viscosity enhancement and ferrofluids can serve as excellent coolants without increasing pumping power.

Magnetic field ramp rate is one of the factors influencing aggregation kinetics that has not received much attention. Faster magnetic field ramps results in simultaneous formation of large number density of fine aggregates which was found to improve field tunable thermal conductivity of ferrofluids owing to the large number density of aggregates. Slower ramps on the other hand, resulted in the formation of thicker aggregates via extensive zippering transitions than a fast ramp, leading to drastic reduction in the number density of aggregates. On sudden exposure to magnetic field, particularly for higher strengths, substantial improvement in thermal conductivity was observed in initially, though with time zippering transitions reduced the number density of chains and thermal conductivity decreased. However, for fast ramps, even after a time period of 30 min., thermal conductivity was still higher than the corresponding value obtained for a slow ramp rate. For higher field strengths, faster ramps was found to be more beneficial for thermal transport and for avoiding the decrease in thermal conductivity with time, alternate magnetic field on-off cycles was found to be effective. Additionally, with faster ramps

thermal conductivity in a system with moderate amount of larger particles can be significantly improved from the values obtained during slower ramps.

The applied magnetic field ramp rate, in addition to influencing field tunable thermal transport, significantly impacted rheological properties of ferrofluids as the microstructure was found to be very different for slow and fast field quenches. Slower field quench rates resulted in a microstructure of higher yield stress composed of very coarse long aggregates while fast quenches led to the formation of thinner and shorter aggregates, denied of the time to settle into lower energy states and thereby existing in a frustrated metastable configuration like a repulsive glass. For the fastest field quench the frequency sweep measurement showed a fast relaxation which is tentatively assigned to local mobility of aggregates in a spatially heterogeneous configuration. For slower ramp durations, such a relaxation could not be seen within the accessible experimental window, though there are clear indications of imminent crossovers at lower frequencies. Fast field quench leads to the buildup of internal stresses, giving rise to faster dynamics, and hence relaxation is shifted to lower frequency with increase in quench duration. In the presence of magnetic field, under fast field quenches, ferrofluid was found to disobey time translational invariance and underwent aging with continuous evolution of microstructure as a result of which strain response to constant stress and creep compliance became a function of the waiting time before the beginning of rheological test. However, when the curves are scaled with respect to an effective time domain, time translational invariance was recovered, just like other soft glassy materials. For longer ramp duration, the microstructure is closer to equilibrium and hence the exponent used for scaling the time domain to an effective time domain was found to be smaller than for faster ramps.

Wetting behavior of ferrofluids in the presence of external magnetic field was found to be affected by aggregation dynamics. In ferrofluids containing significant fraction of large particles, only a slight initial decrease in contact angle with increasing magnetic field strength was observed, owing to lower aggregate-base fluid interaction brought about by extensive zippering transitions that reduce the number density of aggregates drastically. Ferrofluids with narrow size distribution without large aggregates, showed a steady decrease in contact angle with increasing field strength owing to the slower aggregation kinetics without extensive zippering transitions, due to which the number density of aggregates was high enough so as to not mask the interaction between the aggregates and the base fluid.

The findings of this thesis provide better insight into the effect of aggregation dynamics on thermal, rheological and wetting properties of ferrofluids exposed to an external magnetic field and consequently will aide in better utilization of ferrofluids in various technological applications.

7.2 Recommendations for future work

Few recommendations for future work are given below.

- A detailed study on the effect of liquid confinement on thermal conductivity of ferrofluids by experimentally measuring the vibrational relaxation times using optical pump-probe techniques at different magnetic field strengths.
- To probe the impact on magnetic field tunable thermo-rheological properties of ferrofluids incorporated with various additives.

- To develop hybrid ferrofluids that respond to multiple stimuli like temperature or pH in addition to magnetic field, and study the effect of external stimuli on thermo-rheological properties.
- To probe aging in ferrofluids using rheology as a function of volume fraction, magnetic field strength and particle size.
- To study magnetic field induced deformation of ferrofluid droplet as a function of particle concentration, particle size, nature of base fluid and magnetic field strength.
- To develop nanoparticle-polymer composites and magnetic gels and study their field tunable physical properties.

SUMMARY

Ferrofluids are colloidal dispersions of surface modified magnetic nanoparticles (5 – 20 nm). They exhibit interesting rheological, thermal, optical and wetting properties in response to a magnetic field due to aggregation of the magnetic nanoparticles into chains/columns. In general, magnetic field induced aggregation is a reversible process, but is a highly complex phenomenon owing to dependence on multiple variables like magnetic field strength, particle size distribution, temperature etc. The magnetic field tunable changes in physical properties of ferrofluids have inspired many applications and a thorough understanding of field induced aggregation is a prerequisite for effective utilization of ferrofluids.

The main focus of this thesis is to study the effect of particle size distribution on magnetic field induced aggregation in ferrofluids and the subsequent changes in thermo-rheological and wetting properties. Different oil-based ferrofluids of same chemical composition and volume fractions but with different size distributions were synthesized and field induced aggregation was studied. Differences in particle size distribution resulted in drastic difference in field induced microstructure. Ferrofluids containing large aggregates displayed very fast aggregation kinetics with extensive zippering transitions even for relatively low magnetic field strengths resulting in the formation of large micron sized field induced aggregates. In ferrofluids with narrow size distribution without large particles, tip-to-tip aggregation and zippering transitions occur over longer time scales and at higher field strengths owing to larger barrier height for aggregation due to the low dipolar interaction of small particles. The variation in field induced microstructure was reflected in the physical properties.

Ferrofluids with narrow size distribution and without large aggregates, displayed significant enhancement in thermal conductivity in the presence of magnetic field with negligible

viscosity enhancement, owing to the large number density of aggregates. On the other hand, highly polydisperse ferrofluids containing large aggregates, showed very fast aggregation kinetics, leading to the formation of long, coarse aggregates that resulted in drastic reduction in their number density, where the enhancement in thermal conductivity in the presence of magnetic field was modest but the enhancement in viscosity was huge. Additionally, aggregation kinetics affected spreading of ferrofluid droplets on a solid substrate. In polydisperse systems, extensive zippering transitions brought about by larger aggregates reduced particle-base fluid interaction and hence the variation of contact angle with increasing magnetic field strength was not prominent. Significant decrease in contact angle with increasing magnetic field was observed for relatively monodisperse ferrofluids without large aggregates as the number density of aggregates are high enough to ensure strong particle-base fluid interaction.

Magnetic field ramp rate was found to have a profound influence on thermal and rheological properties. Faster ramps result in simultaneous formation of large number density of aggregates which was found to be beneficial for effective thermal transport. On the other hand, slower ramps lead to the formation of thicker aggregates with higher yield stress. Interestingly, when subjected to fast field quenches at sufficiently high magnetic field strengths, ferrofluids disobey time translational invariance and exhibit aging owing to structural arrest of field induced aggregates resulting in a frustrated metastable configuration similar to a repulsive glass.

The findings of this thesis provide better insight into the effect of aggregation dynamics on thermal, rheological and wetting properties of ferrofluids exposed to an external magnetic field that will aide in better utilization of ferrofluids in various technological applications.

Chapter 1 Introduction

1.1 Soft Matter

Soft matter includes a wide variety of materials that give "a large response to small perturbations"[1]. They involve materials that are neither crystalline solids nor simple liquids[2]. A large class of materials comes under soft matter including food items like ketchup, mayonnaise, dough etc., day to day essentials like shampoo, shaving cream etc., biologically important materials like DNA, proteins, cell membranes etc. and other widely used materials like glue, varnish, paints, rubber etc. All these materials fall in categories like colloids, surfactants, liquid crystals, polymers etc[3]. Schematic showing certain soft materials is shown in **Fig. 1.1**. The length scale of soft materials comes under the mesoscopic scale (1 nm - 1 μm) and their material properties differ from that of simple liquids or solids. The relaxation time scale of soft materials lies within the range of 10 ns – several minutes. For non-equilibrium complex fluids, relaxation time can be of the order of years[4].

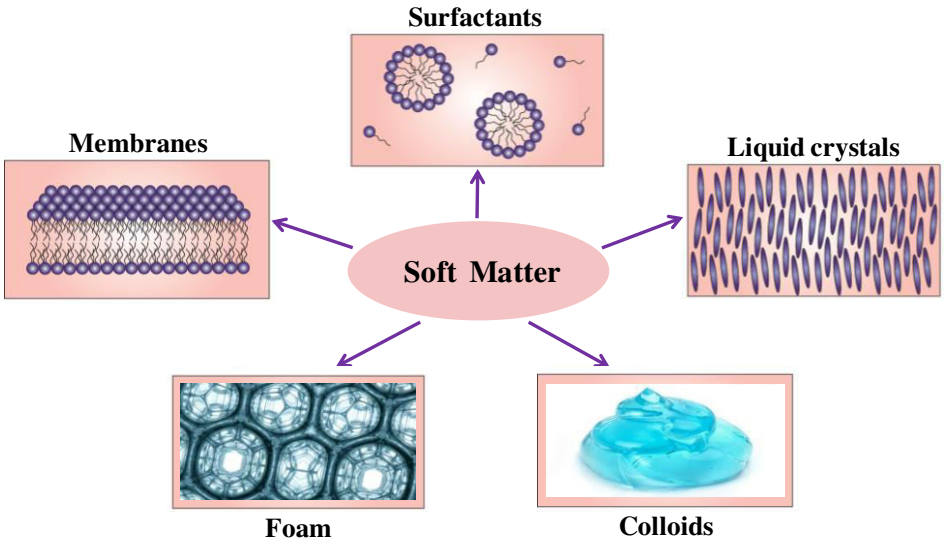

Figure 1.1: Schematic showing some examples of soft matter.

One distinction between soft and hard matter is that in the former molecular energy is close to k_BT (k_B – Boltzmann constant, T – temperature) and in the latter molecular energy is much larger than k_BT [3]. Consequently soft materials are easy to deform as their structural units, that are much larger than atoms, are held together by weak intermolecular interactions that can be easily modified by energies close to k_BT. If a material, in the shape of a cube of dimension L_{side}, is subjected to a small shear strain resulting in a displacement l, then the shear modulus is given by $G = {}^{\tau L_{side}}/_{l}$, where τ is the shear stress[5]. For solids like metals and hard plastics, $G \simeq 10^{11}$ Pa, while for soft materials like gels, $G \simeq 10^{2}$ Pa and for colloids, $G \simeq 10^{-3} - 1$ Pa[4, 5]. Shear modulus of certain materials are indicated in **table 1.1**.

Table 1.1: Values of shear modulus of some materials[6]

Material	Shear modulus
Spray coatings, salad dressings	5 - 10 Pa
Brush coatings	10 - 50 Pa
Lotions, creams	50 - 5000 Pa
Soft natural gums	0.03 - 0.3 MPa
Hard rubbers	10 - 100 MPa
Thermoplastic polymers	0.1 - 2 GPa
Pure resin	1 - 2 GPa
Ice	3.7 GPa
Gold	28 GPa
Steel	80 GPa

Different types of soft matter have features that are common to each other, in addition to certain features that are unique to them. The most important common feature of all soft matter is the lack of crystalline order. The structural units of soft matter display collectivity, leading to slow and nonequilibrium responses[7]. The typical response time of simple liquids is around 10^{-9} s. For soft materials like glasses, response time can be billion or more times longer than simple

liquids. Another characteristic of soft materials is that their phase transitions are 'weak' first order transitions where the enthalpy or entropy change is small and can be described by Landau theory which is based on the expansion of free energy as a power series of an order parameter. Knowledge of the effective interparticle interactions is crucial for understanding and predicting the material properties of soft matter[8]. Some of the most common interactions include van der Waals interaction, coulomb interaction, hard sphere repulsion etc. Some of the experimental techniques used for investigating soft matter are microscopy, scattering methods, rheology, spectroscopic methods, calorimetry and surface structure probes[3].

Certain soft materials, popularly called 'smart' materials, can alter their physical properties in a predictable manner in response to an external stimulus like temperature[9], light[10], pH[11], magnetic field[12], electric field[13] etc. Some of the responses of smart materials to external stimuli include self-sensing, self-healing, self-actuating, self-diagnostic and shape changing[14]. Several stimuli responsive polymer gels have been developed so far[15]. Hybrid hydrogels formed of polyethylene glycol diacrylate, gelatin methacrylate-co-polyethylene glycol dimethacrylate and N-isopropylacrylamide, change their shape in response to the presence of an enzyme, collagenase, mimicking the motion of the insectivorous plant, Venus fly trap, in response to an insect sitting on its leaves[16]. Doubly pH responsive Pickering emulsions was created by using mixtures of oppositely charged nanoparticles and polyelectrolytes. The average diameter of the emulsion droplets could be easily tuned by varying pH[17]. Self-assembled azobenzene monolayer on a hydrophobic inverse opal surface, rendered the surface 'smart' with photo-controlled reversible wetting properties. This change in wettability was due to the reversible transition of azobenzene between cis and trans states on light irradiation[18]. Nanoemulsions composed of poly(dimethylsiloxane) oil droplets coated

with sodium dodecylsulphate dispersed in poly(ethylene glycol)diacrylate, underwent gelation owing to the formation of stress bearing percolating microstructure with arrested phase separation when the temperature was increased beyond a critical value. The gelation was brought about by interdroplet bridging by the continuous polymer phase[19].

Magnetic colloids also come under the category of smart materials where magnetic field assisted tuning of physical properties such as rheological[20], thermal[21] and optical properties[22] are possible. Owing to the field tunable physical properties, ferrofluids have found applications in many areas. Some of the applications are leak free seals[23, 24], clutches[25], dampers[26], optical filters[27] and grating[28], targeted drug delivery[29, 30], hyperthermia agents[31], coolants[32], defect sensors[33], lubricants[34] etc.

1.2 Ferrofluids

Ferrofluids are magnetic colloids with dispersed phase composed of 5-20 nm magnetic nanoparticles suspended in a suitable base fluid[35]. Ferrofluids undergo a very fast and reversible transition from a liquid to a near solid-like state when exposed to external magnetic field. Their micron-sized counterparts, magnetorheological fluids, are also widely popular and has been incorporated in several technological applications such as dampers, clutches, brakes etc., even though long term stability of the colloids owing to the large dimension of the dispersed phase poses a challenge[36]. Ferrofluid was invented by Steve S. Papell while working for NASA and the method of preparation was patented in 1965[37]. The small size of magnetic nanoparticles ensures stability against gravitational settling via Brownian motion. However, the large surface to volume ratio of the nanoparticles results in their aggregation via van der Waals and dipole-dipole attraction. In order to ensure long term stability, the nanoparticle surface is

modified to induce electrostatic or steric repulsion[38]. Electrostatic stabilization is commonly adopted while preparing aqueous ferrofluids where stabilization is brought about through introduction of surface charges[39]. Steric repulsion is brought about by an increase in osmotic pressure when the coated surfactants on two approaching particles interpenetrate[40]. Schematic depicting electrostatic and steric repulsion is shown in **Fig. 1.2**. Stability depended on the molecular weight of surfactant; experiments on stability of ferrofluids coated with copolymers of acrylic acid, styrenesulphonic acid and vinylsulphonic acid revealed that very low molecular weight surfactants were incapable of preventing aggregation and too high molecular weight surfactants lead to bridging between particles[41]. Bilayer surfactant stabilization was also proposed as a means to tailor the surface properties of the magnetic particles and to widen the choice of base fluid (polar/non-polar) without compromising on stability[42, 43].

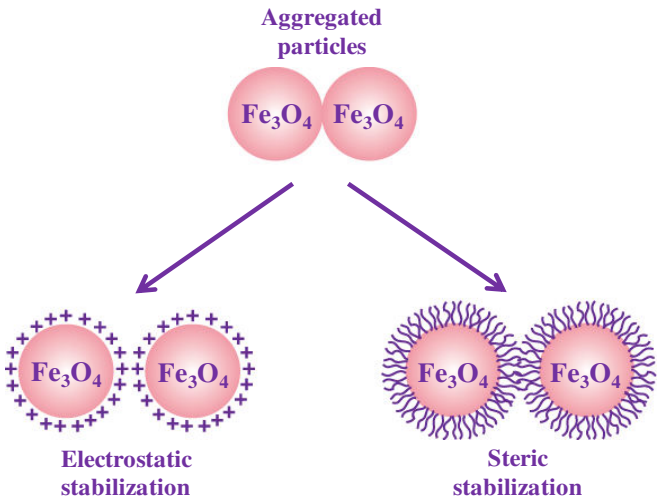

Figure 1.2: Schematic showing electrostatic and steric stabilization of magnetite nanoparticles.

Recently, ionic liquids as base fluid has attracted a lot of attention in the scientific community because of the possibilities of obtaining stable ferrofluids where the magnetic nanoparticles are not required to be surface modified[44]. In general, ferromagnetic or

ferrimagnetic metals or metal oxides are used as dispersed phase and some of the commonly used materials include iron, cobalt, nickel, iron oxide, iron nitride and substituted ferrites like manganese ferrite, nickel ferrite, cobalt ferrite etc[44]. The choice of dispersed phase is made with regard to the compatibility of the nanoparticles with the surfactant and the dispersion medium. Commonly used dispersion medium includes polar solvents like water, ethylene glycol and non-polar solvents like kerosene, silicone oil, mineral oil etc. The choice of dispersant rests on the requirement or application and involves consideration of parameters like boiling temperature, freezing point, viscosity, corrosiveness etc. Ferrofluids are prepared through one-step or two-step processes[44]. In the one-step method, synthesis and dispersion of the magnetic nanoparticles in the desired dispersion medium is done simultaneously. As the name suggests the two-step method involves two stages. The first stage involves synthesis of the magnetic particles via methods like co-precipitation[45], microwave assisted synthesis[46], solvo-thermal method[47], sol-gel synthesis[48], hydrothermal synthesis[49] etc. The second step involves coating the nanoparticle surface with suitable surfactant in order to obtain a stable colloid. Ferrofluids of exceptional stability have been synthesized in oil-based medium and water based systems offer difficulties as certain degree of aggregation was always present owing to stronger interparticle interaction in aqueous media which brings down long term stability due to the formation of aggregates, as revealed by small angle neutron scattering and static and dynamic light scattering measurements[50]. The nature of the surfactant used also affects ferrofluid stability, for example, in organic solvents carboxylate surfactants provided better dispersibility than phosphonate surfactants owing to the higher hydrophobicity of the former[51]. Another study assessing the stability of ferrofluids with regard to the nature of surfactant revealed that

surfactants that are fully wetted by the base fluid were better in imparting long term stability to the magnetic colloid[52].

1.3 Superparamagnetism

The small size of the magnetic nanoparticles in a ferrofluid makes them superparamagnetic in nature. Superparamagnetism is a form of magnetism exhibited by single domain ferromagnetic or ferrimagnetic materials[53, 54]. Being single domain, these particles have a net magnetic moment which can flip direction between preferred orientations by virtue of thermal energy. When the measurement time is much smaller than the relaxation time of the moment, then the particle exists in a well defined state, referred to as the blocked state, with the moment frozen in a particular direction. If the measurement time is much larger than the relaxation time, then the magnetization appears to be zero in the absence of an external magnetic field and particles are said to be in a superparamagnetic state. Superparamagnetic particles do not show hysteresis in the magnetization curve and they do not show remnant magnetization. In the presence of an external magnetic field, the magnetic moments of superparamagnetic particles align along the field direction just like a paramagnetic material but with much larger magnetic susceptibility. As the flipping of magnetic moment depends on thermal energy, one can talk of a certain value of temperature below which the particles exist in a blocked state and above which the particle is said to be superparamagnetic. This temperature which divides the blocked and superparamagnetic states is called the blocking temperature, T_B[54]. Schematic showing particles existing in blocked state below T_B and superparamagnetic state above T_B is shown in **Fig. 1.3**.

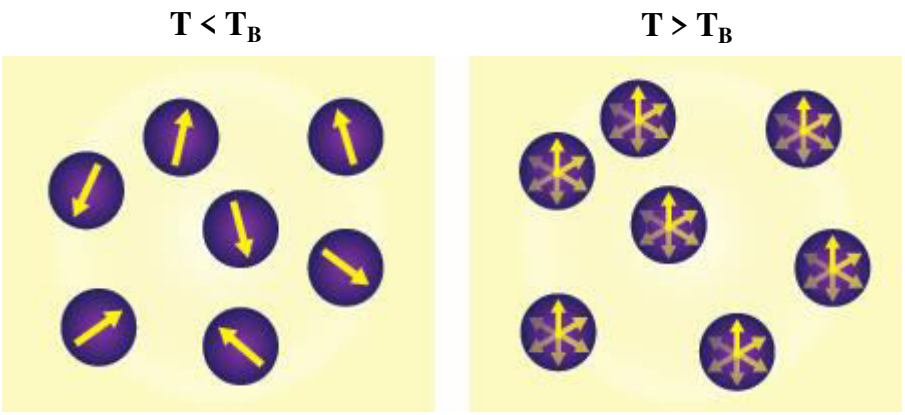

Figure 1.3: Schematic showing magnetic nanoparticles existing in a well defined state with magnetic moment fixed in a single direction below T_B and particles existing in a superparamagnetic state above T_B.

The magnetic nanoparticles in a ferrofluid, owing to their superparamagnetic nature, when exposed to a magnetic field, undergo aggregation that result in a rapid phase transition from a liquid to a solid-like material with altered physical properties.

1.4 Field induced aggregation in magnetic fluids

1.4.1 Tip-to-tip aggregation

In the absence of magnetic field, the magnetic moments of the superparamagnetic particles are randomly oriented by virtue of Brownian motion and hence the net magnetization of the ferrofluid system is zero[35]. The magnetic moment, below saturation magnetization where the moment increases linearly with increasing applied field, is given by[55]

$$m(H) = \frac{\pi}{6} d^3 \chi H \qquad (1.1)$$

where d is the diameter of the particle, χ is the magnetic susceptibility and H is the magnitude of the applied magnetic field. In the presence of an external magnetic field the magnetic moments

of the particles experience a torque which tends to align the moments along the magnetic field direction. There are two ways by which the moments align corresponding to two different time scales or two different relaxation times. They are Brownian relaxation and Neel relaxation. Brownian relaxation occurs when the magnetic moment appears to be fixed inside the particle and the alignment of magnetic moment along the field direction occurs via the rotation of the particle as a whole. Brownian relaxation time is given by[56]

$$\tau_{Brownian} = \frac{3\eta_c V_H}{k_B T} \tag{1.2}$$

where η_c is the viscosity of the carrier or base fluid, V_H is the hydrodynamic volume (volume of the particle along with the surfactant layer), k_B is the Boltzmann constant and T is the temperature. Neel relaxation is where the magnetic moment rotates within the particle without actual rotation of the particle as a whole. Neel relaxation time is given by[57]

$$\tau_{Neel} = \tau_0 e^{\frac{KV_p}{k_B T}} \tag{1.3}$$

where τ_0 is the attempt time (~1 x 10^{-9} s) which is related to the effective uniaxial anisotropy energy density K and V_p is the volume of the particle without the surfactant layer. Brownian and Neel relaxation are schematically shown in **Fig. 1.4**.

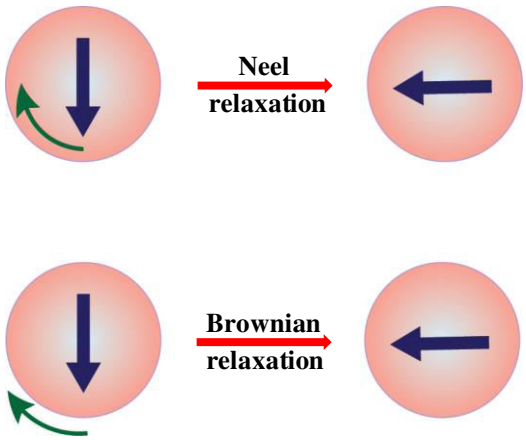

Figure 1.4: Schematic showing Neel and Brownian relaxation of magnetic particle.

By comparing eqns. (1.2) and (1.3), it is evident that for larger particles Brownian relaxation will be dominant as τ_{Neel} increases exponentially with V_p while $\tau_{Brownian}$ increases only linearly with V_H. In reality, any given ferrofluid system will be composed of particles with a size distribution. Hence, the effective relaxation will be a combination of both Brownian and Neel relaxation and it is given by[58, 59]

$$\frac{1}{\tau_{eff}} = \frac{1}{\tau_{Neel}} + \frac{1}{\tau_{Brownian}} \tag{1.4}$$

When the magnetic moment of the particles align along the magnetic field direction, the neighboring particles interact with each other and the interaction energy is given by[60]

$$U_{ij} = \frac{\mu_0}{4\pi}\left[\frac{(m_i.m_j)}{r_{ij}^3} - \frac{3(m_i.r_{ij})(m_j.r_{ij})}{r_{ij}^5}\right] \tag{1.5}$$

where μ_0 is the absolute magnetic permeability and m_i and m_j are the magnetic moments of particles i and j separated by distance r_{ij} (see **Fig. 1.5**).

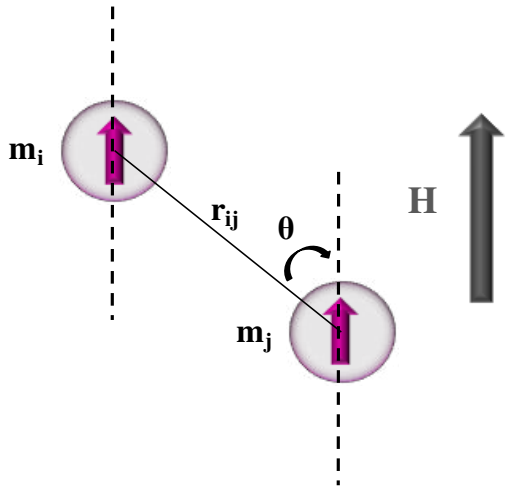

Figure 1.5: Schematic showing interaction between two superparamagnetic particles in the presence of a magnetic field.

From eqn. (1.5), assuming that particles i and j have the same magnetic moment m, the interaction energy can be rewritten as

$$U_{ij} = \frac{-\mu_0 m^2}{2\pi r_{ij}^3}\left[1 - \frac{3}{2}sin^2\theta\right] \tag{1.6}$$

where θ is the angle between the direction of the applied field and the line joining the centers of the two magnetic particles. The interaction energy is minimum when $\theta = 0$ and $r_{ij} = d$ and the minimum interaction energy is given by

$$U_{ij} = \frac{-\mu_0 m^2}{2\pi d^3}\,. \tag{1.7}$$

In the presence of magnetic field, the particles undergo tip-to-tip aggregation in a chain-like formation. Chain formation depends on the balance between the reduction in energy with aggregation and the reduction in entropy. Hence, thermodynamic variables like concentration

and temperature comes into picture. The field induced aggregation can be quantified by a dimensionless quantity called the aggregation parameter, N^* which is given by[61, 62]

$$N^* = \sqrt{\Phi e^{\lambda-1}} \tag{1.8}$$

where Φ ($\Phi = {\mathrm{mf} * \rho_{\mathrm{bf}}}\Big/{\left[(\mathrm{mf} * \rho_{\mathrm{bf}}) + (1 - \mathrm{mf})\rho_{\mathrm{p}}\right]}$, mf – mass fraction, ρ_{bf} - density of base fluid, ρ_{p} - density of particle) is the volume fraction of the ferrofluid and λ is the magnetic coupling parameter which is defined as the ratio of magnetic energy to thermal energy and it is given by[63]

$$\lambda = \frac{\mu_0 m^2}{2\pi d^3 k_B T}. \tag{1.9}$$

Chain formation occurs when $N^* > 1$. If thermal energy is dominant over magnetic energy then $\lambda < 1$ and $N^* < 1$ and field induced aggregation is not possible. Even if magnetic energy is dominant over thermal energy ($\lambda > 1$) aggregation occurs only if the volume fraction of magnetic nanoparticles is high enough to ensure $N^* > 1$. For $N^* < 10$ the equilibrium state of the ferrofluid is composed of single chains of varying sizes. Field induced aggregation is rapid and the average chain length ($\langle l_{chain} \rangle$) increases with time as $\langle l_{chain} \rangle \, \alpha \, t^{\nu}$ where t is the time and $0.45 < \nu < 0.8$ [64].

1.4.2 Lateral aggregation or zippering

When tip-to-tip aggregation is no longer energetically favorable, lateral coalescence called zippering takes over leading to the formation of thick columnar aggregates which can be observed by an optical microscope. The cross-over time, $t_{critical}$ between tip-to-tip aggregation and lateral coalescence was found to be[63]

$$t_{critical} = \frac{\sqrt{\lambda}}{\phi} \tag{1.10}$$

Magnetic field induced aggregation has been experimentally observed using small angle X-ray scattering[65], small angle neutron scattering[66], optical microscopy[63] and cryo-TEM[67]. Several models were developed over the years to explain the attraction between dipolar chains leading to zippering. The first model was proposed by Halsey and Toor[68]. They proposed that the coupling between strong Landau-Peierls thermal fluctuations of chains were responsible for the observed long range interaction between them. Rigid chains are expected to interact with each other at a short range only. Lateral interaction is repulsive if the relative position of the particles in one chain is in-registry to the position of the particles in the neighboring chain and attractive if the position is off-registry. The lateral interaction is given by[69]

$$U(\rho) = \pm(2\pi)^2 \frac{2m^2}{4\pi\mu_0\rho^2 d}\left(\frac{d}{\rho}\right)^{1/2} e^{-2\pi\rho/d} \tag{1.11}$$

where ρ is the lateral distance between the chains. If $\rho > 2d$ then the interaction is repulsive as the chain ends dominate the interaction and if $\rho < 2d$ then the interaction is strong and either repulsive or attractive depending on whether the relative position of particles in the neighboring chains are in or off registry. Halsey and Toor[68] reported that the lateral interaction energy is the sum of interaction energy resulting from thermal fluctuations and the deformation energy necessary for the fluctuation mode. Later Martin and co-workers[70, 71] put forth the modified Halsey-Toor model which takes into account the observed power law dependence of lateral coalescence with the strength of the applied field that could not be explained by Halsey-Toor model. When the time scale for coalescence is less than the time scale for relaxation of thermal fluctuations, coarsening or zippering occurs. Field induced aggregation in ferrofluids is

schematically shown in **Fig. 1.6**. Coarsening can also be initiated by defects in the chains as defects lead to local variations in the dipole moment density, breaking the symmetry of the lateral field[72]. Furst et al.[69] studied lateral interaction among chains through direct force measurements using optical trapping. They observed that for low field strengths where the chains were not rigid, thermal fluctuations were dominant and coupling between thermal fluctuations of neighboring chains resulted in long range lateral interaction. Attaining a steady state becomes longer when lateral interactions are long ranged[73]. For high magnetic field strengths, the chains were rigid and interaction became short ranged with a repulsive barrier. The length of the chains also played an important role in determining whether the interaction is attractive or repulsive. For shorter chains repulsion from the chain ends was more prominent than for longer chains. For low cluster concentrations, lateral coalescence can be expressed crudely by the Smoluchowski kinetic equation given by[74]

$$\frac{dN_k}{dt} = \frac{1}{2}\sum_{i+j=k} K_{ij} N_i N_j - N_k \sum_{j=1}^{\infty} K_{kj} N_j \qquad (1.12)$$

where $\frac{dN_k}{dt}$ is the rate of change in the number of aggregates containing k particles, K_{ij} is the reaction kernel which gives the rate of coalescence of an aggregate containing i particles with an aggregate containing j particles and N_i is the number of aggregates containing i particles. The first term of the above equation represents the formation of an aggregate containing k particles through coalescence of two smaller aggregates containing i and j particles. The second term indicates the loss of aggregates containing k particles through further coalescence.

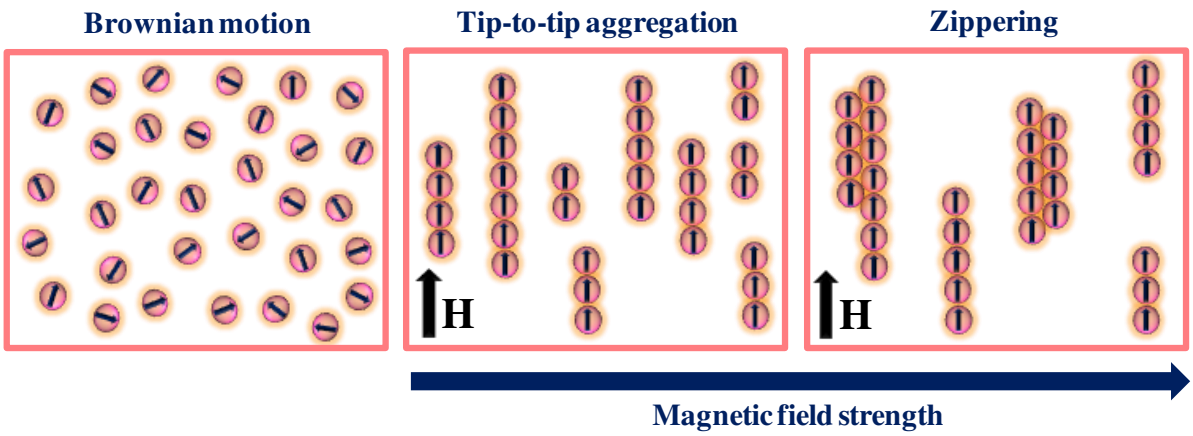

Figure 1.6: Schematic showing field induced aggregation in a ferrofluid. In the absence of magnetic field the particles are in Brownian motion. In the presence of field they undergo tip-to-tip aggregation followed by zippering transitions at higher field strengths.

Zubarev and Ivanov[75, 76] identified three different stages of field induced aggregation: Formation of critical nuclei that initiate chain formation, growth of the nuclei into chain like aggregates and lateral coalescence of chains leading to thicker aggregates. Aggregation is initiated by primary aggregates composed of larger particles with smaller particles clustered around them. As the number of particles is conserved, the growth rate of the critical nuclei can be expressed as[64]

$$J = \frac{dN}{dt} = \frac{(n_i - n_s)dV}{dt} \tag{1.13}$$

where J is the particle flux towards the aggregate, N is the number of particles in the aggregate, V is the volume of the aggregate, n_i is the number of particles within the aggregate and n_s is the number of particles near the vicinity of the aggregate. The particle flux depends on the gradient of chemical potential in the immediate vicinity and the magnetophoretic flux which results in particle migration towards the aggregate. After the initial length-wise growth of aggregates,

lateral coalescence sets in. Coalescence begins only when the aggregate has reached a critical volume which is given by[75]

$$V_c^{1/3} = \frac{2V_p\Phi_{dilute}\sigma\kappa}{3k_BT\Phi_{dense}\Delta} \tag{1.14}$$

where Φ_{dilute} is the volume fraction of particles in the dilute phase in the vicinity of an aggregate, Φ_{dense} is the volume fraction of particles within an aggregate, $\Delta = \Phi_\infty - \Phi_{dilute}$ is the supersaturation where Φ_∞ is the volume fraction of particles far away from the aggregate, σ is the interfacial tension and $\kappa = \frac{S}{V_c^{2/3}}$ where S is the surface area of the aggregate. From equation (1.14) one can see that the critical volume is a function of the particle size which implies that aggregation depends heavily on the particle size distribution. For a relatively monodisperse system with average size around 10 nm, nucleation will take longer time for a given field strength than for a polydisperse system, containing large aggregates, of same average size since in the former critical nuclei has to form and then overcome the potential barrier to initiate the growth phase while in the latter some of the bigger particles themselves can act as nucleation centers and initiate growth. With time, as the distance between aggregates increases, the coalescence rate falls off and steady state is reached[77].

1.4.3 Factors affecting field induced aggregation

Field induced aggregation depends on several variables like strength of magnetic field, volume fraction of magnetic nanoparticles, size and polydispersity of the dispersed phase, temperature, confining cell geometry etc.

1.4.3.1 Size and polydispersity

In a ferrofluid system, for a given strength of magnetic field, larger particles have higher tendency to aggregate owing to their larger dipole moment (eqn. (1.9)) which gives rise to larger magnetic particle-particle interaction. Ferrofluids composed of extremely small particles do not aggregate even in the presence of magnetic field. Larger particles on the other hand result in the formation of thick columnar aggregates even for low field strengths[55]. Hence, the size of the particles is one of the important factors that determine the microstructure of a ferrofluid system in the presence as well as absence of magnetic field. In concentrated ferrofluids, exposure to magnetic field of high strength can lead to formation of tightly packed aggregates whose correlation with the neighbors increases with increasing field strength[78]. High particle-particle interactions leads to the formation of aggregates that are thinner owing to the presence of large potential barriers that prevent further coarsening[79]. Even after the magnetic field is removed for relatively larger particles, certain aggregates persist as the dipole moments of the larger particles remain partially aligned even in the absence of magnetic field since above a certain particle volume, the energy required for the moment to change direction becomes higher and thermal energy will be insufficient to allow rotation[65].

In reality, polydispersity is inevitable in ferrofluid systems. Pshenichnikov et al.[80] reported that a gamma distribution is the best to describe the particle size distribution of ferrofluids. The gamma distribution was found to give better accuracy while calculating higher moments owing to its faster decaying tail which mimics real colloidal systems and the distribution is given by

$$f(x) = \frac{x^y e^{-x/x_0}}{x_0^{y+1}\Gamma(y+1)} \tag{1.15}$$

where y and x_0 are two parameters and $\Gamma(y+1)$ is a gamma function. For field strengths that are much below the saturation magnetization regime, the magnetic properties depend heavily on the size of the particles, for example the larger particles in the distribution can give rise to higher values of initial magnetic susceptibility than a monodisperse system. For a polydisperse system, the coupling constant is modified as[81]

$$\Lambda = \frac{\mu_0}{4\pi k_B T \sum_i M_i m_i^2} \sqrt{\sum_{i,j} \frac{M_i M_j m_i^4 m_j^4}{d_{ij}^6}} \tag{1.16}$$

where M_i is the number of particles having magnetic moment m_i and $d_{ij} = \frac{d_i + d_j}{2}$ where d_i is the diameter of ith particle. For a polydisperse system the susceptibility is modified as

$$\chi_{polydisperse} = \chi_L \left[1 + \frac{\chi_L}{3}\left(1 + \frac{\Lambda^2}{25}\right) + \frac{\chi_L^2}{144}\right] \tag{1.17}$$

where χ_L is the Langevin susceptibility. The magnetic moments of larger particles will align along the direction of applied field more readily than smaller particles, giving rise to larger values of initial susceptibility. Hence for polydisperse ferrofluids with significant fraction of larger particles field induced aggregation will be possible for field strengths much lower than what is necessary to induce aggregation in a relatively monodisperse system with the same average size of particles and thick columnar aggregates form in the polydisperse samples after extensive zippering transitions. Simulations revealed that in polydisperse ferrofluids, the larger particles tend to aggregate first and the smaller particles show a tendency to reside in the interstitial spaces leading to a more compact aggregate when compared to an aggregate of a monodisperse system[82, 83]. Computational studies also revealed that in polydisperse ferrofluids the most probable chain structure will be composed of 1-3 large particles in the

middle with the smaller particles at the edges. Fraction of smaller particles in the system greatly affects the microstructure. In polydisperse systems with significant fraction of smaller particles, it was observed that most of the particles remained unaggregated and the rest lead to shortening of chains (formed by larger particles) by attaching to the chain ends thereby poisoning them and preventing further length-wise growth[84, 85].

Even in the absence of external magnetic field, ferrofluids composed of significant fraction of larger particles show presence of aggregates[86]. In the case of monodisperse systems of large size, in the absence of magnetic field the particles form open necklace like structures whose length increases with increase in particle-particle interaction. In the case of polydisperse ferrofluid with small standard deviation, the particles self assemble into larger necklace like structures and few loop like clusters. When the standard deviation of the particle size distribution is high, the particles aggregate into clumps for weak particle-particle interaction and form network like structure for larger particle-particle interaction.

1.4.3.2 Volume fraction

Neutron scattering studies revealed that for very low volume fraction, field induced aggregates were absent[65]. For extremely low volume fractions (less than 1 vol.%) only monomers and dimmers exist[87, 88]. For slightly higher volume fractions, only single chain-like aggregates were present. Only above a certain volume fraction, which again depends on the size of the particles and the strength of the applied field, do lateral coalescence or zippering take place[63]. The magnetization curve and initial susceptibility also depends heavily on volume fraction[89]. Increasing particle concentration leads to the formation of thicker aggregates[84, 90]. Improperly stabilized ferrofluids without uniform surfactant coating was reported to

aggregate much faster than properly stabilized systems owing to the increased magnetic attraction of the former[91]. Ferrofluids of very high volume fractions, when exposed to external magnetic field of high strength, are known to have a microstructure where the aggregates are packed in a hexagonal arrangement with pseudo-crystalline ordering and the average distance between the aggregates decreases with increasing volume fraction. For magnetic colloids of very high surface fractions, cross linking of individual chains have also been observed. For high volume fractions, even in zero field aggregates have been observed[92].

1.4.3.3 Strength of external magnetic field

The spatial distribution of particles in a ferrofluid is, in general, isotropic in the absence of magnetic field (except for ferrofluids containing large particles). In the presence of an external magnetic field, the coupling constant, λ (eqn. (1.9)) increases which is an indication of the increased interaction of the particles with their neighbors. For very low field strengths only monomers and dimers exist[79]. With increasing magnetic field strength, initially the length of the aggregates increases[65] and with further increase in field strength, when it becomes energetically unfavorable for tip-to-tip aggregation to occur, the aggregates zipper, provided the volume fraction is high enough[63, 69].

1.4.3.4 Dimensions of confining cell

Ferrofluids confined in thin films are known to form different patterns depending on volume fraction, strength and ramp rate of applied magnetic field and the dimensions of the confining cell. Yang et al.[93] observed that in highly confined ferrofluids, for higher field strengths and for larger field ramp rates, the average width of the aggregates deceased while the number density of aggregates increased. Higher ramps resulted in the formation of aggregates

which are more closely packed than slower ramps[94]. Also larger the dimension of the confining cell, larger was the separation between the aggregates. Decrease in volume fraction of magnetic particles also lead to the formation of widely spaced aggregates. When confined to very thin films and exposed to perpendicular magnetic fields, ferrofluids of high volume fraction even form complex microstructure like labyrinthine (very thin films exposed to high magnetic field strengths) and hexagonal patterns (thicker fluid films)[95, 96]. When magnetic field is applied parallel to the magnetic thin film, columnar aggregates formed whose separation and width varied inversely with strength and ramp rate of applied field[97].

1.5 Rheological properties of ferrofluids in the presence of magnetic field

McTague[12] first reported the variation of viscosity of ferrofluid with the strength of the applied magnetic field. Using a capillary viscometer he demonstrated that the viscosity of a ferrofluid increased with application of magnetic field, the increase being more dramatic when the direction of magnetic field is parallel to the flow direction. For higher field strengths viscosity saturated and for low volume fractions of magnetic particles the increase in viscosity was independent of volume fraction and size of the nanoparticles. The increase in viscosity was termed as 'rotational viscosity' as it was believed that the hindrance to rotation of particles in the base fluid was responsible for enhanced viscosity. Rosensweig et al.[98] demonstrated experimentally and theoretically that the rise in viscosity is proportional to the ratio of hydrodynamic stress to magnetic stress. Viscosity of dilute ferrofluids, in the absence of magnetic field, is described by Einstein's formula,

$$\eta = \eta_c\left(1 + {}^{5}/_{2}\,\Phi\right) \tag{1.18}$$

where η is the viscosity of the ferrofluid, η_c is the viscosity of the base fluid and Φ is the volume fraction. In the presence of external field the rotational viscosity is given by[99]

$$\Delta\eta = \frac{3}{2}\Phi\eta_c \frac{\xi' - tanh\xi'}{\xi' + tanh\xi'} sin^2\alpha \qquad (1.19)$$

where $\xi' = \frac{\mu_0 mH}{k_B T}$ and α is the angle between the direction of applied magnetic field and the angular velocity of rotation, Ω of the ferrofluid (see **Fig. 1.7**). From the above equation, when the direction of the magnetic field is parallel to the direction of angular velocity, the viscosity is independent of the applied field. Maximum increase in viscosity can be obtained when the direction of applied field is perpendicular to the angular velocity. Later, equation (1.19) was modified to take into account various other parameters.

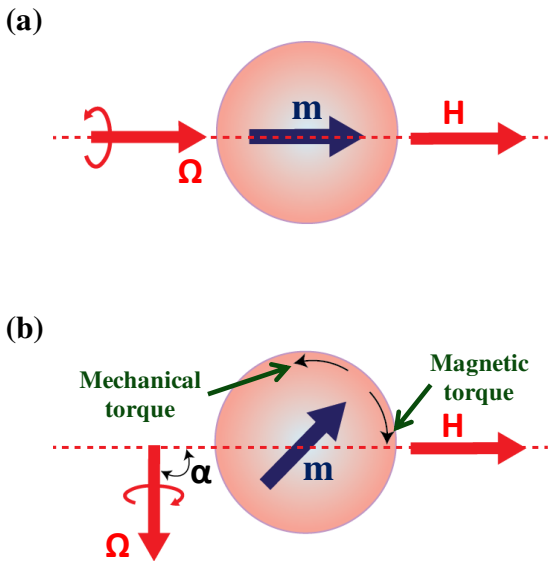

Figure 1.7: Schematic showing the direction of magnetic moment of a particle when the applied field is (a) parallel to angular velocity and (b) perpendicular to angular velocity.

However, the theory of rotational viscosity was unable to account for the drastic increase in viscosity observed when concentrated ferrofluids were subjected to magnetic fields[100]. This discrepancy between theory and experiment was attributed to particle-particle interaction which was not considered during the earlier theoretical formulation. Subsequently, the increase in viscosity when ferrofluids were exposed to magnetic field applied perpendicular to the flow field was termed as magnetoviscous effect (MVE) and the increase was attributed to magnetic field induced formation of chain-like or columnar aggregates that oppose flow. Hence, the rheological properties depends on the microstructure that form in the presence of magnetic field and differ from one ferrofluid system to another depending on factors like volume fraction, size and polydispersity of particles, type of base fluid, temperature, applied shear field parameters, strength of the applied magnetic field etc[20]. For low particle volume fraction, ferrofluids behave as Newtonian liquids and for higher volume fractions, shear thinning was observed.

1.5.1 Factors affecting rheological properties of ferrofluids

1.5.1.1 Shear rate

For a constant non-zero magnetic field, Odenbach et al.[101] observed a decrease in viscosity with increasing shear rate. This decrease was attributed to the destruction of the field induced aggregates. The magnetic force between two dipoles aligned along the field direction is given by[102]

$$F_M = \frac{\mu_0 M_0^2 \pi d^6}{24 d_{hydrodynamic}^4} \tag{1.20}$$

where M_0 is the spontaneous magnetization. The hydrodynamic force experienced by the field induced aggregates in a shear field which is perpendicular to the direction of applied magnetic field is given by[101]

$$F_H = \frac{6\pi\eta_c\dot{\gamma}}{2}\left[\frac{Nd_{hydrodynamic}}{2}\right]^2 \tag{1.21}$$

where $\dot{\gamma}$ is the shear rate. When ferrofluids exposed to high magnetic field strengths are subjected to low shear rates the field induced aggregates remain aligned along the direction of magnetic field. With increasing shear rate the aggregates deviate more from the direction of magnetic field, the deviation becoming more prominent with increasing shear rate. Beyond certain shear rate, the aggregates begin to disintegrate and eventually at high shear rates the aggregates are completely destroyed[103]. The number of particles in a chain decrease with increasing shear rate and the maximum number of particles in a chain under a given shear rate is given by[104, 105]

$$N_{max} = \sqrt{\lambda\frac{D}{\dot{\gamma}}} \tag{1.22}$$

where D is the diffusion coefficient. With increasing shear, the destruction of field induced aggregates gives rise to shear thinning and the degree of shear thinning increases with increase in magnetic field strength. Effect of shear on field induced microstructure of ferrofluid is schematically shown in **Fig. 1.8**.

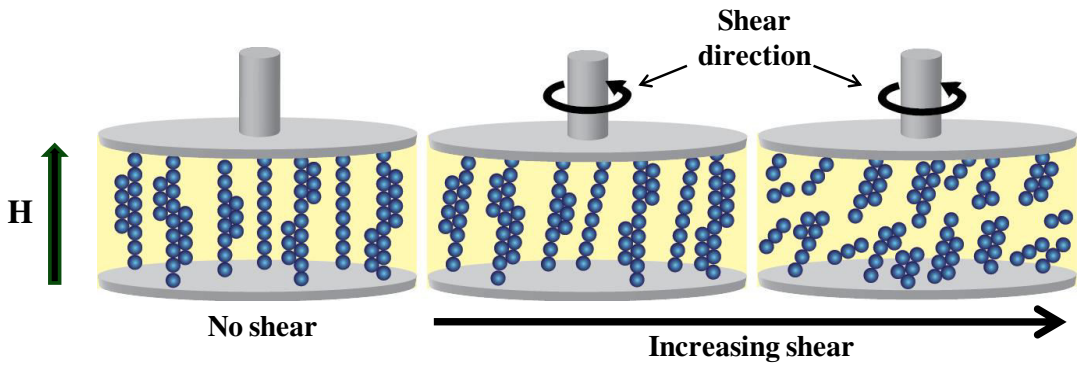

Figure 1.8: Schematic showing field induced microstructure of ferrofluid under shear.

The performance of magnetic fluids like ferrofluids and magnetorheological fluids are generally assessed with respect to a dimensionless quantity called the Mason number which is the ratio of hydrodynamic force to magnetic force and it is given by[106, 107]

$$Mn = \frac{72\eta_c\dot{\gamma}}{\mu_0\mu_c\langle M_p\rangle^2} \tag{1.23}$$

where μ_c is the relative magnetic permeability of the base fluid and $\langle M_p\rangle$ is the mean magnetization of the dispersed phase. The main advantage of scaling the viscosity curves with this dimensionless number is that the effect of applied shear and magnetic field can be quantified in terms of a single parameter, Mn, thus avoiding the need for tedious data acquisition[107]. Generally the field specific viscosity, given by $\eta_F = \frac{\eta-\eta_\infty}{\Phi\eta_c}$ where η_∞ is the infinite shear viscosity in the absence of magnetic field, is plotted against the Mason number. It was observed that if only hydrodynamic and magnetic forces are the dominant forces affecting the flow behavior of magnetic colloids, then the viscosity curves obtained for different magnetic field strengths will collapse onto a master curve[108]. For low magnetic field strengths it was observed that the collapse was poor as thermal energy is comparable to hydrodynamic and magnetic energy.

1.5.1.2 Magnetic field strength

With increasing magnetic field strength, the aggregates become more rigid, elongated and coarser. Significant increase in viscosity is obtained when the field induced aggregates span the gap between the rheometer plates[109]. Gap spanning aggregates form, provided the volume fraction of magnetic nanoparticles and the strength of applied magnetic field are high enough. Hence, with increasing magnetic field strength, the magnetoviscous effect becomes more prominent. The increase in elastic properties of ferrofluid with increasing magnetic field strength has been thoroughly investigated by researchers using oscillatory rheology and it was observed that with increasing magnetic field, ferrofluids became more viscoelastic, in stark contrast to the fluid like nature displayed by them in the absence of magnetic field[110-112].

In the presence of magnetic field, ferrofluids undergo a transition from a liquid to a viscoelastic material with a yield stress[113]. In ferrofluids measurable yield stress is obtained for moderate to high volume fractions. Static and dynamic yielding has been observed in ferrofluids[20]. Static yielding is brought about by the slipping of the field induced aggregates on the moving plate of the rheometer beyond a particular shear rate or shear stress without actual breakage of the aggregates[109]. It is either obtained from the low shear extrapolation of flow curve expressed in double logarithmic scales or through the tangent method where the ferrofluid is subjected to shear stress ramp and the value of stress for which the strain response becomes nonlinear is taken as the static yield stress[6]. Dynamic yield stress is the stress required to continuously break the field induced aggregates that try to reform under the influence of the applied magnetic field. In general dynamic yield stress is obtained by fitting the flow curves to different models[36, 114, 115]. Bingham model is the simplest model available. It describes the

behavior of concentrated colloids subjected to flow, which after yielding display Newtonian behavior and it is given by[6]

$$\tau = \tau_y + \eta_{Bingham}\dot{\gamma} \tag{1.24}$$

where τ is the shear stress, τ_y is the yield stress and $\eta_{Bingham}$ is the Bingham viscosity (slope of the Newtonian region of flow curve after yielding). However, for concentrated ferrofluids Bingham model is not a good fit owing to its simplicity and the flow behavior of concentrated ferrofluids are much more complex. Another model which better describes flow behavior of ferrofluids in the presence of magnetic field is the Casson model which is given by[6]

$$\sqrt{\tau} = \sqrt{\tau_y} + \sqrt{\eta_{Casson}\dot{\gamma}} \tag{1.25}$$

where η_{Casson} is the Casson viscosity which is the viscosity obtained at high shear rate. The Casson model is similar to the Bingham model but with a more gradual transition between the regions before and after yielding. Herschel-Bulkley model is another model that characterizes the flow behavior of ferrofluids rather well as it describes the non-Newtonian behavior of the ferrofluid after yielding and it is given by[6, 39]

$$\tau = \tau_y + K'\dot{\gamma}^n \tag{1.26}$$

where K' is the consistency index and n is the degree of shear thinning. For shear thinning materials, $n < 1$ and for shear thickening materials, $n > 1$. When $n = 1$, the Herschel-Bulkley model reduces to the Bingham model. The dynamic yield stress is typically larger than the static yield stress[116]. Yield stress (both static and dynamic) varies from fluid to fluid depending on the microstructure under the influence of magnetic field and so yield stress was found to increase with increasing volume fraction and magnetic field strength and with the inclusion of larger

particles since in all three cases the field induced structure become increasingly coarser and rigid[117-119].

Ginder and co-workers[120] reported that for magnetic field strengths falling in the linear region of magnetization, the yield stress varies with the strength of the applied field as

$$\tau_y \, \alpha \, \mu_0 \mu_c \beta_{vis}^2 H^2 \tag{1.27}$$

where $\beta_{vis} = \frac{\mu_p - \mu_c}{\mu_p + 2\mu_c}$ is the contrast factor. However, for field strengths close to saturation magnetization M_s, the variation of yield stress with the applied field is given by

$$\tau_y = \sqrt{6}\mu_0 M_s^{1/2} H^{3/2} \tag{1.28}$$

and in the saturation regime, yield stress becomes independent of the strength of applied field and is given by

$$\tau_y = 0.086 \Phi \mu_0 M_s^2 \tag{1.29}$$

The morphology of the dispersed phase also affects yield stress where ferrofluids composed of disc shaped and rod shaped particles had higher yield stress than ferrofluid composed of spherical particles[116, 121]. For nanofibers, the interparticle friction between particles was reported to be the main reason for the enhanced magnetoviscous effect and yield stress. Certain additives like nanosilica[108], multi-walled carbon nanotubes[122], micron sized magnetic particles[123] etc. also enhance yield stress.

1.5.1.3 Volume fraction

With increase in particle content, magnetorheological properties of ferrofluids change[20, 124]. Increasing volume fraction results in larger magnetoviscous effect due to the formation of thicker rheometer gap spanning aggregates[125, 126]. When the particle concentration of a ferrofluid composed of polyethylene coated magnetite nanoparticles was increased from 1 to 15 wt.%, the rheological behavior changed from Newtonian at low concentrations to non-Newtonian with higher particle loading[127]. With increasing volume fraction, ferrofluids become increasingly viscoelastic in the presence of external magnetic field.

1.5.1.4 Incorporation of additives

To improve the rheological properties, various additives have been incorporated into ferrofluids over the years. Small volume fractions of tobacco mosaic virus when added to a cobalt ferrite based ferrofluid resulted in more than one order magnitude increase in viscosity[128]. This substantial enhancement in viscosity was due to the alignment of the virus along magnetic field direction which was brought about by the electrostatically attached magnetic nanoparticles on the virus surface. The viscosity enhancement increased with increasing field strength and length and concentration of the virus. Addition of hydrophilic silica nanoparticles into an oil based ferrofluid resulted in the formation of gap spanning silica network that lead to decreased shear thinning at high shear rates[129]. The silica network reduced the field induced viscosity and yield stress by hampering zippering transitions. Incorporation of multiwalled carbon nanotubes into an oil based ferrofluid led to decrease in viscosity, static yield stress and viscoelastic moduli owing to weakened dipolar interaction between magnetic particles due to the intervening non magnetic carbon nanotubes[122].

1.6 Thermal properties of ferrofluids in the presence of magnetic field

Technological advancement and miniaturization of electronic gadgets fueled intense research on nanofluids as potential candidates for cooling applications as a substitute to conventional heat transfer fluids like water, ethylene glycol etc[130]. Incorporation of relatively small quantity of nanoparticles into conventional heat transfer fluids increases thermal conductivity substantially. The small size of the nanoparticles ensures stability against gravitational settling with shelf life of several years. Additionally, nanofluids do not cause clogging of pipes through which they are pumped through and hence they are preferred over colloids containing micron sized particles[131]. For dilute suspensions devoid of interparticle interactions, thermal conductivity (k) of the nanofluid is described well by the Maxwell model given by[130]

$$\frac{k}{k_f} = \frac{1+2\beta\Phi}{1-\beta\Phi}, \quad \beta_{TC} = \frac{k_p - k_f}{k_p + 2k_f} \tag{1.30}$$

where k is the effective thermal conductivity of the suspension, k_f is the thermal conductivity of the base fluid and k_p is the thermal conductivity of the nanoparticle. For higher volume fractions where interparticle interaction is significant, Maxwell's model was unable to account for the effective thermal conductivity of the nanofluid[132]. Several mechanisms were put forth to explain anomalous thermal transport in nanofluids, though the exact mechanism/mechanisms responsible for thermal transport is still under debate. Some of the popular mechanisms are thermal transport via Brownian motion of nanoparticles, liquid layering of base fluid molecules around the nanoparticles and nanoparticle aggregation[132-134]. Several factors like size and morphology of the nanoparticles, volume fraction of solid phase, type of base fluid used, temperature, nature of additives etc. affect thermal conductivity of nanofluids. Some of the most

commonly used experimental techniques for thermal conductivity measurements of nanofluids are transient hot wire method, thermal constants analyzer and 3ω method[130].

Among nanofluids, ferrofluids have attracted a lot of attention owing to the magnetic field tunable thermal conductivity displayed by them[135, 136]. By tailoring the composition of ferrofluids substantial increase in thermal transport can be achieved through the application of an external magnetic field whose direction is parallel to the direction of heat flux[21, 137]. The field induced aggregates act as low resistance pathways thereby improving thermal transport substantially.

1.6.1 Enhancement of k in the absence of magnetic field

Even in the absence of magnetic field, thermal conductivity of ferrofluids has been studied extensively as function of many parameters though solid correlation of each parameter to thermal conductivity is still under debate owing to conflicting reports which is likely due to the highly sensitive dependence of k on material properties:

1.6.1.1 Volume fraction

In the absence of magnetic field, Philip et al.[136] observed an increase in thermal conductivity with increase in volume fraction above a critical concentration (1.71 vol.%). Sundar et al.[138] reported an increase in thermal conductivity of Fe_3O_4/water ferrofluid (average diameter of magnetite: 13 nm) with increasing volume fraction (0-2%). Pastoriza-Gallego et al.[139] observed a linear increase in k with concentration (even for the highest concentration particles were unaggregated) while non-linear increase was reported by Hong et al.[140] and the nonlinearity was attributed to enhanced heat transport owing to the formation of aggregates.

Depending on nanofluid preparation, the critical concentration above which significant clustering occurs differs from one ferrofluid to another[141, 142].

1.6.1.2 Temperature

Magnetite nanoparticles dispersed in water showed increase in thermal conductivity with increasing temperature (10 - 40 ^{0}C)[141]. Thermal conductivity of ferrofluid composed of magnetite nanoparticles in ethylene glycol was found to be independent of temperature for measurements carried out in the range 10 - 50 ^{0}C[139]. Yu et al.[143] investigated the effect of temperature on k of kerosene based ferrofluid and they observed that while the effective thermal conductivity of the entire system increased with increasing temperature (10 - 60 ^{0}C), the value of k relative to the k of base fluid was independent of temperature.

1.6.1.3 Nature of base fluid

The viscosity of the base fluid was reported to affect thermal conductivity of nanofluids. By tuning the viscosity of the base fluid, composed of diesel oil and polydimethylsiloxane, of a ferrofluid by changing the volume fraction of the two base fluid components, Tsai et al.[144] reported that thermal conductivity of the ferrofluid reduced to the value predicted by Maxwell with increase in viscosity. The authors reasoned that increasing viscosity decreased Brownian motion which led to the decrease in thermal transport. It was also reported that the increase in thermal conductivity with respect to the base fluid was higher for ferrofluids composed of base fluids having lower k, for example, hydrocarbon solvents. Though the effective k of the ferrofluid is higher for a high k solvent like water, the increase in k with respect to the base fluid is higher for ferrofluids composed of low k hydrocarbon solvents.

1.6.1.4 Effect of additives

Incorporation of additives into ferrofluid affects the effective k of the system. Addition of copper oxide (CuO) in a water based ferrofluid, with constant volume fraction of magnetite, was found to increase k of the system, the increase being more prominent for greater than 3% concentration of CuO and for higher volume fraction of magnetite[145]. Addition of silver nanowires in a water based ferrofluid lead to enhancement in thermal transport[146]. Increase in volume fraction of the nanowires increased k of the ferrofluid and the enhancement in k with incorporation of very small quantity of Ag nanowires (0.11 vol.%) was attributed to the large aspect ratio of the nanowires.

In an effort to improve thermal transport in ferrofluids, hybrid ferrofluids were also developed over the years. Sundar et al.[147] synthesized magnetic nanodiamond-cobalt oxide nanocomposite whose thermal properties were found to be better than cobalt oxide based ferrofluid. Heat transport under laminar flow of graphene magnetite hybrid nanofluid was investigated by Sadeghinezhad et al.[148]. The authors reported that the hybrid nanofluid was highly stable with the graphene sheets acting as a supporting material and in the presence of external magnetic field heat transfer was enhanced by 82%. Sun et al.[149] developed magnetic graphite nanoflake suspensions and they obtained 325% enhancement in thermal conductivity in the presence of magnetic field with just 0.8 wt.% of the solid phase. Wright et al.[150] developed hybrid ferrofluid with nickel nanoparticles attached onto single walled carbon nanotubes and the heat transport was improved in the presence of magnetic field owing to the alignment of the carbon nanotubes along field direction because of the attached nickel nanoparticles.

1.6.2 Enhancement of k in the presence of magnetic field

In the presence of magnetic field the thermal transport of ferrofluids can be altered owing to the formation of chain-like aggregates that serve as low resistance pathways for heat flow. In addition to material properties like volume fraction of nanoparticle, size of the particles, nature of base fluid and nature of functionalization, k becomes a function of the strength and orientation of the applied magnetic field[21, 137, 141].

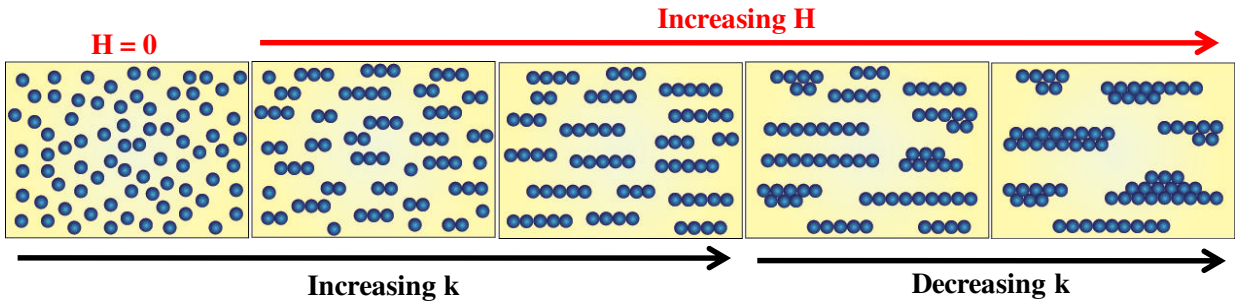

Figure 1.9: Schematic depicting the variation in k with applied magnetic field strength.

Ferrofluids exposed to an external magnetic field display enhanced thermal transport with k increasing as the strength of the magnetic field is increased. Shima et al.[151] studied field tunable k of kerosene based magnetite nanofluid as a function of volume fraction and strength and orientation of applied magnetic field. The authors reported that k increment in the presence of field increased with increasing volume fraction. Enhancement in k was observed upto a critical field strength beyond which k showed a decreasing trend. The enhancement in k upto the critical field was attributed to the increasing aspect ratio of the field induced aggregates with increasing field strength (as the aggregates grew in length). Beyond the critical field the decrease in k was attributed to zippering transitions that decreased the aspect ratio of the aggregates. A schematic showing variation in k with the strength of the applied field is shown in **Fig. 1.9**. The

authors also studied the effect of particle size (2.8-9.5 nm) on k enhancement and they observed that the ferrofluid composed of the smallest particles (2.8 nm) did not show enhancement with the applied field owing to weak dipolar interactions due to which field induced aggregation was not possible. With increasing particle size and dipolar interaction between particles, k increment in the presence of field was larger (highest k enhancement was obtained for the ferrofluid composed of particles of average size 9.5 nm). Experiments performed by various researchers confirmed that enhancement in k was observed when heat flux and the direction of applied magnetic field was parallel[151]. Significant enhancement was not observed when the heat flux and applied field was perpendicular to each other[152]. In a water based ferrofluid, Gavili et al.[153] obtained maximum enhancement of 200% in k when the direction of heat flux was parallel to the direction of applied field. Lenin et al.[154] probed the role of primary and secondary surfactant layers on thermal transport of lauric acid coated magnetite ferrofluid. The authors observed that stability of ferrofluid reduced with secondary surfactant coating which resulted in aggregation even in the absence of magnetic field leading to high k values for the ferrofluid with particles having secondary surfactant coating (without magnetic field). However, in the presence of magnetic field, the more stable ferrofluid with only primary surfactant coating displayed higher k enhancement. The poor response of the system with secondary surfactant coating was attributed to the presence of large amount of non-magnetic layer around the nanoparticle surface. The authors also probed the effect of unsaturation in the fatty acid surfactant layer around the magnetic nanoparticle surface on thermal conductivity[155]. The authors reported that significant aggregation was observed in the ferrofluid system with saturated fatty acid surfactant even in the absence of magnetic field and the enhancement in k in the presence of magnetic field was not a significant as that observed in ferrofluids composed of

unsaturated fatty acid coated nanoparticles where aggregation of particles was not observed in the absence of magnetic field. Key findings of selected journal articles on thermal transport of ferrofluids in the presence of magnetic field are indicated in **Table 1.2**.

Table 1.2: Key findings of selected journal articles on magnetic field tunable thermal conductivity of ferrofluids.

Particle/Base fluid	Size	Concentra-tion	Key findings	Ref.
Fe/water	26 nm	1-5 vol.%	• In the absence of magnetic field, k increased with increase in concentration. • No enhancement in k when magnetic field is perpendicular to heat flux • Observed increase in k when field is parallel to heat flux direction. Increase became more prominent with increasing particle concentration.	[156]
Fe_3O_4/kerosene	6.7 nm	0.031-6.3 vol.%	• In the absence of magnetic field, no enhancement in k upto 1.71 vol.% beyond which k increased linearly with particle concentration. • For lowest concentration (0.031 vol.%) k was independent of applied field. • With increasing particle loading higher field induced k enhancement was observed. • Ruled out role of microconvection in k enhancement. Results supported effective heat transport through field induced aggregates. • Observed a decrease in k when field strength is increased beyond a critical value.	[136]
Fe_3O_4/kerosene	2.8-9.5 nm	5.5 vol.%	• In the absence of magnetic field ferrofluid containing larger particles displayed higher k. • Ferrofluid with larger particles displayed higher k in the presence of magnetic field.	[157]

Fe_3O_4/kerosene	9.9 nm	1.115-4.7 vol.%	• k enhancement was observed beyond a critical magnetic field strength and critical particle concentration. • k was found to be independent of temperature (25-65 ^{0}C)	[158]
Fe_3O_4/water Fe_3O_4/heptane	10 nm 10 nm	1.63 wt.% 1-7 wt.%	• Better k enhancement, under low field strength and particle concentration, was observed when a temperature gradient parallel to field direction was present. • The enhancement was attributed to thermomagnetic convection.	[159]
Fe_3O_4/kerosene	3-10 nm	0.031-1.71 vol.%	• k was nearly independent of magnetic field strength and concentration of particles when the direction of applied field was perpendicular to the direction of heat flux. • Upon varying field orientation with respect to direction of heat flux, maximum enhancement was observed for 0^0 and the k enhancement decreased with increasing deviation. For perpendicular direction no k enhancement with field was observed • When the field direction and heat flux direction was parallel, k enhancement was larger for larger volume fraction which was attributed to increased dipolar interaction • The decrease in k beyond a critical magnetic field strength was attributed to zippering transitions that decreased the aspect ratio of the aggregates.	[151]
Fe_3O_4/water	10 nm	5 vol.%	• In the absence of magnetic field significant enhancement in k was not observed. • Obtained significant enhancement in k with magnetic field application. • On turning off the magnetic field, the value of k decreased to the zero field value gradually like an exponential decay. • Increasing temperature decreased field	[153]

			dependent k drastically.	
Fe_3O_4/synthetic ester	13 nm	8.56 vol. %	• When heat flux and magnetic field were parallel, k enhancement was observed • When heat flux and magnetic field were perpendicularly aligned, a decrease in k was obtained.	[152]
Fe/silicone oil	20 nm	0.1-0.9 vol.%	• Ferrofluid composed of bare Fe nanoparticles was not stable and displayed fluctuating k values while surface modified Fe ferrofluid was stable with repeatable k values.	[160]
Fe_3O_4/water $CoFe_2O_4$/water	10 nm 15 nm	0.5-4.8 vol.%	• Fe_3O_4 ferrofluid gave higher k enhancement at lower field strengths when compared to $CoFe_2O_4$ ferrofluid. • Both fluids displayed k enhancement with increasing particle concentration and field strength.	[161]
$Mn_{0.6}Zn_{0.4}Fe_2O_4$ /transformer oil	8 nm	1.6-10.3 vol.%	• In the absence of magnetic field, higher volume fractions of nanoparticles resulted in k enhancement which was lower than that predicted by Maxwell's theory. Lower k value was attributed to aggregation of nanoparticles owing to reduced compatibility of particles with the base fluid. • For a fixed magnetic field, k was found to increase with time initially, attain a maximum and then decrease. This behavior was attributed to the temporal evolution of aggregates.	[162]
Fe_3O_4/kerosene	10.6 nm	0.5-7.2 vol.%	• Significant enhancement in k is possible when four parameters, namely, particle size distribution, volume fraction, coupling constant and Langevin parameter, are such that field induced aggregates form and the density of aggregates are high. • To avoid sedimentation of particles and huge enhancement in viscosity in the presence of magnetic field, the size and volume fraction of particles should be	[163]

			appropriately chosen.	
Fe_3O_4/water	60 nm	0.86 vol.%	• In comparison with TiO_2/water nanofluid, ferrofluid was found to give higher k enhancement with the additional benefit of finer control over aggregate size and aggregate growth direction without compromising stability of the nanofluid.	[164]
Fe, Co, Ni/ethylene glycol, heat transfer oil	35-45 (Fe) nm, 60-80 (Co) nm, 30-40 (Ni) nm	0-7 vol.%	• Fe based ferrofluid gave higher k enhancement than Co and Ni which was attributed to the higher saturation magnetization of the former. • The critical magnetic field beyond which k decreases shifts towards smaller field strength for ferrofluid with lower base fluid viscosity owing to the easier movement of particles in lower viscosity liquids.	[165]
Fe_3O_4/toluene	6, 7 nm	0.25-6 vol.%	• Ferrofluid composed of magnetite coated with stearic acid (18 carbon chain) displayed lower critical concentration (beyond which k enhancement was observed) than capric acid (10 carbon chain) coated magnetite ferrofluid which was attributed to the formation of aggregates in the former. • At higher magnetic field strengths ferrofluid with capric acid coated magnetite particles gave higher k enhancement due to easy aggregation of particles with shorter surfactant.	[166]

1.7 Wetting properties

1.7.1 Nanofluids and wetting

Spreading of fluids on solid substrates has been thoroughly researched over the years on account of the crucial role wetting plays in many industrial applications[167]. Wetting, which is

the interaction of a liquid with a solid substrate, plays an important role in many applications from printing (ink-jet printing, 3-D printing, bio-printing) to coating applications that are instrumental to aerospace, automotive, marine industries etc. Nanofluids display enhanced wetting properties than the base fluid and the wetting properties can be tailored easily[168]. Wetting is generally characterized through contact angle studies. Depending on the mode of measurement two different contact angles can be defined[169]: Equilibrium (static) contact angle and dynamic contact angle. Equilibrium contact angle is the contact angle made by a sessile droplet on a smooth, homogenous solid substrate and this wetting which does not involve motion of the droplet is called static wetting. Some of the factors that affect the equilibrium contact angle are volume of the droplet, roughness of the solid substrate, nature of interaction at the contact line etc. Dynamic contact angle is the contact angle made by a droplet in motion on the solid substrate and this wetting with advancing contact line is called dynamic wetting.

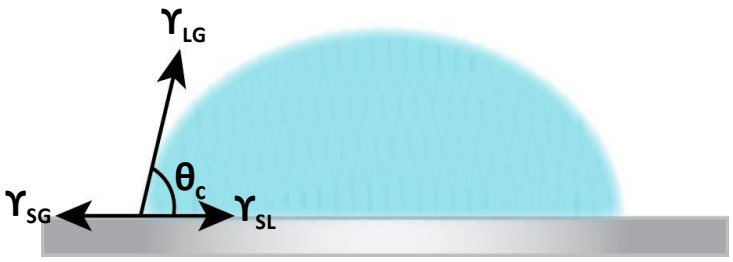

Figure 1.10: Schematic depicting the surface tension acting on a sessile fluid droplet on a solid substrate.

In 1805 Thomas Young reported the first expression relating the equilibrium contact angle for a sessile droplet on a solid substrate to the surface tensions acting on it. The Young's equation, given by[169]

$$\cos\theta_C = \frac{\Upsilon_{SG}-\Upsilon_{SL}}{\Upsilon_{LG}} \tag{1.31}$$

where θ_C is the contact angle, Υ_{LG}, Υ_{SG} and Υ_{SL} is the interfacial tension between liquid-gas, solid-gas and solid-liquid (see **Fig. 1.10**), respectively, was obtained by considering the fact that for a solid-liquid-gas system in thermodynamic equilibrium the sum of the horizontal components of the surface tension at the three phase contact line must be zero. For $\theta_C > 90^0$ the liquid is said to have low wettability for the solid substrate used and for $\theta_C < 90^0$ the liquid is said to be highly wettable. Complete wettability is achieved when $\theta_C = 0^0$.

In contrast to simple liquids, wetting properties of nanofluids are influenced by interaction between the nanoparticles in the nanofluid and also interactions between particles and substrate and particles and base fluid[168, 169]. The change in wetting properties with the addition of nanoparticles to a base fluid is attributed to the structure disjoining pressure that arises as a result of ordering of nanoparticles at the three phase interface[170]. This ordering increases the overall entropy of the droplet by allowing increased freedom to the other nanoparticles in the bulk. Kondiparty et al.[171] reported that the particle structure within the three phase wedge affects the spreading of the nanofluid on the solid substrate. The nature of interaction between the particles and between the particles and the solid surface affects the structural disjoining gradient which in turn affects wetting. Sefiane et al.[169] reported that wetting and spontaneous spreading of nanofluids on a substrate can be tuned by varying volume fraction of nanoparticles and size of the nanoparticles. Studies on wetting of alumina nanofluids on a Teflon coated substrate revealed that the contact line velocity increased upto 1 wt.% beyond which a decrease was observed. The authors hypothesized that this could be due to the dominating viscous forces that overcome the structural disjoining pressure beyond 1 wt.% or due to the adsorption of the nanoparticles on the substrate. Depending on the nature of interaction between the nanofluid and the substrate, wetting can be enhanced or diminished relative to the

wetting properties of the base fluid. In general smaller particles were reported to bring more significant changes to wetting properties than larger particles[172].

1.7.2 Field induced wetting of ferrofluids

Wetting of ferrofluid droplets is even more interesting than that of a simple nanofluid owing to the possibility of manipulating the droplet shape and flow across a surface through the application of an external magnetic field. For example, placing a permanent magnet beneath a ferrofluid droplet causes it to flatten and the droplet can be moved across the surface by moving the magnet[173]. In a homogenous magnetic field, like a solenoidal field, a ferrofluid droplet will elongate along the direction of the magnetic field[174]. The droplet shape is determined by the balance of gravitational, magnetic and surface forces. If the droplet volume is small, effect of gravity can be ignored and the effect of magnetic and interfacial forces can be described conveniently using the magnetic Bond number given by[175]

$$N_B = \frac{\mu_0 H^2 R}{\Upsilon} \tag{1.32}$$

where R is the diameter of the droplet and Υ is the surface tension. The interfacial tension changes with the strength of the applied magnetic field due to the rearrangement of the nanoparticles within the droplet and at the interface. The work of Kalikmanov[176] revealed that the dipole interactions between the particles lead to a non-uniform particle distribution which was responsible for the weak increment of surface tension with field strength. Experimentally it was demonstrated that ferrofluids with low magnetic permeability underwent continuous deformation of droplet shape profile as the strength of the applied magnetic field was increased[177, 178]. However, a system with high magnetic permeability undergoes continuous deformation only upto a critical magnetic field strength beyond which a sudden change in the

drop shape profile from an ellipsoidal curvature to an elongated cone was recorded. Gaffari et al.[179], through simulations, demonstrated that ferrofluid droplets of larger volume displayed larger deformation in the presence of magnetic field. Additionally, they also reported that ferrofluid having higher magnetic susceptibility deformed more with increasing magnetic field strength. Manukyan et al.[180] studied magnetic field induced wetting behavior of an oil based ferrofluid and water based magnetic paint on a hydrophobic surface. The authors observed that when the magnetic field is applied perpendicular to the solid substrate the oil based ferrofluid displayed a decreasing contact angle with increasing field strength upto a critical field beyond which the contact angle showed an increasing trend while the water based paint, owing to negative magnetic susceptibility, displayed an increase in contact angle upto a critical field strength beyond which a decreasing trend was observed. Zhu et al.[181] reported that applying a magnetic field parallel to an oleophobic surface on which a ferrofluid droplet is placed lead to the elongation of the droplet along the substrate. With increasing field strength the elongation also increased, though for field strengths beyond saturation magnetization deformation decreased.

Ferrofluids are also impregnated into surfaces or templates to control the wetting properties of other liquids[174]. Recently, an ice resistant (delayed ice formation) surface was made by using silicon wafers coated with 300 micron thick layer of oil based ferrofluid[182]. On application of an external magnetic field, the ferrofluid was pushed against the substrate which resulted in a magnetic buoyancy effect forcing water droplets to float near the ferrofluid surface thus successfully preventing ice nucleation (ice formation temperature was reduced to -34 ^{0}C) as direct contact between water droplets and the silicon wafer is prevented. Khalil et al.[183]

experimentally demonstrated that textured surfaces impregnated with ferrofluid can be used to propel viscous, conducting and diamagnetic liquids with the help of weak magnetic fields.

Ferrofluids are used in many microfluidics applications where an externally applied magnetic field is used to control ferrofluid droplet generation, coalescence and separation of droplets[174]. Nguyen et al.[184] observed that ferrofluid droplets can be forced to move across a solid substrate at the same velocity as a magnet provided the magnetic field produced by the magnetic is strong enough to dominate over capillary forces and friction.

1.8 Motivation

Magnetic field tunable physical properties of ferrofluids have inspired many technological applications. Understanding aggregation dynamics is vital for efficient utilization of ferrofluids for such applications. Aggregation dynamics in ferrofluids is extremely complex being highly sensitive to multiple variables like particle size distribution, nature of surfactant coating, particle morphology and volume fraction, strength of applied magnetic field, ramp rate of field application etc[52, 62, 65, 75, 88, 89]. Hence the field induced changes in the physical properties of one ferrofluid system can drastically be different from another. For example a ferrofluid system may show drastic improvement in thermal conductivity in the presence of magnetic field with minimal viscosity enhancement while another system of same volume fraction and similar average crystallite size may not show notable enhancement in thermal conductivity when exposed to magnetic field. The focus of most of the available research is on capturing the rheological, thermal or optical response of ferrofluids on modification of particle morphology, surface functionalization, varying particle size and volume fraction etc. without examining the differences in aggregation dynamics which is responsible for the observed

physical properties brought about by varying these parameters. Lack of insight into aggregation dynamics lead to conflicting reports on field tunable physical properties of ferrofluids.

1.9 Objectives

The main focus of this thesis is on the effect of aggregation dynamics on magnetic field tunable thermal, rheological and wetting properties of ferrofluids. The major objectives of the thesis are given below

- To probe the effect of particle size distribution on thermo-rheological properties of ferrofluids.
- To obtain the optimum conditions to achieve high thermal conductivity with minimal viscosity enhancement.
- To probe the effect of magnetic field ramp rate on thermo-rheological properties of ferrofluids.
- To determine the conditions under which a ferrofluid exhibits aging and to explore the glass-like dynamics displayed by it using rheology.
- To determine the impact of field induced aggregation on wetting properties of sessile ferrofluid droplets.
- To study the microstructure of ferrofluid under magnetic field using a phase contrast optical microscope, thereby obtaining direct correlation between the microstructure and macroscopic physical properties of ferrofluid.

1.10 Overview of the thesis

The thesis is composed of seven chapters, the details of which are summarized below.

Chapter 1 gives an introduction to soft matter, smart materials, ferrofluids, field induced aggregation and the factors affecting magnetic field tunable physical properties of ferrofluids. **Chapter 2** briefly discusses synthesis of ferrofluid and lists the details of the ferrofluid samples used for all the experimental studies included in the thesis and the experimental techniques used for their characterization. Details of the rheological and thermal conductivity measurement protocols are described along with contact angle measurement procedure. **Chapter 3** presents the study on field tunable thermal conductivity of four different ferrofluids having different particle size distributions. All four systems were kerosene based with oleic acid coated magnetite nanoparticles. The difference in aggregation kinetics of the ferrofluid systems which arises due to differences in the particle size distribution was probed and the subsequent differences in the thermal and rheological properties were explored. **Chapter 4** describes the impact of applied magnetic field ramp rate on field tunable thermal conductivity of ferrofluid. The effect of particle size distribution on the field induced microstructure formed at different ramp rates of applied field and the corresponding consequences on thermal transport is detailed here. **Chapter 5** provides experimental results on rheological behavior of ferrofluids under different magnetic field quench rates. The results of creep tests obtained at different waiting times which indicate aging is described in this chapter. **Chapter 6** deals with the effect of magnetic field induced aggregation on magnetowetting of ferrofluid suspensions. Sessile ferrofluid droplet, on being exposed to external magnetic field, elongated along the field direction and effect of particle size distribution on the extent of deformation is detailed in this chapter. **Chapter 7** summarizes the obtained results and conclusions. The future scope of this work is also included here.

Chapter 2 Materials and Methods

2.1 Synthesis of ferrofluid

All the iron oxide nanoparticles used for ferrofluid preparation were synthesized via co-precipitation method[45, 185]. The iron salts required for synthesis of magnetic nanoparticles ($FeCl_2.4H_2O$, $FeCl_3.6H_2O$), 25% ammonium hydroxide, oleic acid, 35% hydrochloric acid, acetone and hexane were all purchased from E-Merck and were of GR grade and used without further purification. MilliQ water of resistivity 15 MΩcm was used for synthesis. Freshly prepared iron salt solutions of 0.2 M $FeCl_2.4H_2O$ and 0.4 M $FeCl_3.6H_2O$ were mixed in 1:1 ratio and stirred at a speed of 1000 rpm. Ammonia was added to the salt solution till the pH reached 10, following which 20 mL of oleic acid was added. The pH was then adjusted to 9.5 and the temperature increased to 70 ^{0}C. The solution was kept at the same temperature and stirring speed for 30 minutes to ensure surfactant binding on the nanoparticle surface. The protonation of unadsorbed and adsorbed ammonium oleate to oleic acid and removal of excess ammonia was achieved by raising the temperature to 79 ^{0}C. The oleic acid capped nanoparticles were triply washed with distilled water at temperature of 60 ^{0}C, until the pH was 7 to remove ionic impurities. The washed particles were dispersed in hexane. To remove excess surfactant, the nanoparticles were agglomerated by adding acetone to hexane and the resulting mixture was centrifuged at 2500 rpm for about 30 minutes. This process was repeated a few times. The washed oleic acid coated nanoparticles were vacuum dried at 35 ^{0}C for 48 hrs following which the particles were dispersed in kerosene at the desired volume fractions.

2.2 Rheology

2.2.1 Introduction to rheology

Rheology is the study of "deformation and flow of matter"[186]. The term rheology originates from the Greek work "rhein" which means "to flow" and it was coined by Professor Bingham. Rheology involves the study of a wide range of materials from Hookean elastic solids to Newtonian viscous liquids. Many materials are neither Hookean solids nor are they Newtonian liquids. However, every material deforms, some over time intervals less than a millisecond while others take years. In the Old Testament, Deborah is claimed to have said, "The mountains flowed before the Lord…" which is in sync with the idea that "everything flows if you wait long enough"[186]. The glass windows of the Cathedral of Chartres in France are proof of this[187]. Over the time period of six hundred years the glass molecules of the window pane had flowed downwards under the effect of gravity as a result of which the top part of the glass pane has become paper thin while the thickness of the lower part had nearly doubled. Every material has a characteristic time over which it deforms. Hence, a material may appear solid-like if the time period of measurement is shorter than the material relaxation time. To characterize the fluidity of a material, a dimensionless number called Deborah number (De) was defined which is the ratio of characteristic time of deformation of a material to the time of observation[186]. Large De corresponds to solid-like response and low De for liquid-like nature.

Solids can resist an applied stress or they show an elastic response while liquids deform continuously in response to the applied stress[188]. The response of many materials cannot be quantified as perfectly viscous or perfectly elastic. When deformed such materials will have a

viscous force component as well as an elastic force component and these materials are called viscoelastic[189].

2.2.2 Rheological parameters

The rheological response of materials are usually studied as a function of shear rate or frequency of deformation[190]. The fundamental rheological parameters are defined using the two-plates model[6]. A schematic representing the two-plates model is shown in **Fig. 2.1**.

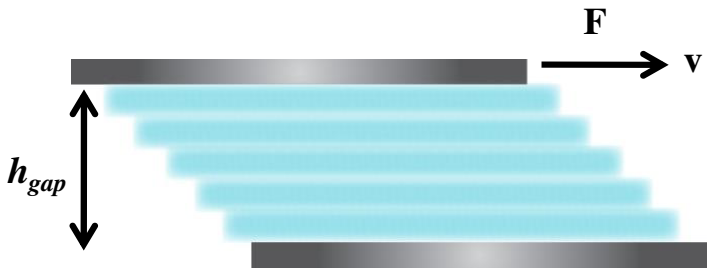

Figure 2.1: Schematic representation of the two-plates model.

The material to be studied is confined between two plates at a gap height h_{gap}. The upper plate of area A_{plate} is used to shear the material while the bottom plate remains stationary. The common rheological parameters that are defined using this model are

- Shear stress (τ): It is defined as the shear force F applied per unit area (in this case, area to be considered is the area of the rheometer shearing plate A) and it is given by

$$\tau = \frac{F}{A} \tag{2.1}$$

  The SI unit of shear stress is Nm^{-2} or Pa.

- Shear rate ($\dot{\gamma}$): Assuming laminar flow, shear rate is defined as the velocity of the upper plate v divided by the gap height.

$$\dot{\gamma} = \frac{\mathrm{v}}{h} \tag{2.2}$$

The SI unit of shear rate is s^{-1}.

- Viscosity (η): Every fluid in motion offers a resistance to flow which is quantified in terms of viscosity. For ideally viscous fluids viscosity at a given temperature is given by

$$\eta = \frac{\tau}{\dot{\gamma}} \tag{2.3}$$

The SI unit of viscosity is Pa.s. Shear viscosity is often termed as dynamic viscosity. When the flow of Newtonian liquids are characterized using capillary viscometers where gravity is responsible for initiating flow, the density of the fluid medium plays a crucial role in determining flow and kinematic viscosity, which is the dynamic viscosity divided by the density of the material, is used to quantify the resistance of the material to flow[187].

2.2.3 Steady shear rheology

Steady shear rheology is used to determine viscosity of materials as a function of applied shear rate. These experiments involve steady state flow where the stress response have equilibrated to the imposed shear rate[191]. Depending on the material response, fluids are classified into different categories.

2.2.3.1 Newtonian fluids

Under simple shear, Newtonian fluids display linear relationship between shear rate and shear stress as a result of which viscosity is independent of the degree and duration of applied shear (eqn. (2.3))[6, 186, 187]. The behavior of Newtonian liquids is described using the dashpot model. In this model the behavior of a Newtonian fluid is mimicked by the motion of a piston

through an annular gap containing a fluid. The velocity of the piston is proportional to the force driving it and the proportionality factor is the resistance offered by the fluid, i.e., the viscosity of the fluid. If the external force is constant, then the velocity of the dashpot fluid is constant, i.e., the deformation rate is constant. After the external deformation force is removed, the fluid remains in the deformed state. Some examples of Newtonian fluids are pure solvents like water, oils, dilute colloidal dispersions and dilute polymer solutions.

2.2.3.2 Non-Newtonian fluids

Non-Newtonian fluids, when sheared, display non-linear relationship between shear rate and shear stress[186, 187, 190]. Hence, viscosity is no longer independent of the applied shear. The relationship between shear stress and shear rate can be described by a power law of the form,

$$\tau \, \alpha \, \dot{\gamma}^{n} \tag{2.4}$$

where n is the power law index. When $n < 1$ the fluid is classified as a shear thinning fluid and $n > 1$ indicates shear thickening nature.

For shear thinning fluids, the stress increases sublinearly with the applied shear rate and viscosity decreases as the shear rate increases. Many suspensions, pastes, emulsions and polymer solutions exhibit shear thinning[186, 187]. The decrease in viscosity with increasing shear rate is often due to structural changes of the material brought about by the external shear. As the shear rate increases, decrease in viscosity can be brought about in many ways, for example, rod shaped particles in a colloid will align along the shear direction at higher shear rates, chain like polymers, either in a melt or in a solution, can disentangle, orient and stretch along shear direction, elastically deformable units like emulsion droplets can be reshaped to reduce the

diameter and aggregates present in a colloid can be broken apart by shear, all of which can reduce viscosity.

Shear thickening or dilatant materials display increased viscosity with increasing shear rate because of the larger than linear increase in shear stress with shear rate. This flow behavior is in general exhibited by highly concentrated suspensions, for example, highly concentrated ceramic or starch dispersions, natural rubber, highly filled elastomers etc[192]. Under rest conditions or low shear rates, dilatant materials display shear thinning nature as under low shear, the particles in the dense suspension can rearrange into new configurations easily as the base fluid lubricates their motion, thus reducing friction between particles. Beyond a critical shear, drastic increase in viscosity occurs, the increase being discontinuous (sudden jump in viscosity) or continuous. Many mechanisms have been proposed over the years to explain shear thickening. The widely accepted ones are formation of hydroclusters (particles under high shear form clusters that increase lubrication drag forces between them), order-disorder transition (under low shear ordered layers of fluid are present which transitions to a disordered state at higher shear rate which again increases drag force between particles) and jamming of particles under high shear which increases friction between particles[193]. A schematic showing the rheological response of Newtonian, shear thinning and shear thickening fluids is shown in **Fig. 2.2**.

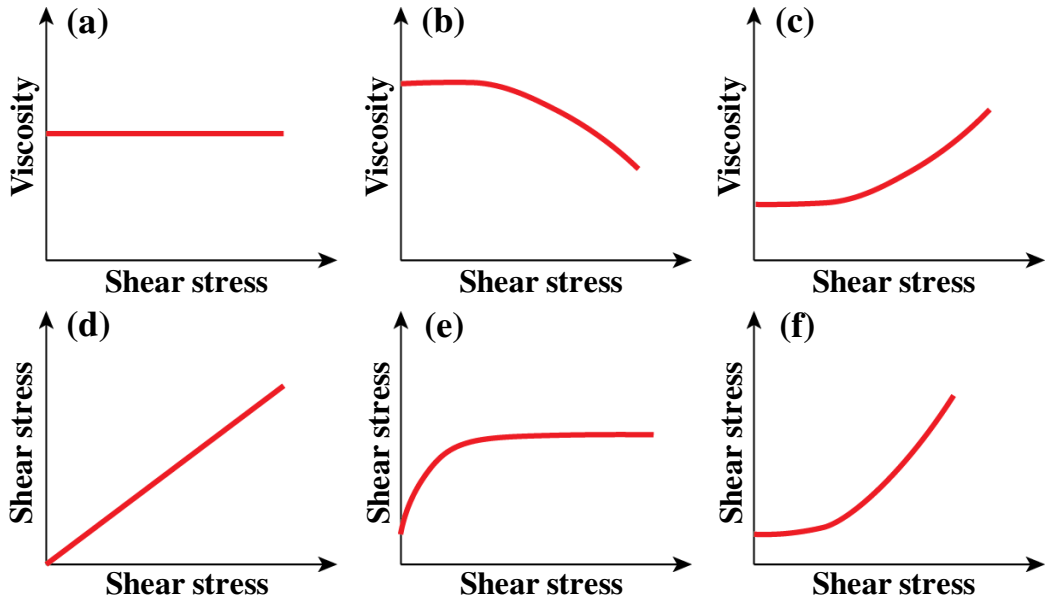

Figure 2.2: Rheological response of Newtonian ((a) & (d)), shear thinning ((b) & (e)) and shear thickening ((c) & (f)) fluids.

2.2.3.3 Time dependent rheological behavior

The rheological parameters of many materials depend not only on the magnitude of the applied shear but also on the duration of shear and the previous kinematic history. Time dependent fluid behavior can be broadly classified into two categories depending on the response of materials to shear applied over a period of time: Thixotropy and rheopexy.

Thixotropic systems are those which when sheared displays a decrease in viscosity but when the shear is stopped, the viscosity increases to the initial value owing to structural regeneration[194, 195]. Many pastes, creams and gels are thixotropic. Ketchup, paints, coatings, drilling fluids etc. display thixotropic nature. Breakdown of microstructure as a result of shear is typically much faster (milliseconds to few minutes) than the time taken (hours to days) to rebuild

after removal of shear. Thixotropy is studied by applying a high shear load for a short duration of time and observing the viscosity change as a function of time after removal of shear[6].

Rheopectic materials are those which when sheared display increased viscosity which decreases to the initial value on removal of shear. Rheopexy is generally displayed by suspensions containing anisometric particles[6, 186, 187]. Unlike thixotropic fluids, in rheopectic materials external shear lead to build-up of structure. Same material can display both thixotropic and rheopectic behaviors under appropriate combinations of shear conditions and concentration. Schematic representing the time dependent rheological response of thixotropic and rheopectic fluids is shown in **Fig. 2.3**.

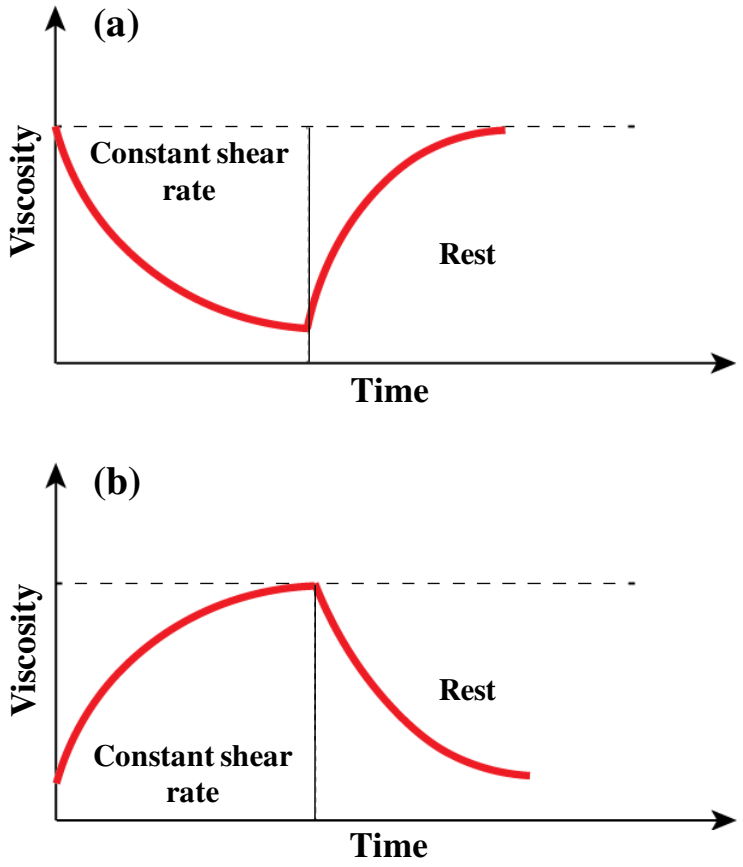

Figure 2.3: Time dependent rheological behavior of (a) thixotropic and (b) rheopectic fluids.

2.2.4 Oscillatory shear rheology

Oscillatory rheology is a common and useful way to probe time dependent properties of soft materials. When a sinusoidal strain of the form

$$\gamma(t) = \gamma_0 \sin(\omega t) \tag{2.5}$$

where oscillation frequency is given by ω and γ_0 is the amplitude of the applied strain, is imposed on a soft material, the stress response of the material is also time varying and takes the form

$$\tau(t) = G\gamma(t) = \tau_0 \sin(\omega t + \delta) \tag{2.6}$$

where G is the shear modulus of the material and δ is the phase lag. For an ideally elastic material $\delta = 0^0$, indicating that the stress response is completely in phase with the applied strain and $\tau(t) = G\gamma(t) = \tau_0 \sin(\omega t)$ [6, 191]. For ideally viscous materials, $\delta = 90^0$ indicating that the stress response of the material is out of phase with respect to the applied strain by 90^0. For viscoelastic materials the phase lag is between 0^0 and 90^0 and δ depends on the oscillation frequency ω (see **Fig. 2.4**).

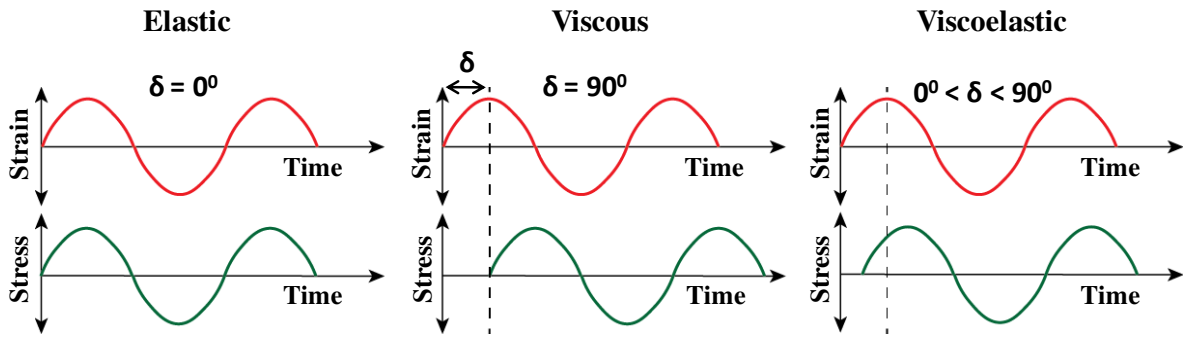

Figure 2.4: Schematic showing the stress response of elastic, viscous and viscoelastic materials to a sinusoidal strain.

Thus, the rheological response of viscoelastic materials contain both elastic and viscous contributions and the stress response can be divided into two parts,

$$\tau(t) = G'\,\gamma_0 \sin(\omega t) + G"\gamma_0 \cos(\omega t) \tag{2.7}$$

where G' is the storage or elastic modulus and $G"$ is the loss or viscous modulus. If the strain deformation is written as a complex function, $\gamma(t) = \gamma_0 e^{i\omega t}$, then the stress response takes the form

$$\tau(t) = G^*(\omega)\gamma_0 e^{i\omega t} \tag{2.8}$$

where $G^*(\omega)$ is the complex shear modulus given by $G^*(\omega) = G'(\omega) + iG"(\omega)$. For a given ω a material is said to be liquid-like if $G" > G'$ and the solid-like response is when $G" < G'$.

2.2.5 Rheometer

For estimation of flow properties, rotational rheometers are preferred over capillary and falling-ball viscometers owing to the sophisticated designs of the former available in the market making estimation of complex rheological characteristics of materials easier to probe with high accuracy. Rotational rheometers come in two different test modes: controlled shear rate (CSR) and controlled shear stress (CSS) mode. In the CSR mode rotational speed or shear rate is preset and the torque is measured, from which the rheological parameters are estimated. In the CSS mode, torque or shear stress is preset and the rotational speed or shear rate is measured[6, 187].

In rotational rheometry different types of measuring geometries are available. They are

- Parallel plate geometry: In this geometry the material to be probed is confined between two parallel plates at a gap height h. The top measuring plate rotates with an angular velocity Ω.

In this geometry, shear rate is not constant or homogeneous throughout the gap height (shear rate is maximum at the edge and reduces towards the center) and the shear rate is given by[6]

$$\dot{\gamma} = \frac{R_{plate}\Omega}{h} \tag{2.9}$$

where R_{plate} is the radius of the shearing plate. This geometry is most appropriate for rheological characterization of highly viscous materials like elastomers, gels, pastes etc. and dispersions containing large particles.

- Cone and plate geometry: In this geometry the top measuring plate is a flat circular cone and the bottom plate is stationary. Generally the cone angle α_{cone} is 1^0. Measuring systems with larger angles, less than 4^0, are also available. Throughout the shear gap shear rate is constant and it is given by[6]

$$\dot{\gamma} = \frac{\Omega}{tan\alpha_{cone}} \tag{2.10}$$

This geometry is suitable for less viscous materials and only small quantity of sample is required for a test. In this geometry the maximum particle size (<50 μm) is limited.

- Concentric cylinder geometry: This geometry consists of two concentric cylinders. The outer cylinder is stationary and the inner cylinder is the measuring system and it is used to shear the material which is confined between the two cylinders. The shear rate is given by[6]

$$\dot{\gamma} = \frac{1}{r'^2}\frac{2R_i^2R_o^2}{R_o^2-R_i^2}\Omega \tag{2.11}$$

where R_i is the radius of the inner rotating cylinder, R_o is the radius of the outer cup and $R_i < r' < R_0$. This geometry is used for probing low viscosity fluids and it yields highly accurate results even at very high shear rates as low surface tension liquids cannot flow out

of the shear gap. However, this geometry requires large amount of sample and for viscous samples, artifacts introduced by air bubbles poses a problem. Schematic representing the different measuring geometries are shown in **Fig 2.5**.

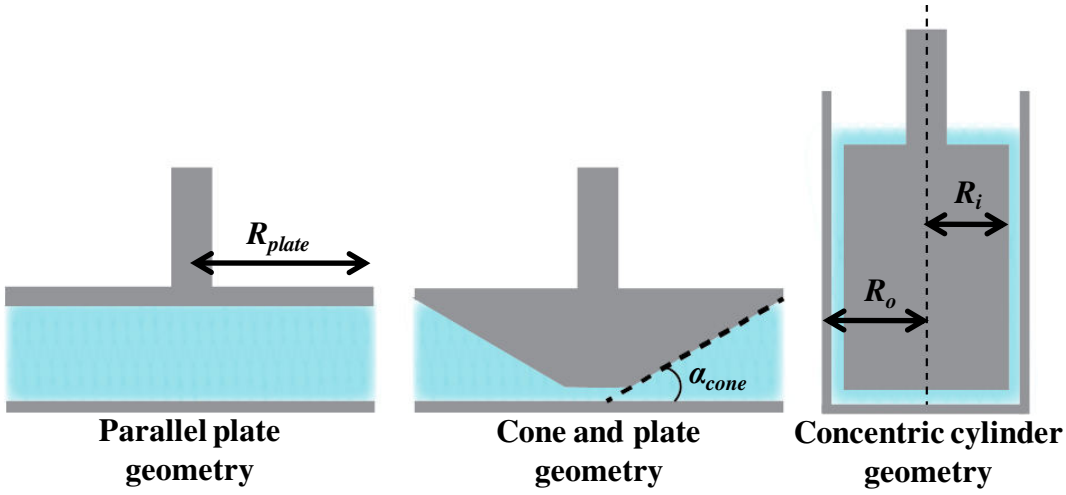

Figure 2.5: Different measuring geometries used in rheometry: Parallel plate, cone and plate and concentric cylinder geometry.

2.2.5.1 Rheometer design

Rheometer (MCR301) that operates in controlled shear rate mode equipped with a magnetorheological device (Anton Paar, Germany) was used for obtaining all the rheological data included in this thesis. This rheometer has an air bearing supported synchronous electrically commutated motor. Permanent magnets are attached to the rotor of the motor drive. Coils with opposite polarity produce magnetic poles in the stator. The stator coils and the magnets present in the rotor attract each other ensuring that a rotating flux of current in the coil windings provides a frictionless movement to the rotor. The input current to the stator coils is used to set and measure the torque of the motor. This equipment offers precise torque control owing to the linear relationship of the torque and input current to the stator coil. A high resolution optical encoder

which is based on data oversampling technology offers highly accurate measurement and control of angular deflections (as low as 100 nanorad). Two air bearings support the motor and they are not perturbed by external influences. The air bearings are optimized for rigidity, drift stability and robustness. The range of magnitude of torque that can be measured by the rheometer in the steady shear mode is 0.05 μNm to 200 mNm and the torque resolution is 0.1 nNm. In the oscillatory mode the minimum magnitude of torque that can be measured is 0.01 μNm. Shear rate can be preset between 10^{-7} and 3000 min^{-1} and angular frequency can be varied between 10^{-5} and 628 $rad.s^{-1}$. The temperature is maintained during experiments using a chiller (Anton Paar Viscotherm VT2) with water as coolant. The magnetic field is generated by the instrument using a magnetorheological device equipped with Helmholtz coils for producing uniform magnetic field in the sample area. The strength of the magnetic field is varied by changing the current from a power supply, whose operation can be controlled using Rheoplus software which also controls the operating conditions of the rheometer along with data acquisition and analysis. The maximum flux density attainable within the shear gap is 1 T corresponding to 5 A of current. The rheometer also has a built-in demagnetizer to eliminate residual magnetic fields.

Parallel plate geometry was used for all the tests and the gap height was fixed at 0.1 mm. Before the start of all measurements, the sample was sheared at 100 s^{-1} for a time period of 60 s to eliminate shear history and ensure repeatability of tests. Then the sample was subjected to magnetic field of required strength for 60 s following which the rheological characterization was carried out.

2.3 Thermal conductivity measurements

Thermal conductivity measurements were made using transient hot wire method[196] using a thermal property analyzer from Decagon devices Inc. (KD2-Pro), USA. KD2-Pro has a Platinum wire probe that acts as both heat source and temperature sensor. The Pt sensor, which is immersed in the fluid, heats up the fluid via resistive heating of the wire brought about by a step increase in electrical power. The change in resistivity of the fluid in response to the given heat is obtained through a wheat stone bridge circuit that is built-in the KD2-Pro (see **Fig. 2.6**). The change in temperature of the fluid is estimated from the change in resistivity. Using Fourier's law, thermal conductivity is estimated using the equation,

$$k = \left[\frac{q}{4\pi(T_2 - T_1)}\right] ln\left(\frac{t_2}{t_1}\right) \tag{2.12}$$

where q is the heat produced by the Pt wire per unit length per unit time, T_2 is the temperature measured at time t_2 and T_1 is the temperature measured at time t_1. Transient hot wire method is an easy and low cost method which offers fast data acquisition. Each measurement comprises a 30 s equilibration period, 30 s heating period and a 30 s cooling period. During heating and cooling periods, temperature measurements are made at 1 s interval. The obtained temperature values are fit to exponential integral functions using nonlinear least square method and then k is calculated.

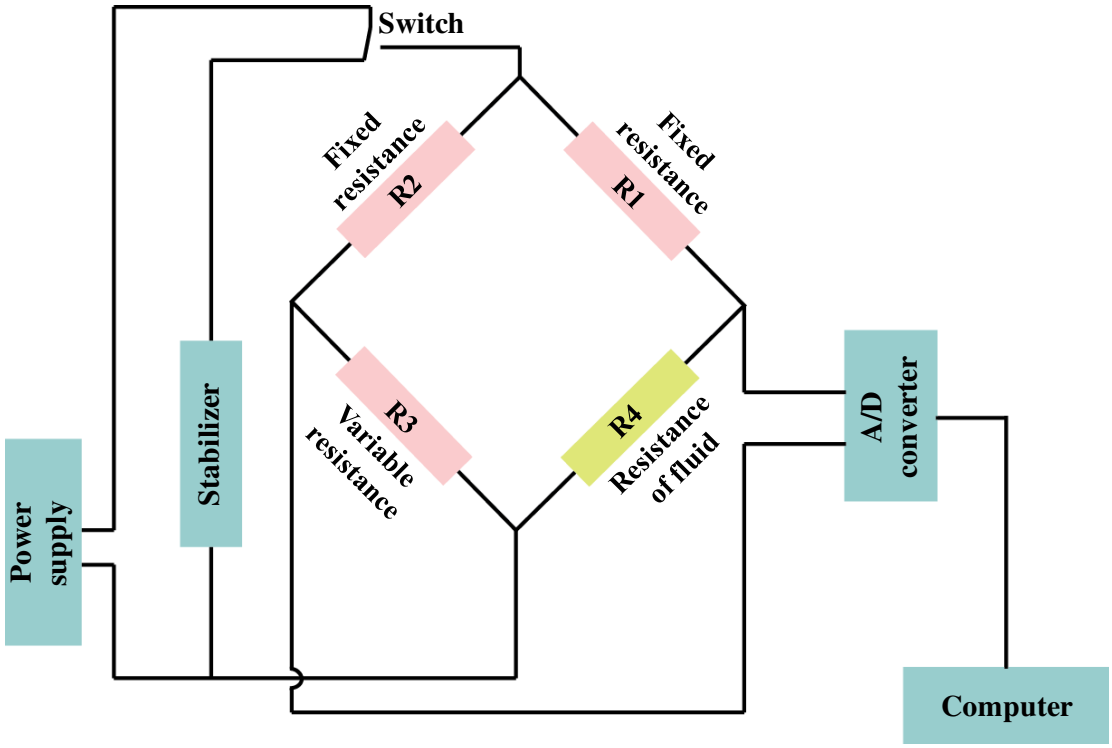

Figure 2.6: Schematic of transient hot wire experimental set-up.

The length of the Pt probe is 60 mm and its diameter is 1.28 mm. The range of thermal conductivity that can be measured by the probe is 0.02-2 $Wm^{-1}K^{-1}$. The probe is calibrated by measuring thermal conductivity of standard liquids like water, ethylene glycol, glycerol and kerosene. For field dependent studies, a solenoid was used for magnetic field generation. The strength of magnetic field was varied by changing the magnitude of current through the solenoid. Thermal conductivity measurements were taken after 30 s of setting the field to required strength.

2.4 Powder X-ray diffraction

The most widely used technique for crystal structure determination is powder X-ray diffraction (XRD)[197]. X-rays are used for probing crystal structure as the wavelength of X-

rays is comparable to the lattice spacing. XRD makes use of Bragg's law of diffraction which is given by

$$2d_{hkl}sin\theta = n\lambda_{X-ray} \tag{2.13}$$

where d_{hkl} is the spacing between lattice planes, θ and n are the Bragg angle and order of Bragg reflection, respectively and the wavelength of X-ray used to probe the sample is given by λ_{X-ray}. The X-ray source, the detector and the sample lie along the circumference of a focusing circle. Constructive interference occurs at specific directions depending on the phase of the diffracted X-rays. The average crystallite size is calculated using the Scherrer's equation given by

$$d_{crystallite} = \frac{0.89\lambda_{X-ray}}{\beta_{FWHM}cos\theta} \tag{2.14}$$

where β_{FWHM} is the full width at half maximum of the highest intensity peak measured in radians.

X-ray diffraction studies included in this thesis were performed using Rigaku Ultima IV. The X-ray diffraction pattern was recorded in the 2θ range, 20-80^0. The instrument uses CuKα X-ray radiation of wavelength 1.516 Å. The step size and scan rate was fixed at 0.02^0 and 2^0/minute, respectively. The software used for data acquisition and preliminary analysis is PDXL and the obtained diffraction patterns were compared to the patterns in the database of Joint Committee on Powder Diffraction Standards (JCPDS).

2.5 Dynamic light scattering

Dynamic light scattering (DLS) technique was used for the determination of average hydrodynamic size of the dispersed nanoparticles. This technique exploits the Brownian motion of the nanoparticles within the base fluid to obtain a correlation function from the time varying

speckle pattern that arises owing to the changing spatial distribution of the particles[198]. The size of the dispersed nanoparticles affects the correlation function. Smaller particles diffuse faster via Brownian motion than larger particles resulting in a faster decaying correlation function. The intensity auto correlation function is given by

$$g^{(2)}(q,t) = \frac{\langle I(q,t)I(q,t+\delta t)\rangle}{\langle I(q,t)\rangle^2} \tag{2.15}$$

where $I(q,t)$ is the scattered intensity at time t and $I(q,t+\delta t)$ is the scattered intensity at time $t+\delta t$. The wave vector is given by q. Electric field correlation function is obtained from the intensity correlation function using Siegert's relation which is given by

$$g^{(2)}(q,t) = 1 + \beta'\left|g^{(1)}(q,t)\right|^2 \tag{2.16}$$

where β' is a correction factor that depends on the scattering geometry. In the case of monodisperse particles the electric field auto correlation function takes the form of a single exponential function and can be expressed as

$$g^{(1)}(q,t) = e^{-\Gamma t} \tag{2.17}$$

where $\Gamma = Dq^2$ is the rate of relaxation. The translational diffusion coefficient of the particles is given by D. Hence by fitting the correlation function to an exponential function, D can be obtained, from which the hydrodynamic size is determined using the Stokes-Einstein equation,

$$d_{hydrodynamic} = \frac{k_B T}{3\pi\eta_c D}. \tag{2.18}$$

In the work detailed in this thesis the average hydrodynamic diameter was estimated using Zetasizer Nano ZS of Malvern instruments, UK. The experiments were performed in the back scattering geometry (173^0) at ambient temperature of 25 ^{0}C.

2.6 Vibrating sample magnetometer

Vibrating sample magnetometer (VSM) is used for probing the magnetic properties of materials. The foundation of operation of VSM is Faraday's law of induction which states that the induced electromotive force in a circuit is directly proportional to the temporal change of magnetic flux linked to the circuit[199]. The material to be studied is placed at the center of a constant magnetic field. The field aligns the magnetic domains or spins of the material along the magnetic field direction thus creating a magnetic field around the material. When the material is oscillated up and down, perpendicular to the applied field, a stationary detection coil experiences the time varying magnetic field of the vibrated material and consequently a voltage is induced in the detection coils. The induced current in the detection coil is proportional to the magnetization of the material. The magnetic properties of the magnetic nanoparticles studied here were obtained using a cryogen-free VSM (M/s Cryogenics, U.K.) and measurements were performed in the field range ± 2 T. All the measurement protocols are computer controlled.

2.7 Phase contrast microscopy

Phase contrast microscopy manipulates small spatial variations in phase to obtain corresponding variations in intensity of transmitted light[191]. Light first passes through an annular ring that is placed before the condenser lens and is then focused on the sample (see **Fig. 2.7**). The light either passes undeviated or it is diffracted with a change in phase depending on the sample composition. The undeviated and the diffracted light passes through the objective and then to the eyepiece through a phase ring whose purpose is to introduce an additional phase shift to the undeviated light to obtain better contrast. Depending on the refractive indices of the

different areas of the sample, certain areas will appear darker and certain areas appear brighter when compared to the uniform background.

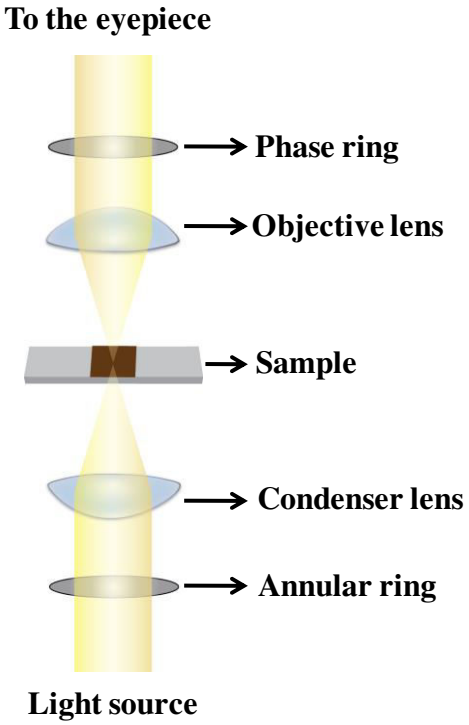

Figure 2.7: Schematic representing phase contrast microscopy.

2.8 Thermogravimetric analysis

Thermogravimetry is used to estimate the amount and rate of change of mass of a material as a function of temperature or time under controlled atmospheric conditions[200]. TGA characterizes materials based on their thermal and compositional stability. In general, thermogravimetric analysis (TGA) instruments have a sample pan that is attached to a high precision analytical balance that is designed to sense changes in mass. A built-in furnace is programmed to provide a linear rise in temperature that generates heat directed radially towards the center. For any given nanofluid, the weight fraction of the dispersed phase can be estimated

from the weight loss curve. The nature of the surfactant coating around the nanoparticles can also be determined using TGA. The measurements included here were performed using Mettler-Toledo TGA-DSC-1, 1100 LF (Switzerland). Measurements were performed in the temperature range 30-600 ^{0}C under inert Argon atmosphere at a heating rate of 10 ^{0}C/minute.

2.9 Contact angle measurements

A contact angle meter (Holmarc, Kochi) with a built-in charge coupled device (CCD) was used for contact angle measurements. A single drop of ferrofluid of volume 10 µl was drop cast onto the substrate using a manual dispensing syringe pump which is mounted on a vertical translator to facilitate the adjustment of distance between the substrate surface and needle tip. The imaging optical assembly is also mounted on a translation stage for fine adjustment of the droplet image. The light source is a LED device, the intensity of which is manually controllable. Magnetic field was generated using a solenoid. The direction of the applied field was perpendicular to the substrate surface. Contact angle values were obtained using Imagej software (drop snake method).

2.10 Material characterization of ferrofluids

Five different ferrofluids (oleic acid coated magnetite nanoparticles dispersed in kerosene) of volume fraction 0.037 (corresponding to a weight percentage of 20 %) were used for experiments. The ferrofluid samples were coded as S1, S2, S3, S4 and S5. The sample code and characterization details of all five systems are summarized in table 2.1.

Table 2.1: Sample code and characterization details.

Sample code	Avg. Crystallite size [nm]	Most probable hydrodynamic size [nm]	Polydispersity index	Saturation magnetization [emu/g]	Surfactant weight loss [%]
S1	6.9 ± 0.7	11.6 ± 0.6	0.225	63 ± 0.6	30
S2	8.3 ± 0.8	18.2 ± 0.9	0.243	66 ± 0.7	21
S3	10.5 ± 1	21 ± 1	0.79	71 ± 0.7	19
S4	7.2 ± 0.7	11.7 ± 0.6	0.238	69 ± 0.7	24
S5	8.4 ± 0.8	24.3 ± 1.2		72 ± 0.7	

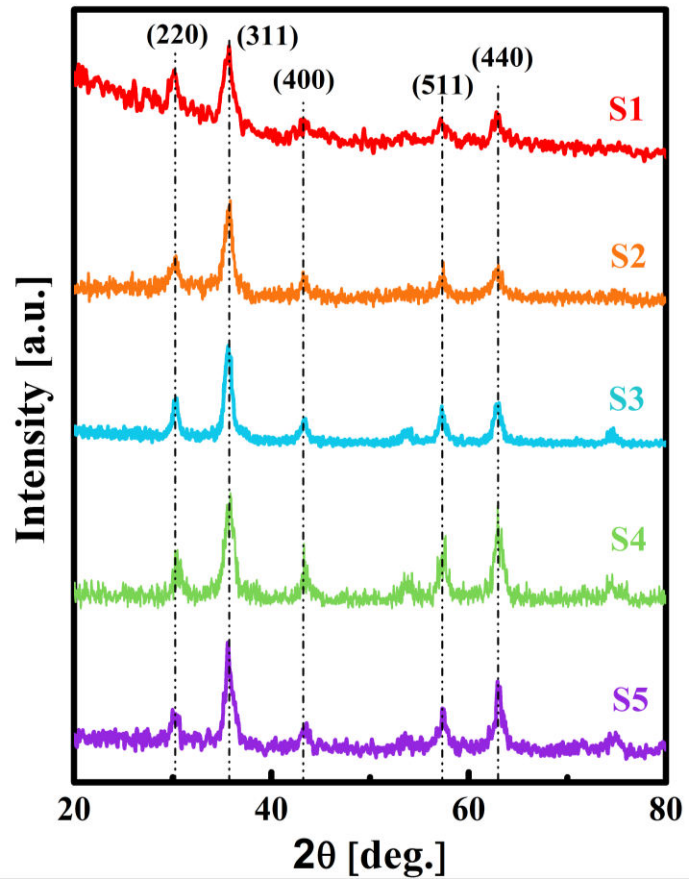

Figure 2.8: X-ray diffraction pattern of S1, S2, S3, S4 and S5.

The X-ray diffraction patterns of all five ferrofluid samples are shown in **Fig. 2.8**. The prominent peaks observed in the patterns were from (220), (311), (400), (511) and (440) planes corresponding to an inverse spinel structure (JCPDS card no. 89-3854) where the oxygen ions are arranged in a close packed cubic lattice with half of Fe^{3+} ions occupying tetrahedral interstices and the other half along with Fe^{2+} occupying octahedral interstices. The highest intensity peak is (311) from which the average crystallite sizes of S1, S2, S3, S4 and S5 were calculated using the Scherrer equation and the corresponding values are 6.9 ± 0.7, 8.3 ± 0.8, 10.5 ± 1, 7.2 ± 0.7 and 8.4 ± 0.8 nm, respectively.

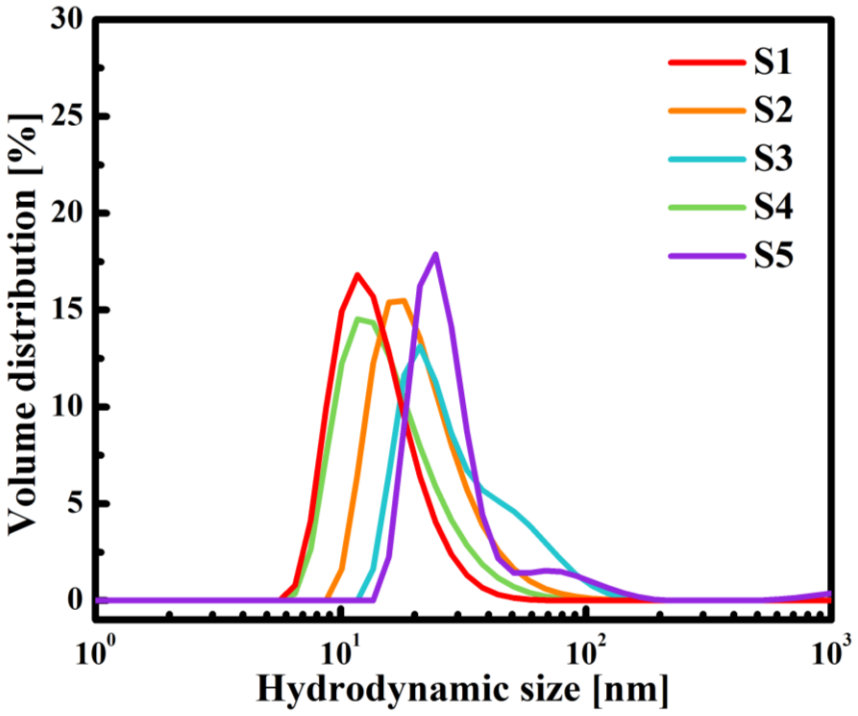

Figure 2.9: Volume distribution of hydrodynamic size of S1, S2, S3, S4 and S5.

The volume distribution of particles in all five ferrofluid systems obtained from dynamic light scattering studies is shown in **Fig. 2.9**. The most probable hydrodynamic size of S1, S2, S3, S4 and S5 are 11.6 ± 0.6, 18.2 ± 0.9, 21 ± 1, 11.7 ± 0.6 and 24.3 ± 1.2 nm, respectively. From the

volume distribution, S1 and S4 are relatively monodisperse while S3 and S5 is highly polydisperse with multiple peaks. The polydispersity index of S1, S2, S3 and S4 are 0.225, 0.243, 0.79 and 0.238, respectively.

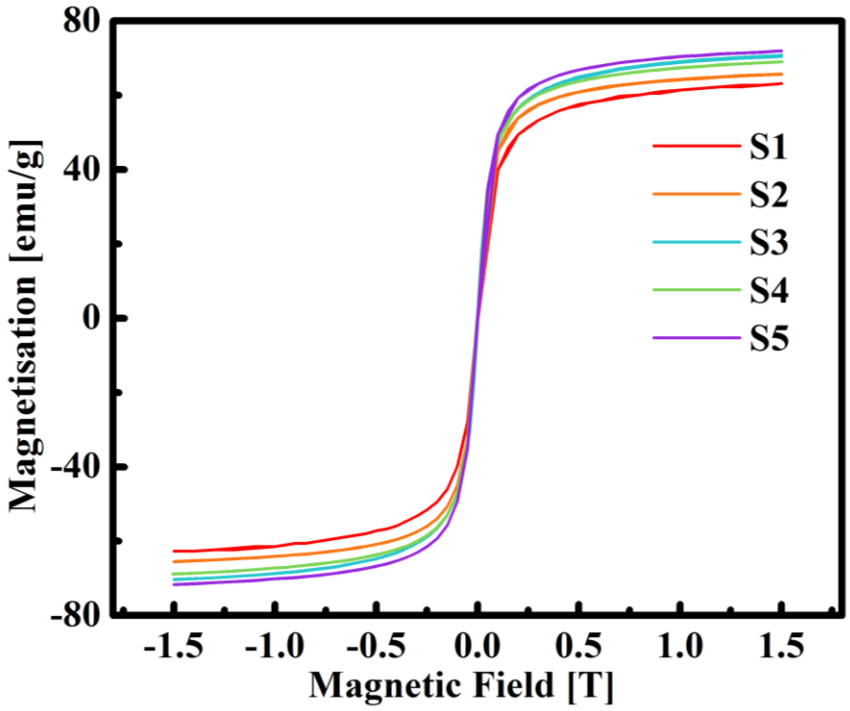

Figure 2.10: Magnetization curves of S1, S2, S3, S4 and S5.

The magnetization curves of S1, S2, S3, S4 and S5 are shown in **Fig. 2.10** and all the samples displayed superparamagnetic features with saturation magnetization values of 63 ± 0.6, 66 ± 0.7, 71 ± 0.7, 69 ± 0.7 and 72 ± 0.7 emu/g, respectively. Though the saturation magnetization values of all five systems are relatively similar, the effect of larger particles in polydisperse systems like S3 and S5 will manifest in the magnetization curves at low magnetic field strengths. As the moments of larger particles are easily oriented along the external magnetic field direction at relatively lower field strengths than smaller particles, magnetization will shower a steeper increase with increasing field strength at low field magnitudes for ferrofluids

with notable fraction of larger particles resulting in higher values of initial magnetic susceptibility in such systems[81]. Hence, for field strengths much below saturation magnetization, the particle size distribution affects the magnetic properties of ferrofluids drastically.

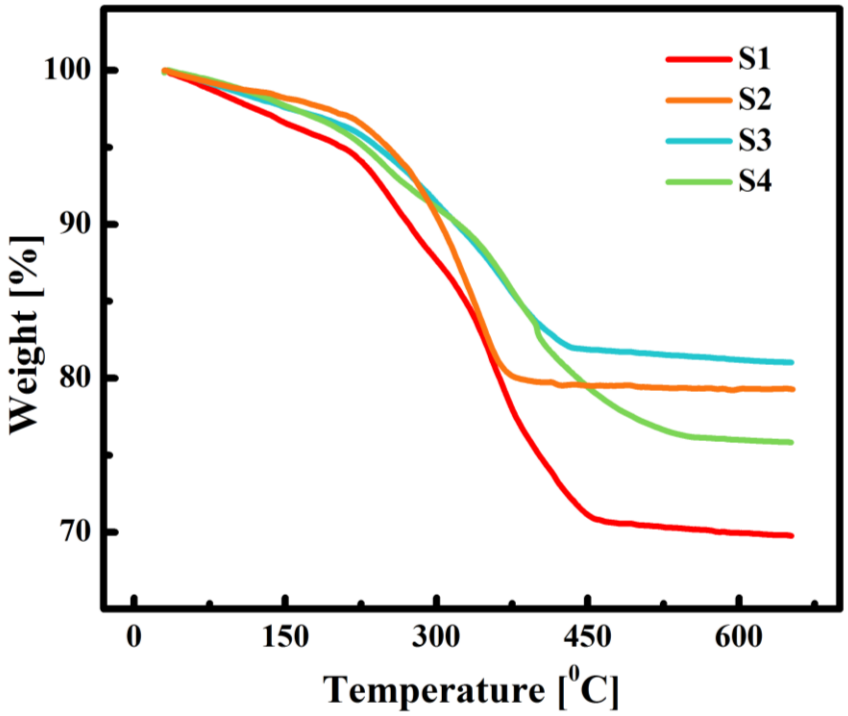

Figure 2.11: Thermogravimetric weight loss curves of S1, S2, S3 and S4.

Thermogravimetric weight loss curves of oleic acid coated magnetite nanoparticles of S1, S2, S3 and S4 are shown in **Fig. 2.11** and the corresponding weight loss was found to be 30, 21, 19 and 24 %, respectively. In S1 and S4 the average crystallite size of the particles was lowest and hence the weight loss is higher in these two systems owing to the presence of larger amount of surfactant. The weight loss percentage of adsorbed surfactant can be calculated using the

equation $\frac{100\left(\left(\frac{\pi d_{crystallite}^2}{a_s}\right)\frac{M}{N_0}\right)}{\left(\frac{1}{6}\pi d_{crystallite}^3\rho+\left(\frac{\pi d_{crystallite}^2}{a_s}\right)\frac{M}{N_0}\right)}$ where a_s is the head area of a single surfactant (oleic acid) molecule, N_0 is the Avogadro number, ρ is the density of magnetite nanoparticles and M is the molecular weight of oleic acid[201]. The calculated weight loss % were 25, 21.4, 17.7 and 23.9 %, respectively, for S1, S2, S3 and S4. On comparison with the experimentally obtained values, S1 has excess surfactant while the other samples have more or less comparable weight loss percentages. Insufficient amount of surfactant added can lead to permanent sticking of particles resulting in the formation of large aggregates which can result in higher polydispersity.

Chapter 3 Role of field induced aggregates on effective thermal transport in ferrofluids

3.1 Introduction

Ferrofluids exhibit magnetic field tunable thermal conductivity (k) making them desirable for cooling applications[136]. Even though tunable thermal conductivity in ferrofluids was conclusively proven by many researchers over the years, the exact mechanism or mechanisms for heat transport, the ideal conditions to achieve maximum enhancement in thermal conductivity and the reasons for different percentage of k enhancement obtained in ferrofluids containing similar volume fraction of magnetic nanoparticles are not clearly understood. A thorough understanding of the field tunable enhancement in k is a prerequisite to optimize the heat transfer properties of ferrofluids for the development of next generation microelectronic cooling technologies.

In this work, through systematic thermal, rheological and microscopic studies, the conditions to achieve very high thermal conductivity to viscosity ratio are explored. The questions that are addressed in this work are the following: (a) What is the role of magnetic field induced aggregates on thermal and rheological properties of ferrofluids? (b) What is the effect of capping agent on interfacial thermal conductance and heat transport? (c) How does the presence of larger particles or aggregates affect thermal conductivity and viscosity enhancement of ferrofluids in the presence of magnetic field? (d) What is the cause for decrease in thermal conductivity beyond a critical magnetic field? To address these questions, thermal and rheological properties of three ferrofluids of similar crystallite size, same capping agent and similar magnetic properties, but with different size distribution were studied. To understand field induced aggregation and its impact on thermal and rheological properties, phase contrast

microscopy studies were carried out. The possible role of surfactant and the effect of confinement of base fluid molecules by the field induced aggregates on interfacial thermal boundary conductance are also addressed.

3.2 Materials and methods

Oleic acid coated magnetite nanoparticles were prepared by chemical co-precipitation technique which is detailed in section 2.1 of chapter 2. Three different ferrofluids, S1, S2 and S3, were employed in this study. The volume fraction of all three ferrofluids was fixed at 0.037 (corresponding to 20 wt.%). **Table 3.1** summarizes the obtained results of ferrofluid characterization, details of which can be found in section 2.10 of chapter 2.

Table 3.1: Sample code and characterization details

Sample code	Avg. Crystallite size [nm]	Most probable hydrodynamic size [nm]	Polydispersity index	Saturation magnetization [emu/g]	Surfactant weight loss [%]
S1	6.9 ± 0.7	11.6 ± 0.6	0.225	63 ± 0.6	30
S2	8.3 ± 0.8	18.2 ± 0.9	0.243	66 ± 0.7	21
S3	10.5 ± 1	21 ± 1	0.79	71 ± 0.7	19

The thermal conductivity and rheological measurements were performed as described in chapter 2.

3.3 Results and discussion

3.3.1 Magnetic field induced enhancement in thermal conductivity (k)

3.3.1.1 Variation of k when magnetic field direction is parallel to the direction of heat flux

The variation of thermal conductivity of the ferrofluids relative to base fluid thermal conductivity, k/k_f as a function of applied field strength is shown in **Fig. 3.1**. In the absence of magnetic field, k/k_f of S1, S2 and S3 are nearly the same. The slight variations in k/k_f values are due to local density fluctuations in the fluids. In the presence of external magnetic field, S1 and S2 displayed significant enhancement in thermal conductivity upto a critical magnetic field. When the strength of magnetic field was increased beyond the critical value, k/k_f of S1 and S2 decreased. Maximum enhancement of 130 % was obtained for field strength of 150 G in S1 and in S2 the maximum enhancement obtained was 73 % at 80 G. S3 did not display notable enhancement in k with increasing field strength.

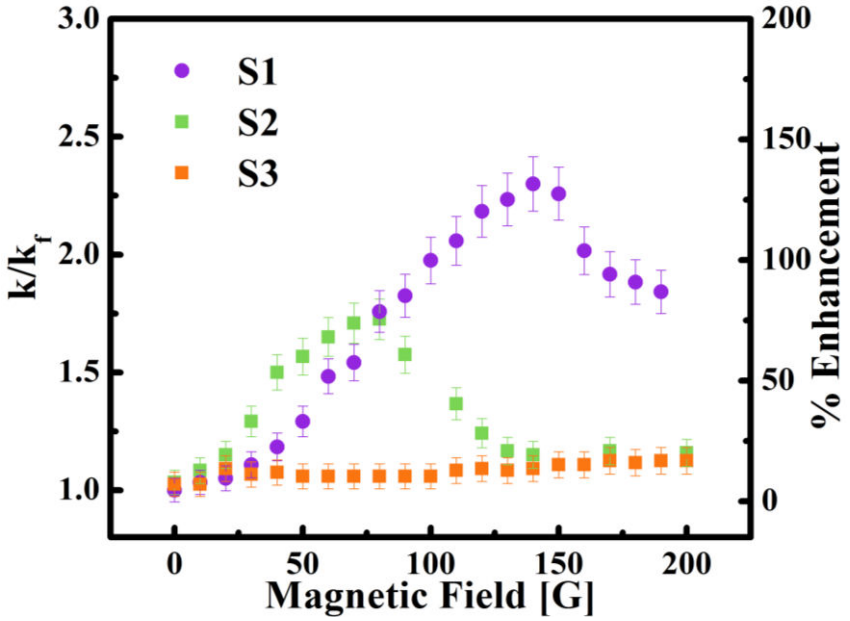

Figure 3.1: The variation of k/k_f and percentage of enhancement in k as a function of magnetic field strength when the field is applied parallel to the direction of heat flux.

The increase in k with increasing magnetic field strength is due to the increasing aspect ratio of the aggregates, which indicates that k depends on field induced microstructure. Phase contrast microscopy was employed to understand the reasons why the three ferrofluid systems, in spite of having same volume fraction and similar average crystallite size, have drastically different thermal properties in the presence of magnetic field. The microscopy images taken for different field strengths are shown in **Fig. 3.2**.

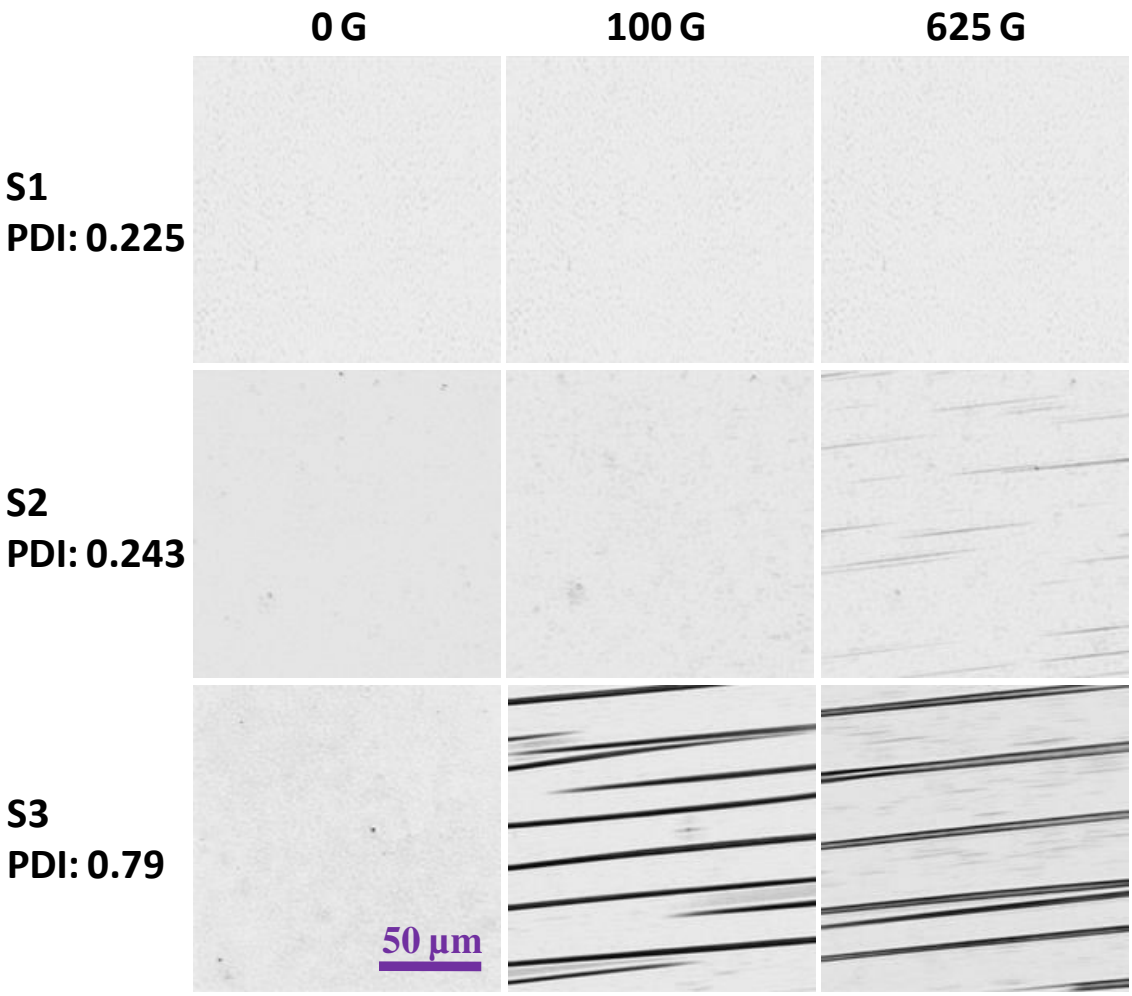

Figure 3.2: Phase contrast microscopy images of S1, S2 and S3 at different magnetic field strengths. The images clearly indicate the difference in aggregation kinetics of the ferrofluids.

Even for field strength of 625 G, observable aggregates were absent in S1, which indicates that the aggregates are nanosized. As the smallest size discernable using the phase contrast microscope is around 200 nm, the aggregate width must be less than 200 nm in S1. Microscopy images of S2 showed very small aggregates at 100 G which grew in length and breadth with increasing magnetic field. The number density of observable aggregates in S2 is rather low which indicates that most of the aggregates are nanosized. In S3 even for 100 G very long and thick aggregates were observed. On increasing field strength to 625 G, the aggregates

underwent further lateral coalescence and became bulkier. In addition to large aggregates, shorter and finer chains were also observed.

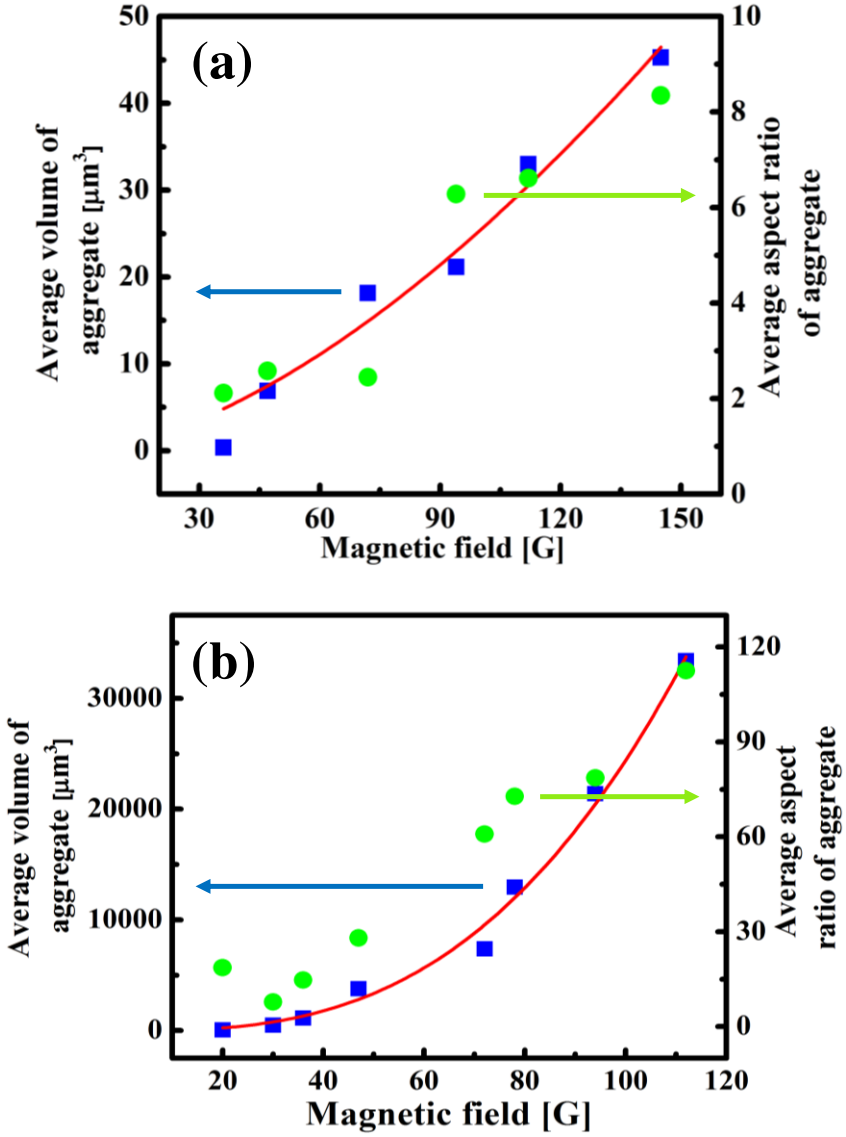

Figure 3.3: Variation of average volume and aspect ratio of field induced aggregates in (a) S2 and (b) S3 as a function of magnetic field strength. The average volume scales with the strength of the magnetic field as a power law with an exponent 1.6 ± 0.2 in S2 and 2.9 ± 0.3 in S3.

Using phase contrast microscopy images and considering the shape of the field induced aggregates to be elliptical, the change in volume of aggregate, $V_{aggregate} = \frac{4}{3}\pi a' b'^2$ where a' is the semi-major axis, b' is the semi-minor axis, as a function of strength of applied field was obtained and the results are plotted in **Fig. 3.3**. The change in aspect ratio (ratio of length to breadth) of aggregates with field strength is also indicated in **Fig. 3.3**. With increase in field strength, the increase in volume and aspect ratio of field induced aggregates in S3 is far greater than S2. The average volume of aggregates scales with the strength of applied field as a power law with an exponent of 1.6 ± 0.2 in S2 and 2.9 ± 0.2 in S3.

In S1 with the least polydispersity, observable aggregates were absent due to hindering of zippering transitions. Presence of significant amount of smaller particles can hinder growth of aggregates with increasing field strength due to sticking of the smaller particles at chain ends resulting in reduced dipole interaction (poisoning effect)[85, 202]. The smallest particles may not interact even at high field strengths owing to low dipole-dipole interaction. As a result, the field induced aggregates in S1 remained nanosized even at 625 G. S2, with slightly higher polydispersity index and greater fraction of large particles than S1, had observable field induced aggregates, though most of the aggregates were still nanosized even at 625 G. The larger dipole interaction of bigger particles in S2 is responsible for the formation of few observable aggregates. From the volume distribution it is clear that S3 has significant amount of larger particles which act as nucleation centers and initiate chain formation even at low field strengths[203, 204]. With further increase in magnetic field strength, the aggregates grow in length and undergo zippering transitions becoming longer and thicker. However, extensive zippering transitions reduce the number density of aggregates drastically.

From the experimental results, ferrofluids with less polydispersity and less amount of larger particles where extensive zippering transitions are hindered is found to be ideal for obtaining high enhancement in field tunable thermal conductivity. Though several studies on field tunable thermal transport of ferrofluids are available, detailed insight into the factors affecting heat transport within a chain or aggregate and the reasons behind why certain ferrofluids did not show enhancement in thermal conductivity in the presence of magnetic field are rarely addressed. Despite high thermal conductivity of materials like graphene (1500-2500 $Wm^{-1}K^{-1}$) and carbon nanotubes (around 3500 $Wm^{-1}K^{-1}$ along its axis), when these materials are dispersed in a liquid medium, the effective thermal conductivity of the nanofluid is significantly lower than that of the nanoparticles[205, 206]. The reason for this decrease is scattering of phonons at the particle/fluid interface. In a ferrofluid, even a single field induced aggregate will have many such interfaces. Thermal conductance across an interface separating two dissimilar materials is commonly known as Kapitza conductance G_k which is defined as[207]

$$J_Q = -G_k \Delta T \tag{3.1}$$

where J_Q is the heat flux across the interface and the sharp temperature drop across the interface is given by ΔT. In the case of nanofluids, the effective thermal conductivity of the system depends heavily on the effectiveness of heat transfer from the solute to the solvent. Kenkre et al.[208] described vibrational relaxation of polyatomic molecules dispersed in polyatomic solvents using quantum mechanics. Liquids, unlike solids that possess well defined bound phonon modes, possess a continuum of low frequency vibrational modes, popularly called instantaneous modes, owing to their continuously changing structure. These instantaneous normal modes are also referred to as ‘phonons’ in literature though they are different from crystal phonons. In a colloid, excited vibrational mode of the solute relaxes by coupling with a

combination of low frequency modes of the solvent which mostly involves production of solvent phonons to conserve energy. The vibrational relaxation rate is governed by Fermi's golden rule given by

$$R_{vib} = \frac{2\pi}{\hbar}\sum_{r',r"}\rho_{r',r"}\left|\left\langle\sigma"',r"\middle|V'_p\middle|\sigma',r'\right\rangle\right|^2 \quad (3.2)$$

where the density of states is given by $\rho_{r',r"}$, r' and $r"$ represent the initial and final states of the modes to which the excited mode transferred energy, σ' and $\sigma"'$ represent the initial and final states of the excited vibrational mode and V'_p is the potential. Transient absorption measurements performed by Huxtable et al.[209] to study interfacial thermal transport in carbon nanotube suspensions revealed that efficient heat transport from the nanotubes to the base fluid occurred only when the high frequency modes of the nanotubes coupled with lower frequency modes within itself which then coupled with the lower frequency modes of the base fluid as nanotubes and base fluid are coupled strongly only through limited number of low frequency vibrational modes. The authors reported that the limiting factor for heat transfer was this cascade of energy. The effect of chemical bonding on interfacial thermal transport was studied by Losego et al[210]. They monitored the variation of heat flow across a gold-self assembled monolayer (SAM) interface as a function of chemical bonding across the interface by changing the end group chemistries across gold-SAM interface. The authors found that SAM having thiol end group displayed higher thermal boundary conductance than one with methyl group and this difference was attributed to the nature of bonding between the different end groups with the gold surface. Thiols interact with gold surface through covalent bonds while methyl groups interact via weak van der Waal's interaction. Non-equilibrium molecular dynamics simulations of carbon nanotubes in poly(ether ketone) revealed that thermal boundary conductance was higher for

functionalized nanotubes than bare particles and as the number of covalent bonds increased, thermal boundary conductance also increased[205]. Studies on thermal boundary conductance on fullerene derivative solutions using time domain thermo-transmittance technique also confirmed that functionalization impacts thermal transport across the boundary between nanoparticles and base fluid[206]. Hence, stronger the bonding between nanoparticles and surfactant, better is the thermal boundary conductance. When compared to bare fullerene, the low frequency density of states of fullerene derivatives was found to overlap more with the low frequency density of states of the base fluid resulting in better coupling of frequency modes of solute and solvent. Molecular dynamics simulations of fullerene in octane revealed that only the low frequency modes of fullerene will be capable of coupling with the abundant number of low frequency modes of octane. In S1, S2 and S3 the magnetite nanoparticles are functionalized with oleic acid that is covalently attached to the nanoparticle surface which can aid in coupling of vibrational modes of solute with that of the solvent. However, the reason behind the absence of significant k enhancement in S3 is still unexplained.

To explain heat transport from one end of a field induced aggregate to another in a ferrofluid, one must additionally consider the impact of liquid layering around each particle. As the magnetite particles are functionalized, even in the presence of magnetic field, the particles cannot come into direct contact with each other. Hence, they confine solvent molecules between them when they aggregate in the presence of external magnetic field. Oleic acid, being hydrophobic, interacts strongly with kerosene. In **Fig. 3.4**, when a magnet is held at the side of a bottle containing ferrofluid, it is not only the solid particles that are held by the magnet, but also the base fluid, which confirms that the base fluid is held closely by the field induced aggregates within themselves as well as between them.

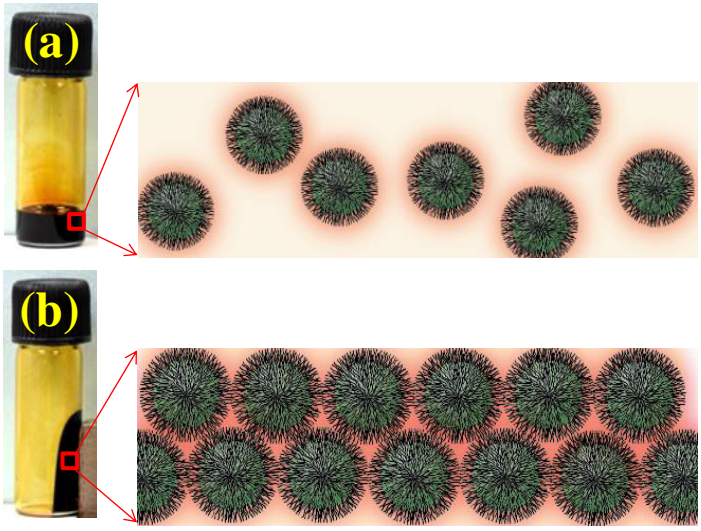

Figure 3.4: Photograph of glass vial containing ferrofluid in the (a) absence and (b) presence of magnetic field. Schematic of (a) the particles in Brownian motion in the absence of magnetic field and (b) field induced aggregates aligned along the field direction is shown on the right side.

Liquid layering around nanoparticles was not considered as a dominant mechanism for improved heat transport displayed by nanofluids as experiments indicated that the layer of ordered liquid around a nanoparticle extended only upto a few atomic distances[211]. However, subsequent studies revealed that liquid layering can play an important role in heat transport by reducing interfacial phonon scattering. Molecular dynamics study of water-SAM interfaces where the wetting properties were varied by using different end group chemistries revealed that stronger bonding or better wetting increased thermal boundary conductance because high frequency phonons are transmitted better with increased bond strength or increased wetting[212, 213]. Caplan et al.[214] reported that for strongly wetted particles, as the translational motion of liquid molecules at the interface is severely restricted, the transverse vibrational modes of the solid could couple strongly to the liquid in addition to the longitudinal modes. Recent studies on heat transport across solid Argon-liquid Argon interface also demonstrated the importance of

interfacial bonding on thermal boundary conductance[215]. Frank et al.[216] reported that when liquids are confined to nanochannels, owing to structural order of liquid molecules brought about by confinement, long range phonons could also be sustained thereby improving thermal transport. Enhanced heat transport through liquid confinement could be the reason why S1, with large number density of field induced aggregates owing to hampered zippering transitions, displayed excellent heat transport efficiency while S3, where most of the aggregates are micron sized, did not. This could also explain the decrease in k beyond a critical field in S1 and S2 since beyond the critical magnetic field, zippering transitions occur reducing the number density of aggregates. As magnetic field of low magnitudes is sufficient to achieve huge enhancement in thermal transport, ferrofluids are attractive candidates for use as coolants.

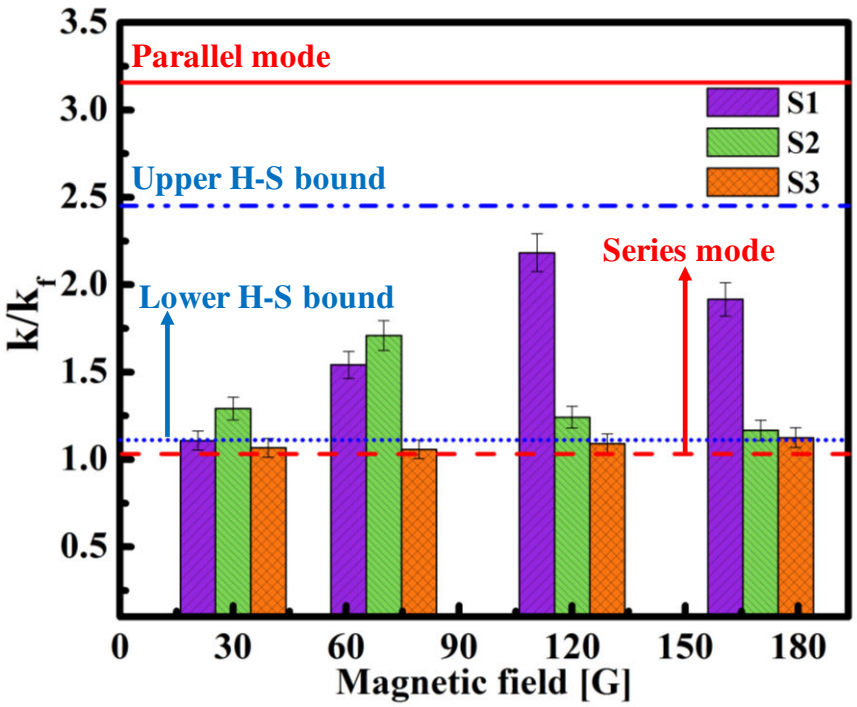

Figure 3.5: Variation of k/k_f with field strength in S1, S2 and S3 along with the predicted value of k/k_f for $\Phi = 0.037$ using series and parallel models (dashed and solid red lines, respectively) and lower and upper H-S bounds (dotted and dashed blue lines, respectively).

Thermal conductivity as a function of volume fraction was described by mean field models for parallel and series mode of thermal conduction where the pathway for heat conduction through the base fluid and the suspended nanoparticles is assumed to be parallel in the former and series in the latter[134, 217]. In the series mode of conduction, the effective thermal conductivity is given by

$$\frac{1}{k^{=}} = \frac{(1-\Phi)}{k_f} + \frac{\Phi}{k_p} \tag{3.3}$$

and in the parallel mode of conduction the effective thermal conductivity is given by

$$k^{\parallel} = (1-\Phi)k_f + \Phi k_p \tag{3.4}$$

where k_p and k_f are the thermal conductivity of particle and base fluid, respectively. If $k_p \gg k_f$ (which is generally true) then $k^{\parallel} > k^{=}$. As the parallel mode represents a geometric configuration that is most favorable for heat transport, it is generally considered as the upper limit for effective thermal conductivity of a nanofluid. More restrictive bounds were developed by Hashin and Shtrikman using variational principles where the lower bound corresponds to a configuration where the nanoparticles are dispersed uniformly throughout the solvent and the upper bound corresponds to a configuration where the nanoparticles aggregate and form percolating paths through which heat is transported[218]. The Hashin-Shtrikman (H-S) bounds is given by

$$k_f\left[1 + \frac{3\Phi(k_p-k_f)}{3k_f+(1+\Phi)(k_p-k_f)}\right] \leq k \leq k_p\left[1 - \frac{3(1-\Phi)(k_p-k_f)}{3k_p-\Phi(k_p-k_f)}\right]. \tag{3.5}$$

As the volume fraction of ferrofluids used was 0.037, the effective thermal conductivity was calculated for $\Phi = 0.037$ using the parallel and series bounds (solid and dashed red lines,

respectively, in **Fig. 3.5**) as well as upper and lower H-S bounds (dashed and dotted blue lines, respectively, in **Fig. 3.5**). The variation of k with magnetic field strength is compared to the values calculated using the mean field models in **Fig. 3.5**. For low field strengths, the effective thermal conductivity is close to the value calculated using series mode. Interestingly, for magnetic field strengths less than 80 G, enhancement in k is higher in S2 than S1. S2 has higher fraction of larger particles than S1 and hence tip-to-tip aggregation, responsible for increase in length of single chains, occurs at a faster rate in S2 than S1 owing to increased dipolar interactions. Longer chains give larger increase in k. The presence of larger particles in S2 also reduces the potential barrier for zippering transitions which occur at much lower field strength than S1 and hence k reduces after 70 G to nearly the value predicted by the lower H-S bound. In S1 where the presence of notable fraction of smaller particles hinder zippering transitions, decrease in k occurs at a critical field which is much higher than that of S2 and the decrease in k is not as steep as in S2. However, even the highest k exhibited by S1 is lower than the k predicted by upper H-S bound and parallel mode of conduction. In S3, even with increasing magnetic field strength, effective k remains close to the value predicted by the series model.

3.3.1.2 Variation of k when magnetic field direction is perpendicular to the direction of heat flux

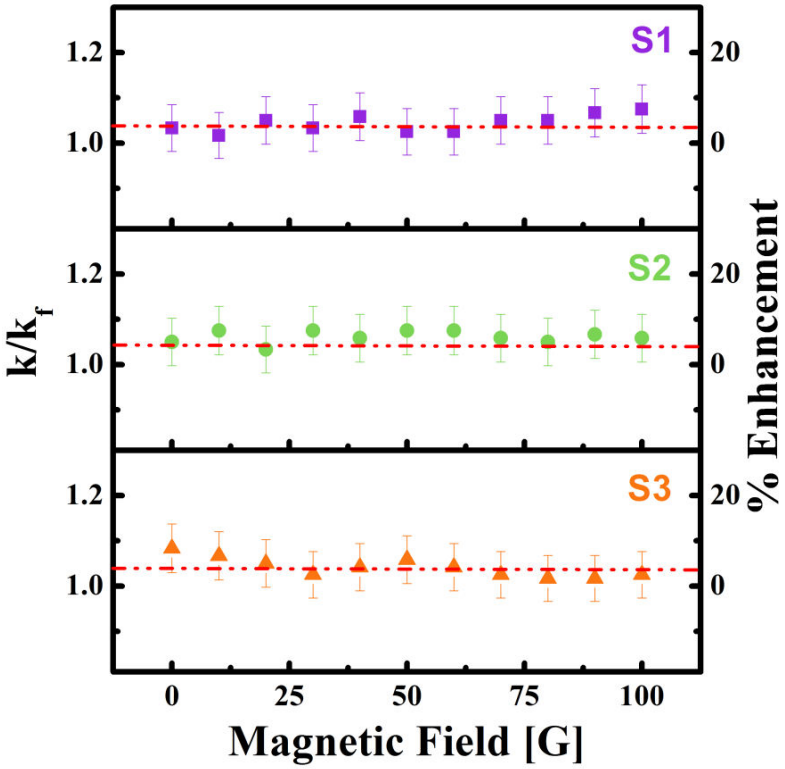

Figure 3.6: Variation of k/k_f in S1, S2 and S3 as a function of magnetic field strength when the field is applied perpendicular to the direction of heat flux. The value of k predicted by the series model for $\Phi = 0.037$ is indicated by the red dashed line.

Significant enhancement in thermal conductivity (<10 %) was not observed in S1, S2 and S3 when the direction of external magnetic field was perpendicular to the direction of heat flux as shown in **Fig. 3.6**. The value of k of all three systems is comparable to the value obtained from the series model for heat conduction (red dashed lines in Fig.) for $\Phi = 0.037$. Hence, in addition to magnitude, the direction of applied magnetic field also affects field tunable thermal transport.

3.3.2 Magnetic field induced enhancement in rheological parameters

3.3.2.1 Magnetic field induced enhancement in viscosity

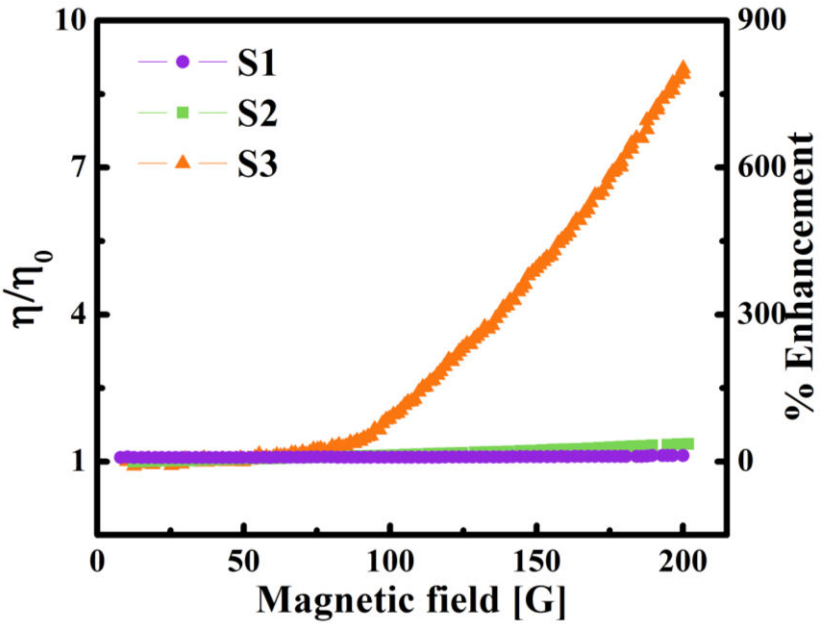

Figure 3.7: Variation of η/η_0 in S1, S2 and S3 as a function of magnetic field strength with the percentage of enhancement indicated on the right axis.

The enhancement in viscosity with respect to the viscosity obtained in the absence of magnetic field (η_0) as a function of strength of applied magnetic field is shown in **Fig. 3.7.** The viscosity curves were obtained at a constant shear rate of 75 s^{-1}. Even for field strength as low as 200 G, around 800 % enhancement in viscosity was obtained in S3 while S1 and S2 displayed only minimal enhancement. The root cause for enhancement of viscosity in ferrofluids when magnetic field is applied perpendicular to the shear field, is the formation of field induced aggregates that span the gap between the rheometer plates[101]. At a constant shear rate when the strength of the applied field is increased, viscosity increases when the magnetic force dominates over the hydrodynamic force[109]. Microscopy images confirm the formation of thick

aggregates in S3. The thick field induced aggregates in S3 resist shear which manifests as increased viscosity. S1 and S2 possess large fraction of smaller particles that hinder extensive zippering transitions as a result of which most of the aggregates are nanosized and can be broken apart easily by the applied shear. Hence, S1 and S2 showed only minimal enhancement in viscosity with increasing field strength.

3.3.2.2 Magnetic field induced changes in viscoelasticity

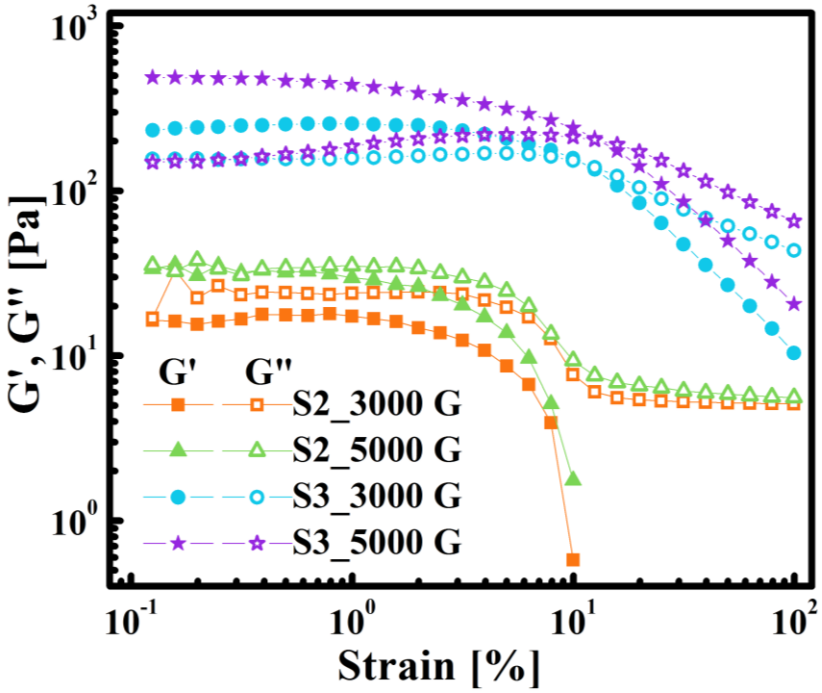

Figure 3.8: Variation of G' and G" of S2 and S3 as a function of strain amplitude at field strengths of 3000 and 5000 G.

The viscoelastic nature of the field induced aggregates of S2 and S3 was investigated using amplitude sweep at constant frequency of 10 rad.s^{-1}. As the field induced aggregates in S1 were too weak, reliable data could not be obtained owing to low torque values. In S2 measurements had to be performed at high magnetic field strengths to obtain reliable data (3000

to 5000 G) and even then S2 displayed a predominantly viscous behavior. For 3000 G, G" > G' in S2 throughout the amplitude sweep, as shown in **Fig. 3.8**, probably because the aggregates are not gap spanning which results in easy alignment of aggregates along the direction of imposed strain[219]. At around 5 % strain, G" decreases from around 30 to 6 Pa which was accompanied by a sharp decline in G' due to dislodgement and disintegration of the feeble aggregates. For higher field strength of 5000 G, G' and G" of S2 are more or less the same below 0.6 % strain possibly due to the formation of weak gap spanning structures brought about by increased magnetic interaction. For 3000 and 5000 G, below a critical strain, G' > G" in S3 which is indicative of the strength of the gap spanning aggregates. For strain amplitude less than 0.3 %, G' and G" are independent of the imposed strain indicating that the aggregates formed are not affected by hydrodynamic forces and this region below the critical strain is termed as the linear viscoelastic (LVE) region. For strain amplitudes beyond the LVE region, nonlinearity in G' and G" sets in due to slight rearrangement of particles within the aggregates in an effort to regain stable configurations and G' starts decreasing[220]. For both field strengths, as the amplitude of imposed strain is further increased, the field induced aggregates are broken apart by hydrodynamic forces as a result of which G" > G' in S3. The cross over of G' and G" occurs around 10 % strain for 3000 G and around 13 % strain for 5000 G indicating that the aggregates are stronger at higher field strengths.

3.3.2.3 Magnetic field induced enhancement in yield stress

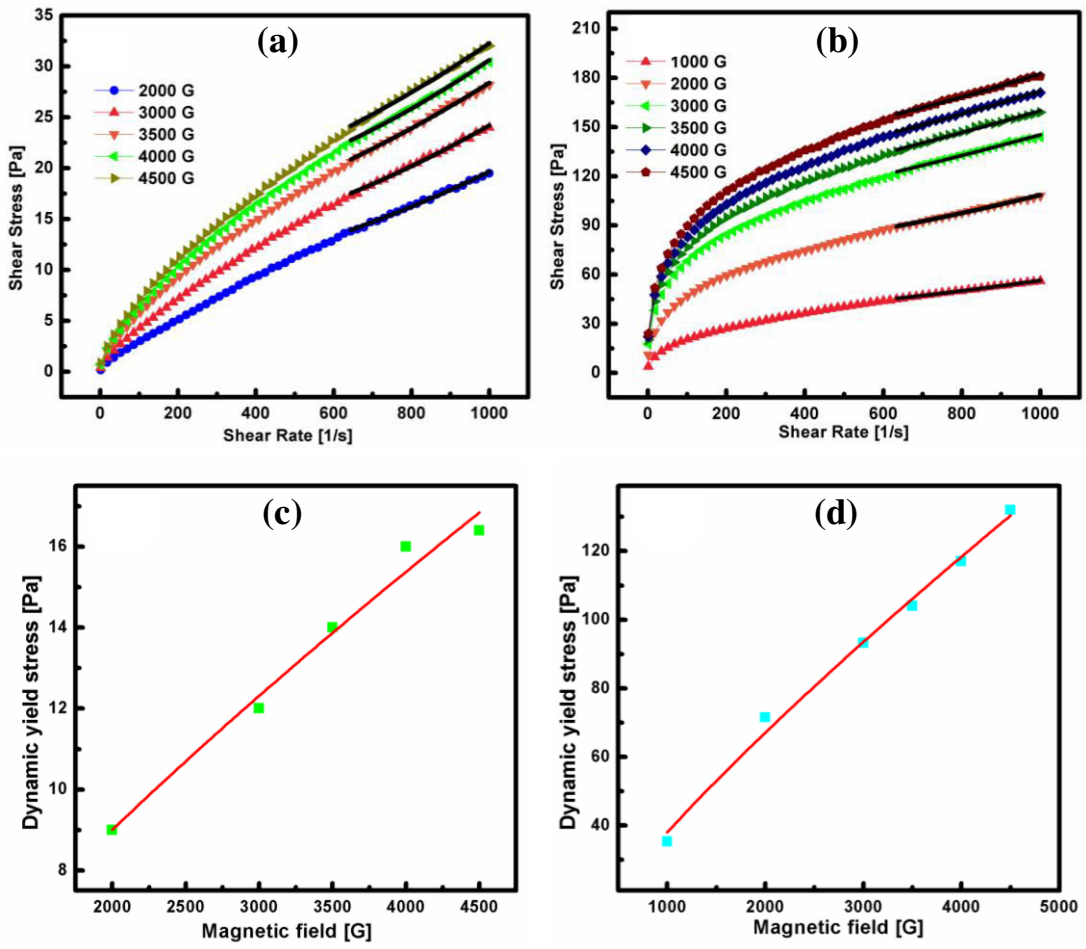

Figure 3.9: Flow curves of (a) S2 and (b) S3 obtained at different field strengths. Black line indicates the fit of data to Herschel-Bulkley model. The variation of yield stress of S2 and S3 with magnetic field strength is shown in (c) and (d), respectively. Yield stress scaled with magnetic field strength as a power law with exponent 0.77 ± 0.07 in S2 and 0.8 ± 0.04 in S3.

Magnetic field dependent dynamic yield stress is one of the most important rheological properties of ferrofluids. Since ferrofluids with significant amount of larger particles have thicker and longer field induced aggregates, the yield stress will be higher for such systems when compared to a relatively monodisperse ferrofluid. The variation of yield stress with magnetic

field strength is shown in Fig. 3.9 (c & d). The dynamic yield stress was obtained by fitting the flow curves (Fig. 3.9 (a & b) at higher shear rates (> 600 s^{-1}) to the Herschel-Bulkley model (eqn (1.26), section 1.5.1.2 in chapter 1). S3 displayed significantly higher yield stress in the presence of magnetic field than S2 as the field induced aggregates in S3 are stronger than those in S2. For example, when exposed to magnetic field of strength 4000 G the yield stress of S3 was around 117 Pa while the yield stress of S2 was around 16 Pa.

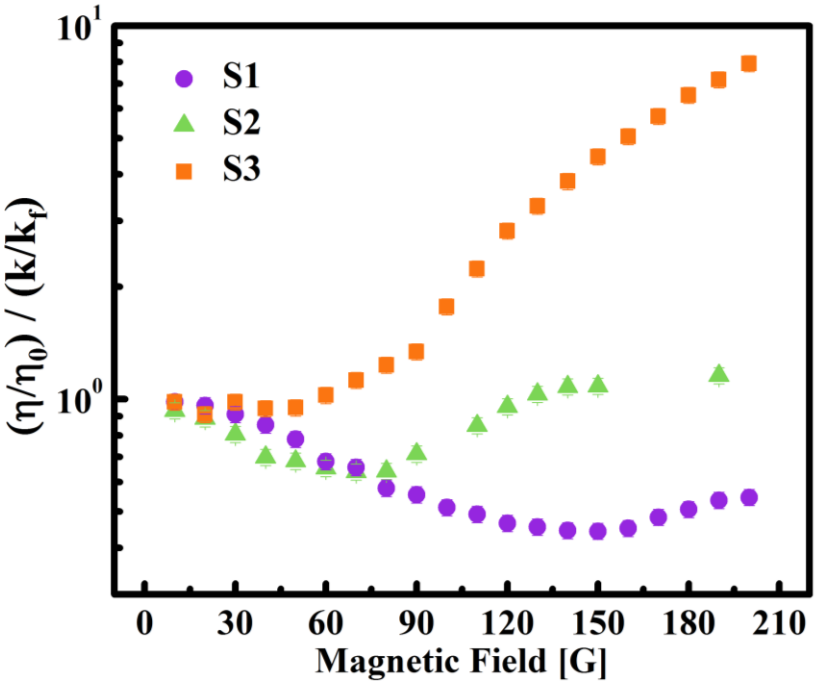

Figure 3.10: Variation of ratio of relative change in viscosity to the relative change in thermal conductivity as a function of magnetic field strength.

Prasher et al.[221], from studies on thermal conductivity and viscosity enhancements of alumina nanofluids subjected to laminar flow, concluded that the efficiency of a nanofluid as a coolant will be lower than the bare base fluid when the relative increase in viscosity ($\eta_r = \eta/\eta_o$) is around four times higher than the relative increase in thermal conductivity ($k_r = k/k_f$).

Shima et al.[135] demonstrated that in ferrofluids, η_r/k_r for a particular volume fraction can be tuned by varying the strength of the external magnetic field which is highly advantageous from a technological point of view. In S1 and S2 since the relative increase in thermal conductivity is much higher than the relative increase in viscosity, $\frac{\eta_r}{k_r} < 1$ upto 200 G (**Fig. 3.10**) which makes them highly suitable as coolants. In S3, which exhibited huge increase in viscosity without significant increase in k with field, $\frac{\eta_r}{k_r} > 4$ beyond 150 G.

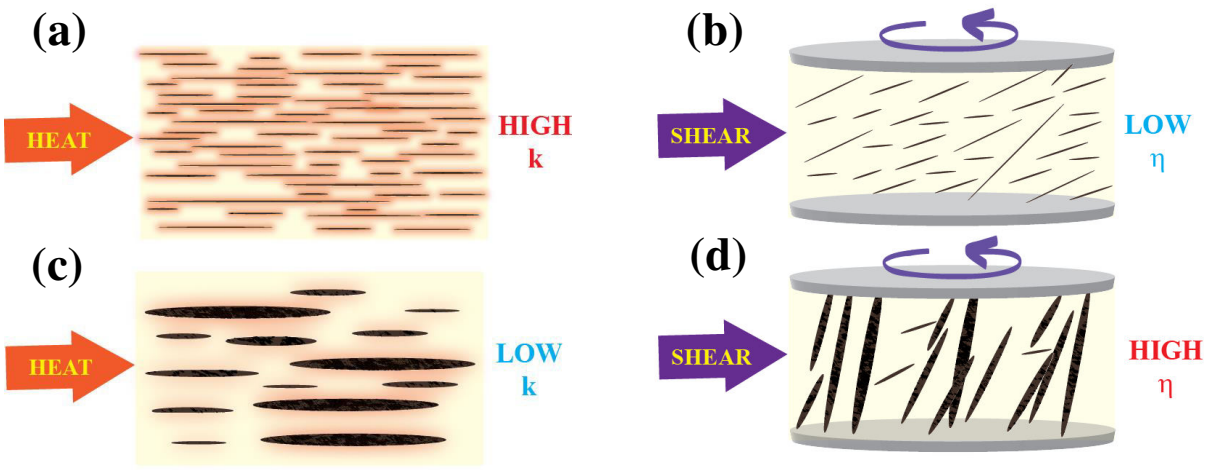

Figure 3.11: Schematic representing the field induced microstructure (a) favorable and detrimental (c) to k enhancement and the microstructure that is (b) detrimental and (d) favorable to viscosity enhancement.

From the above experimental results, it can be concluded that relatively monodisperse ferrofluids without large aggregates display high enhancement in k with magnetic field without significant increase in viscosity (see **Fig. 3.11 (a & b)**). Ferrofluid containing large aggregates on the other hand will display huge viscosity enhancement without notable enhancement in k (see **Fig. 3.11 (c & d)**).

3.4 Conclusions

Studies on thermal and rheological properties of three different ferrofluids containing oleic acid capped magnetite nanoparticles of similar crystallite size but different size distribution point towards the decisive role played by aggregation kinetics on the efficiency of a ferrofluid to conduct heat. When an external magnetic field was applied parallel to the direction of heat flux, S1, which was the least polydisperse with considerably less large particles than S2 and S3 gave maximum k enhancement of 130 % at 150 G while S2, with slightly higher polydispersity than S1, gave maximum enhancement of 73% at 80 G. S3, which was highly polydisperse with significant amount of larger particles did not display notable enhancement in k. Phase contrast microscopy images taken in the presence of magnetic field revealed that in S1 observable aggregates were absent even for field strength as high as 625 G while in S2 and S3 visible aggregates were present. At 625 G the visible aggregates in S3 were longer and coarser than those of S2. This difference in aggregation kinetics is brought about by differences in the particle size distribution of the three ferrofluids. In S1 observable aggregates were absent as the significant amount of small particles present in it hamper zippering transitions by sticking to the end of aggregates and preventing further growth due to the decreased dipolar interaction. As a result, most of the aggregates in S1 are still nanosized. In S2 with more large particles than S1, few micronsized aggregates were observed at 625 G, though most of the aggregates are still nanosized. In S3 which is highly polydisperse containing significant amount of large particles, aggregation kinetics is much faster than a relatively monodisperse system of same average size as the large particles themselves act as nucleation centers and initiate chain formation even at low field strengths. Extensive zippering transitions in S3 reduced the number density of aggregates leading to reduced interaction between the aggregates and base fluid, thereby

reducing interfacial boundary conductance leading to minimal enhancement in k with field. In S1, owing to hampered zippering transitions, the large number density of aggregates confines solvent molecules reducing the disorder of the base fluid which is beneficial for interfacial thermal transport. In S1 and S2, beyond a critical magnetic field, k decreases as zippering transitions becomes predominant over tip-to-tip aggregation. Less than 10 % enhancement in thermal conductivity was observed in S1, S2 and S3 when the direction of applied magnetic field was perpendicular to the direction of heat flux. For magnetic field strength as low as 200 G, S3 displayed around 800 % enhancement in viscosity owing to the formation of thick gap spanning aggregates that resist shear while S1 and S2 showed minimal enhancement in viscosity as most of the aggregates are nanosized and easily broken apart by shear. Owing to thick gap spanning aggregates, the yield stress of S3 was much higher than S2 and for small amplitudes of imposed strain (<0.3 %) S3 displayed dominant elastic nature while S2 displayed viscous nature. From the experimental results it can be concluded that ferrofluids containing narrow and smaller size distribution of particles, with proper surfactant bonding, can provide extraordinary field dependent thermal conductivity enhancement without significant viscosity rise. Hence, by tailoring the particle size distribution appropriately, efficient heat transfer can be achieved without increasing pumping power.

Chapter 4 Impact of magnetic field ramp rate on effective thermal transport in ferrofluids

4.1 Introduction

Magnetic field assisted thermal transport in ferrofluids has received much attention in recent years owing to their potential as a coolant, especially in miniature devices. Though various parameters affecting thermal transport in ferrofluids were studied, the role of aggregation kinetics on thermal conductivity is scarcely addressed. Thermal conductivity (k) of ferrofluids is highly sensitive to the field induced microstructure[151]. Many contradicting thermal conductivity enhancements were reported in similar nanofluids, owing the lack of model nanofluids with well defined physical properties like size, morphology, polydispersity and proper surfactant capping. Among the many factors that influence aggregation kinetics, magnetic field quench rate has received the least attention.

The extreme sensitivity of thermal conductivity to microstructure of nanofluids warrants a detailed study of aggregation kinetics. It has been reported that fast ramp rates result in the simultaneous formation of large number of aggregates which are out of equilibrium as the nanoparticles does not have enough time to settle into minimum energy configurations. On the other hand slow ramps result in the formation of field induced aggregates closer to equilibrium as a result of which yield stress was found to be higher for slower ramps[222, 223]. In this work, the effect of field ramp rate on thermal transport of oil based ferrofluid is explored. As aggregation kinetics depends heavily on particle size distribution, three different ferrofluid systems of same volume fraction but with different size distributions were employed and the effect of size distribution on thermal conductivity when magnetic field is applied at different ramp rates was probed.

4.2 Materials and methods

Oleic acid coated magnetite nanoparticles were prepared by chemical co-precipitation technique which is detailed in section 2.1 of chapter 2. Two different ferrofluids, S4 and S5, were employed in this study along with a third system S45 which was obtained by mixing S4 and S5 in the ratio 95:5. The volume fraction of all three ferrofluids was fixed at 0.037 (corresponding to 20 wt.%). **Table 4.1** summarizes the obtained results of ferrofluid characterization, details of which can be found in section 2.10 of chapter 2.

Table 4.1: Sample code and characterization details.

Sample code	Avg. Crystallite size [nm]	Most probable hydrodynamic size [nm]	Polydispersity index	Saturation magnetization [emu/g]
S4	7.2 ± 0.7	11.7 ± 0.6	0.238	69 ± 0.7
S5	8.4 ± 0.8	24.3 ± 1.2		72 ± 0.7

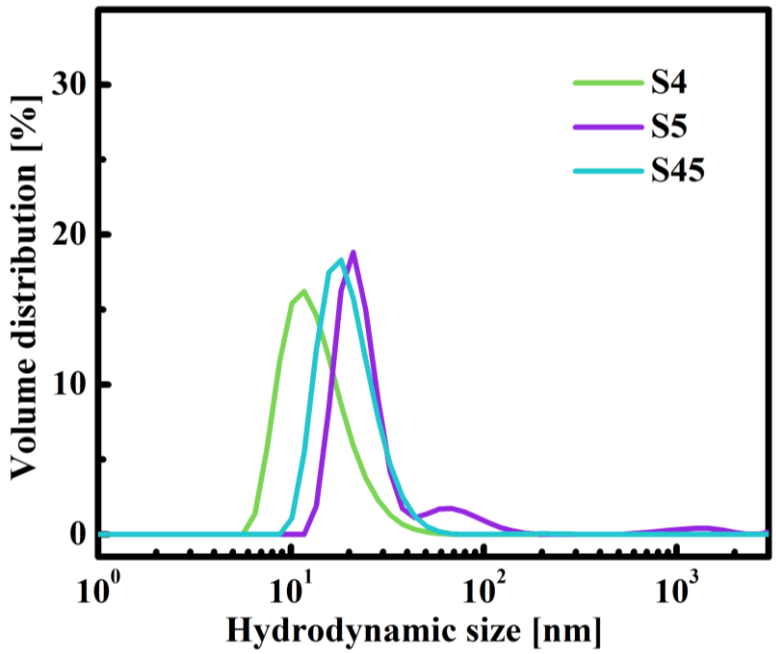

Figure 4.1: Volume distribution of hydrodynamic diameter of S4, S5 and S45.

Fig. 4.1 shows the volume distribution of hydrodynamic size of particles in S4, S5 and S45. From the distribution, the most probable hydrodynamic size for S4, S5 and S45 was found to be 11.7 ± 0.6, 24.3 ± 1.2 and 18.2 ± 0.9 nm, respectively. The volume distribution of S5 has multiple peaks and has significant amount of larger particles than S4 which has a monomodal distribution. S45 which is a combination of S4 and S5 is still monomodal, however the most probable size has shifted to a larger value than S4.

The thermal conductivity measurements were performed as described in chapter 2.

4.3 Results and discussion

4.3.1 Effect of magnetic field ramp rate on thermal transport

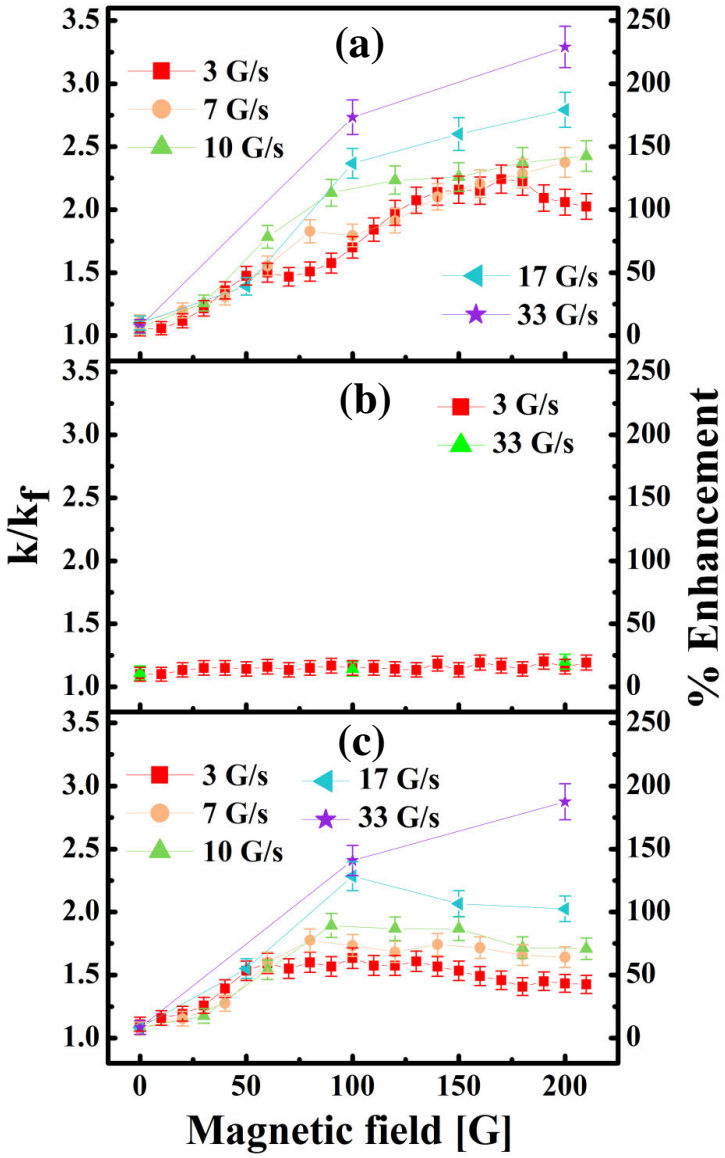

Figure 4.2: Variation of k/k_f with field in (a) S4, (b) S5 and (c) S45 for different ramp rates of applied field. The axis on the right indicates the % enhancement of thermal conductivity with respect to the base fluid conductivity.

The variation of thermal conductivity of S4, S5 and S45 expressed relative to that of the base fluid (k/k_f) as a function of magnetic field applied at different ramp rates are shown in **Fig. 4.2 (a), (b)** and **(c)**, respectively. Thermal conductivity of S4 and S45 improved substantially with increasing field strength and ramp rate of magnetic field. On the other hand, S5 did not display significant enhancement with field even for 33 G/s ramp. In S4, maximum enhancement of 124 % was obtained at 170 G for 3 G/s ramp and k showed a decreasing trend with further increase in field strength. For higher field ramps, k of S4 did not decrease for the applied range of magnetic field. For 17 G/s ramp, thermal conductivity enhancement of S4 was 180 % at 200 G which improved to 230 % with 33 G/s ramp. S5 did not show notable improvement in thermal transport in the presence of external field. For 3 and 33 G/s ramps thermal conductivity enhancement shown by S5 was around 18%. In S45, for 3 G/s ramp maximum enhancement of 58 % was obtained at 60 G and significant enhancement was not observed with further increase in field strength. Similar trend was observed for 7, 10 and 17 G/s ramp though for higher ramps thermal conductivity showed improvement and for 33 G/s ramp significant enhancement was observed. For 17 G/s ramp S45 gave thermal conductivity enhancement of 103 % at 200 G which improved to 188 % for the same field strength with a 33 G/s ramp.

Aggregation kinetics is strongly affected by volume fraction and size distribution of particles[63, 65, 88], strength of the applied field[65, 69] and ramp rate of field application[222]. For polydisperse samples containing significant amount of larger particles, the nucleation stage is very short and occurs at relatively lower field strengths because of the large dipolar strength of the bigger particles. During the initial stages of a slow ramp rate, the larger particles initiate nucleation and as the strength of the applied field increases, growth of the nuclei into chains occurs, with simultaneous generation of new nuclei. In S4 and S45, thermal

conductivity gradually increases upto 50 G after which a plateau is observed for the 10 G ramp. This initial increase is attributed to the growth phase where tip-to-tip aggregation happens along with isolated zippering transitions. It is interesting to note that upto 80 G, S45 with greater measure of larger particles showed slightly better enhancement in thermal transport than S4. This is because of larger number density of chains present in S45 owing to the relatively faster aggregation kinetics brought about by the larger particles. The inherent polydispersity of the system gives rise to aggregates of different lengths and the longer ones can zipper even at low fields.

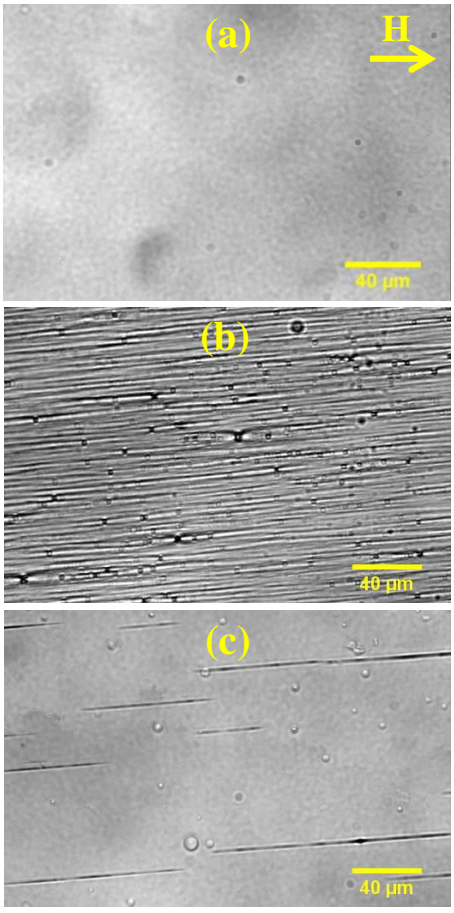

Figure 4.3: Phase contrast microscopy images showing the field induced microstructure of (a) S4, (b) S5 and (c) S45 when exposed to magnetic field of strength 200 G.

Fig. 4.3 shows the phase contrast microscopy images of S4, S5 and S45 exposed to magnetic field of strength 200 G. Observable aggregates were absent in S4 (**Fig. 4.3 (a)**) indicating that the field induced aggregates are nanosized. In S5 (**Fig. 4.3 (b)**) micronsized aggregates span the entire observation window for the same field strength because of the larger particles present in it. In S45 (**Fig. 4.3 (c)**) which contains relatively large quantity of bigger particles than S4, a few micron sized aggregates were observed which points towards the drastic change in aggregation kinetics that a small fraction of larger particles can bring about.

In S4 after a short plateau, thermal conductivity increases again upto 170 G after which it decreases. On increasing the field strength beyond 50 G, zippering transitions become prominent. In addition to lateral aggregation, individual particles in the vicinity of an aggregate can also be adsorbed onto it owing to the strong attractive interaction and new nuclei composed of smaller particles can also form. In S4 thermal conductivity decreased beyond 170 G due to decreased number density of chains brought about by widespread zippering. In S45, because of the significant number of larger particles, extensive lateral coalescence took place at much lower field strength than that observed for S4 and hence thermal conductivity did not show notable improvement above 50 G. For faster ramps thermal conductivity of S4 and S45 improved at higher field strengths because faster ramping leads to the simultaneous formation of large number density of chains as most of the particles, except for the limited population of very small particles, will interact strongly with the neighbors. For slow ramps on the other hand, during the start of the ramp, only aggregates composed of larger particles exist[222]. During later stages of the ramp other chains composed of relatively smaller particles form which are drawn towards the earlier formed aggregates. Eventually zippering takes place leading to the formation of thicker aggregates with considerably less number density of chains.

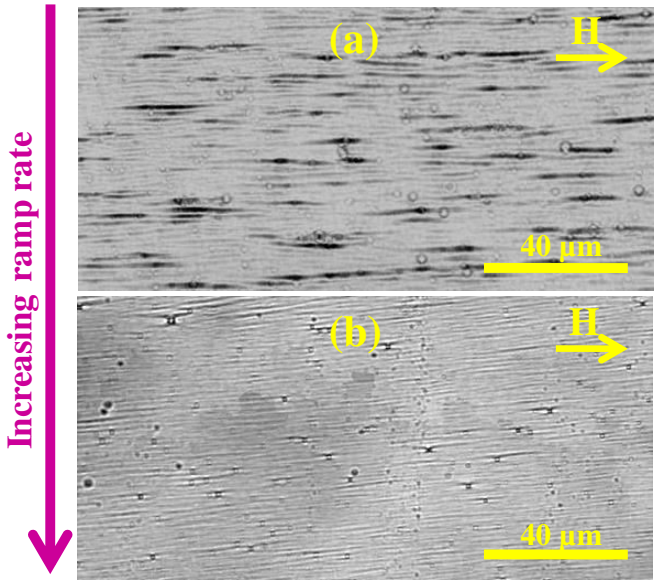

Figure 4.4: Phase contrast microscopy images of S5 showing the difference in microstructure when magnetic field of 200 G is applied in a (a) slow and (b) fast ramp.

Fig. 4.4 (a) and **(b)** show the field induced microstructure of S5 when the system is field quenched at ~200 G at slow and fast ramp, respectively. Since in S4 visible aggregates were absent and in S45 only a few visible aggregates were observed, phase contrast microscopy images is shown only for S5, even though the latter did not give notable enhancement in thermal conductivity. From the images in **Fig 4.4** it is clear that slower ramps lead to thicker aggregates while those formed during fast ramps are finer. Even the yield stress of a ferrofluid during a slow ramp was reported to be higher than that obtained during a fast ramp which indicates that the aggregates formed during slow ramps are thicker than their counterparts formed during fast field ramping[224]. Thicker aggregates mean lesser number density of aggregates. Fast ramping can thus prevent the reduction in number density of chains at higher field strengths as evidenced by the absence of reduction of thermal conductivity at high field strengths for ramp rates of 7, 10,

17 and 33 G/s in S4, and in S45 33 G/s ramp aided in preventing the reduction in thermal conductivity.

Only modest enhancement was observed in S5 even though space filling micron sized aggregates were observed in the microscopy images (**Fig. 4.3 (b)**). High thermal transport across an interface is only possible if the interfacial thermal conductance G is high. As discussed in chapter 3, extensive zippering transitions is detrimental to thermal transport owing to the reduction in number density of aggregates which can lead to reduced interaction between the aggregates and base fluid resulting in inefficient coupling of high frequency modes of the particles with the abundant low frequency modes of the base fluid.

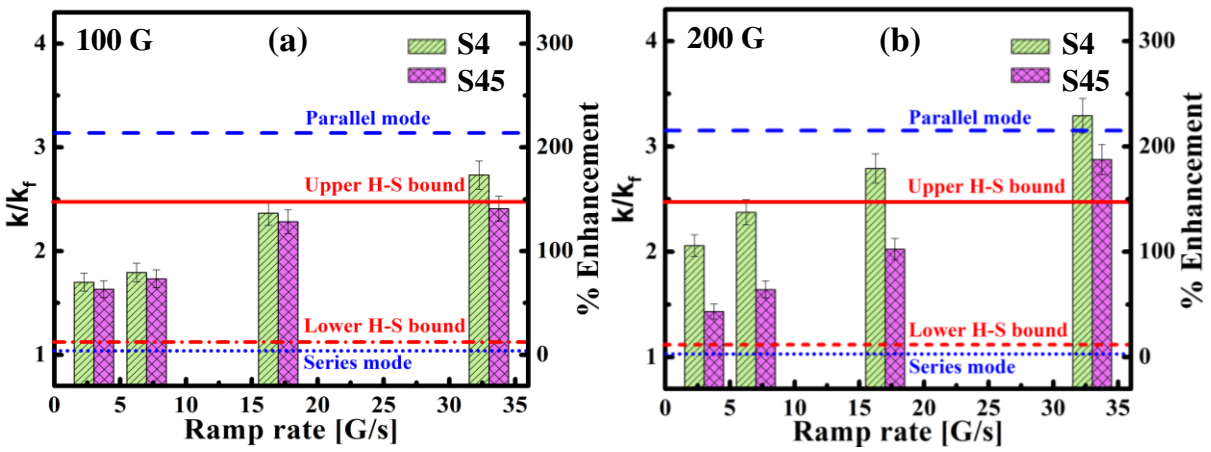

Figure 4.5: Variation of k/k_f of S4 and S45 as a function field ramp rate for (a) 100 and (b) 200 G. The solid and dashed red lines indicate the upper and lower H-S bounds, respectively, and the blue dashed and dotted lines indicate the values for k/k_f obtained using parallel and series mode of conduction, respectively, for volume fraction of 0.037.

Fig. 4.5 (a) and **(b)** indicate the variation of k/k_f in S4 and S45 with ramp rate for magnetic field strength of 100 and 200 G. The solid and dashed red lines represent upper and

lower Hashin-Shtrikman (H-S) bounds, respectively, calculated for volume fraction 0.037 (same as that of S4, S5 and S45). For 100 G (**Fig. 4.5 (a)**), except for 33 G/s ramp in S4, thermal conductivity of S4 and S45 for all ramp rates falls within the H-S bounds. For 200 G (**Fig. 4.5 (b)**), k enhancement is greater than the upper H-S bound for both systems for 33 G/s ramp. This could be because the H-S bounds are unable to capture the complexity of the thermal transport mechanism in ferrofluids in the presence of magnetic field. As discussed earlier, simple aggregation alone cannot explain the field induced anomalous enhancement in thermal transport in ferrofluids. Additional factors like liquid confinement need to be considered.

4.3.2 Variation of field tunable k with time

To study how temporal evolution of microstructure affects thermal transport, magnetic field of desired strength (50, 100, 150 and 200 G) was suddenly applied and thermal conductivity of S4 and S45 was recorded as a function of time and the results are shown in **Fig. 4.6**. Sudden switching on of higher magnitude magnetic field lead to enormous increase in thermal conductivity initially for both S4 and S45 which gradually decreased with time plateauing off beyond 15 min.

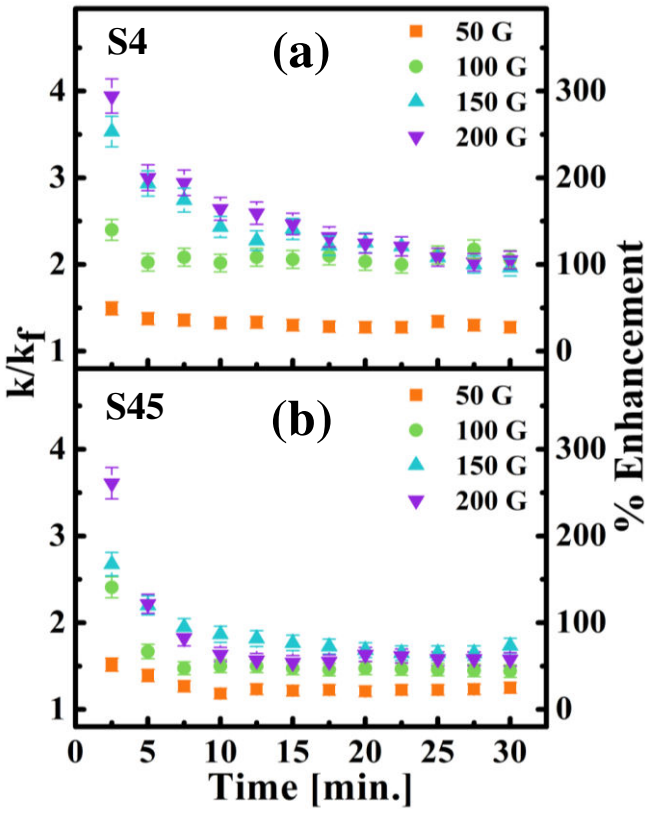

Figure 4.6: Variation of k/k_f with time of (a) S4 and (b) S45 for constant field strengths of 50, 100, 150 and 200 G.

When exposed to 50 G, k of S4 was only slightly higher than the value obtained for the same field strength during 3 G/s ramp (**Fig. 4.6 (a)**). As the microstructure slowly evolved, thermal conductivity decreased slightly and remained nearly constant beyond 10 min. For 100 G, thermal conductivity was higher than the slowest ramp (3 G/s) value throughout the time duration for S4 with a slight decrease with time. For 150 and 200 G, thermal conductivity was substantially higher than the slowest ramp initially though it decreased to that value with time. The initial huge increase in thermal conductivity, more pronounced at higher field strengths, is due to the simultaneous formation of large number of aggregates with sudden switching on of field. The substantial decrease is due to increased zippering transitions as strength of the applied

field strongly influences coalescence[225]. The time scale of lateral coalescence τ_l depends on the strength of the applied field as, $\tau_l \, \alpha \, H^{-2}$[64]. With increased lateral coalescence the number density of chains reduces leading to a decrease in thermal conductivity. However, with time aggregation kinetics slows down and thermal conductivity also becomes nearly time independent. For S45 (**Fig. 4.6 (b)**), even for 50 G there is a noticeable decrease in thermal conductivity with time because of the presence of larger particles that speed up aggregation. With sudden switching on of field to 50 and 100 G, even though thermal conductivity improves shortly after the field is switched on, it decreased even further than the value obtained for 3 G/s ramp. This is an indication of the faster aggregation kinetics in S45 when compared to S4. Just like in S4, sudden switching on of field to 150 and 200 G results in huge enhancement of thermal transport in S45 initially which later decreases and plateaus off at later time. Interestingly, for the higher field strengths (150 and 200 G), even after 30 min. thermal conductivity is still higher than what was achieved for the slowest ramp. With sudden switching the initial sudden decrease in thermal conductivity is because of lateral aggregation of the large number density of chains that form during fast ramps. However, after a certain time the immediate vicinity around an aggregate will not have any neighbors. In order to laterally coalesce further increasing the field strength becomes a requirement. Hence, after an initial period of active coalescence, aggregation kinetics slows down drastically resulting in nearly time independent thermal conductivity values beyond 15 min. So, rapid ramp rates or sudden switching on of field of high strength appears to give better thermal conductivity enhancement than slow ramps.

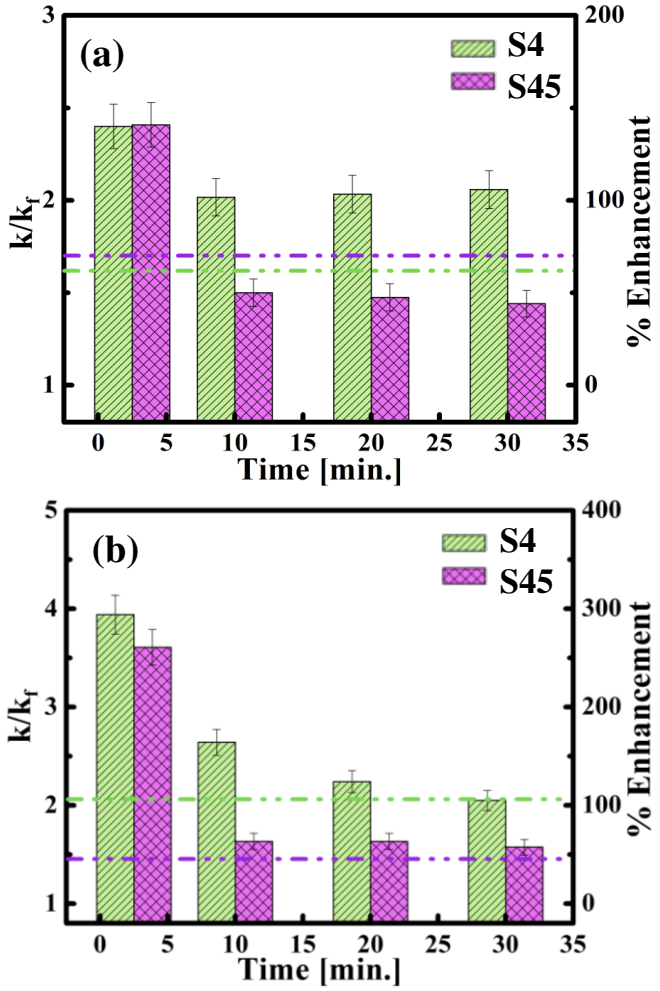

Figure 4.7: Variation of k/k_f with time of S4 and S45 on sudden exposure to magnetic field of strength, (a) 100 and (b) 200 G. The dashed lines indicate the value of k/k_f obtained during 3 G/s ramp for the corresponding field strength.

Fig. 4.7 (a) and **(b)** indicate the variation of k/k_f of S4 and S45 with time when suddenly exposed to magnetic field of strength 100 and 200 G, respectively. The dashed lines indicate the value of thermal conductivity obtained during the 3 G/s ramp for the corresponding field strength. Initially prominent increase in k/k_f can be seen in both S4 and S45 for 100 and 200 G. For 100 G (**Fig. 4.7 (a)**), even after 30 min. thermal conductivity of S4 was higher than that obtained during the slowest ramp while thermal transport of S45 decreased below the respective

slowest ramp value with time. For 200 G (**Fig. 4.7 (b)**) S4 and S45 displayed enhanced thermal transport beyond the value obtained for the slowest ramp upto 30 min.

S4 and S45 was exposed to on-off cycles of 100 and 200 G over a time period of 62.5 min. The dotted lines indicate the value of thermal conductivity obtained for the respective field strength during slow ramp of 3 G/s.

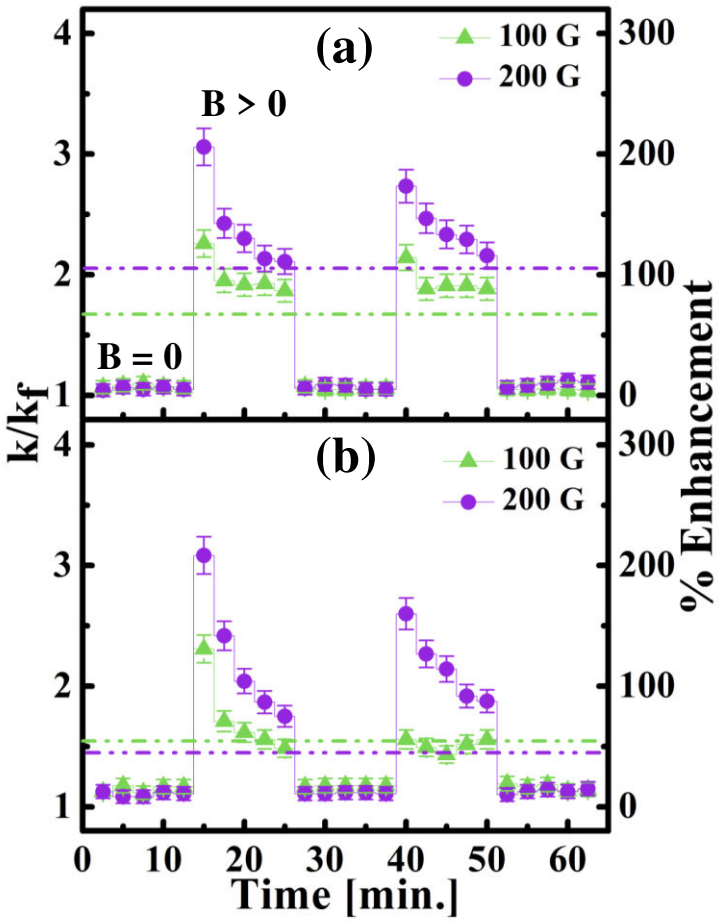

Figure 4.8: Variation of k/k_f with time of (a) S4 and (b) S45 when exposed to on-off cycles of magnetic field of strength 100 and 200 G. The dashed lines indicate the value of k/k_f obtained during 3 G/s ramp for the corresponding field.

In **Fig. 4.8**, during the field on-off cycles, when the magnetic field was turned off, thermal conductivity of S4 and S45 came down to the zero field value and minor variations in k/k_f are due to local density fluctuations. The fact that thermal conductivity comes down to the same zero field value after every field on cycle indicates that both the ferrofluid systems are quite stable, even S45 with larger fraction of bigger particles. For 100 and 200 G, thermal conductivity value throughout the on-cycle for S4 (**Fig. 4.8 (a)**) is higher than that obtained during the slowest ramp. In S45 (**Fig. 4.8 (b)**) for the 100 G cycle, owing to the presence of more number of larger particles, the value obtained is more or less similar to the slow ramp case without much improvement.

4.4 Conclusions

The impact of magnetic field ramp rate on the field dependent thermal transport exhibited by ferrofluids with different size distributions was thoroughly explored, using two different kerosene based ferrofluids (S4 and S5) composed of oleic acid coated magnetite nanoparticles and a third system, S45 which was a mixture of S4 and S5 in the ratio 95:5, respectively. The volume fraction of all the systems was maintained at 0.037 and they differed from each other in their size distribution alone. S4 and S45 displayed significant enhancement in thermal conductivity with field while S5 did not show notable improvement for low and high magnetic field ramp rates owing to the presence of significant amount of larger particles due to which aggregation kinetics was much faster in the latter leading to increased zippering transitions which decreased the number density of field induced aggregates drastically. Higher ramp rates were found to improve thermal conductivity notably even in S45 where thermal conductivity enhancement during 3 G/s ramp was much lower than S4 due to presence of greater amount of larger particles in it. For 17 G/s ramp, thermal conductivity enhancement of S4 was 180 % at 200

G which improved to 230 % with 33 G/s ramp. For 17 G/s ramp S45 gave thermal conductivity enhancement of 103 % at 200 G which improved to 188 % for the same field strength with 33 G/s ramp. From the phase contrast microscopy images, slower ramp was observed to generate a field induced microstructure composed of thicker aggregates than a fast ramp, considerably decreasing the number density of aggregates. Hence faster ramps resulting in simultaneous formation of large number density of fine aggregates was found to be better for thermal conductivity enhancement. On sudden exposure to magnetic field, particularly for higher strengths, substantial improvement in thermal conductivity was observed in both S4 and S45 initially, though with time zippering transitions reduced the number density of chains and thermal conductivity decreased. However, for the fastest ramp employed (33 G/s) to 200 G even after a time period of 30 min. thermal conductivity was still higher than the corresponding value obtained for the slowest ramp (3 G/s). For higher field strengths, faster ramps are more beneficial for thermal transport and for avoiding the decrease in thermal conductivity with time, alternate magnetic field on-off cycles was found to be effective. Additionally, with faster ramps thermal conductivity in a system with moderate amount of larger particles can be significantly improved from the values obtained during slower ramps. These results provide new means of improving field induced thermal transport of a ferrofluid through fast field ramp rates without altering the physical properties of the magnetic fluid.

Chapter 5 Rheological study of the effect of magnetic field quench rate on aggregation kinetics, yielding and aging of ferrofluid

5.1 Introduction

Ferrofluids, with their wide array of technological applications, have been the subject of intense research over the past years, in spite of which most studies were limited to magnetic field induced equilibrium aggregates. Ferrofluids, exposed to magnetic field, possess a very rich and complex phase diagram expressed as function of strength and ramp rate of applied field[226]. Equilibrium field induced aggregates typically form when the external field is applied at a slow ramping rate. During the initial stages of a slow quench, thermal energy is still significant, compared to magnetic energy, thereby enabling the particles to explore the energy landscape and settle into minimum energy configurations. However, during fast field quench, magnetic interaction dominates over Brownian motion almost immediately, interlocking the aggregates into complex configurations[222, 223]. Under fast ramping of magnetic field, if the volume fraction of particles is high enough, the field induced aggregates become trapped in the repulsive potential of their neighbors and are forced to settle into metastable states. Many other soft materials like foams, emulsions, pastes etc. also exist in metastable states and they share similar rheological properties. Such disordered materials that exist in metastable states come under a category of soft matter called soft glassy materials[227]. The formation of soft glassy state in ferrofluids with rapid field quench is very similar to that of molecular glasses and colloidal glasses where the parameter that determines the entry of the system into glassy state is temperature in the former and volume fraction in the latter. One common feature of soft glassy materials is that they age with time. In an effort to reach equilibrium, the microstructure slowly evolves with time which results in time dependent rheological properties and the system is said to age. Aging has been explored in several soft systems like metallic glasses, microgels, pastes

etc. For many technological applications, ferrofluid is subjected to faster quench rates (e.g. optical switching, magnetic hyperthermia, smart thermal cooling devices, actuators etc), where the behavior is little known. In this work the effect of applied magnetic field quench rate on the rheological properties of an oil-based ferrofluid is experimentally investigated.

5.2 Materials and methods

Oleic acid coated magnetite nanoparticles were prepared by chemical co-precipitation technique which is detailed in section 2.1 of chapter 2. Kerosene based ferrofluid, S3, of volume fraction 0.037 (corresponding to 20 wt.%) was employed in this study. **Table 5.1** summarizes the obtained results of ferrofluid characterization, details of which can be found in section 2.10 of chapter 2.

Table 5.1: Sample code and characterization details.

Sample code	Avg. Crystallite size [nm]	Most probable hydrodynamic size [nm]	Polydispersity index	Saturation magnetization [emu/g]	Surfactant weight loss [%]
S3	10.5 ± 1	21 ± 1	0.79	71 ± 0.7	19

The rheological measurements were performed as described in chapter 2.

5.3 Results and discussion

An important factor that impacts aggregation kinetics, the effects of which has not been thoroughly probed, is the ramping rate of the applied magnetic field. On subjecting the ferrofluid to slow magnetic field quench, the particles can explore and settle into a lower energy state by virtue of the thermal energy possessed by them, since the dipolar interaction between the particles is not yet strong enough to prevent Brownian motion. On the other hand, with sudden

application of magnetic field, the particles are forced into metastable states as the strong dipolar interaction prevents them from moving around, depriving them of the chance to settle into low energy states[222]. Slow ramping rates results in the formation of equilibrium structures and the microstructure is commonly observed to be composed of chains or columns[64]. Fast ramping rates leads to the formation of non-equilibrium structures that are quite complex and the microstructure ranges from columns to bent wall-like to labyrinthine depending on cell thickness, volume fraction etc[223].

5.3.1 Effect of magnetic field ramp rate on yield stress

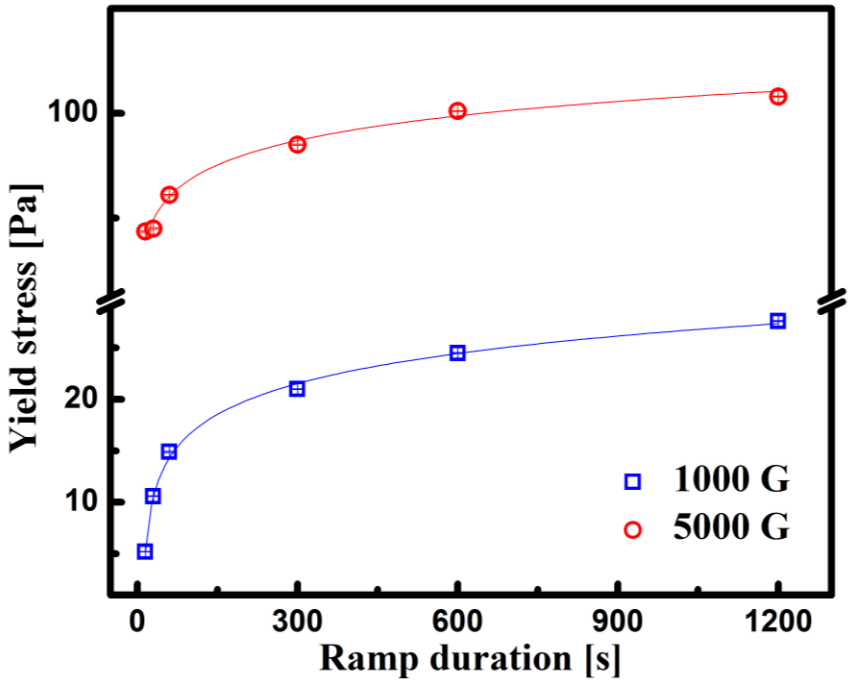

Figure 5.1: Variation of yield stress with magnetic field quench duration for 1000 and 5000 G. The solid lines represent logarithmic fit to the data.

The difference in microstructure with ramping rate of applied field manifests in the rheological properties of the ferrofluid. For example, the yield stress of a ferrofluid at a particular

magnetic field is found to be higher for slow ramping where equilibrium structures form than for fast ramping. **Fig. 5.1** shows the variation of apparent yield stress as a function of duration of field ramp for 1000 and 5000 G. The yield stress was obtained by fitting the high shear region of the flow curve with the Casson model (eq. (1.25) in section 1.5.1.2 in chapter 1). For 1000 G, the apparent yield stress varied from ~5 Pa for ramp duration of 15 s to ~ 28 Pa for 1200 s duration and for 5000 G the variation was from ~89 to 102 Pa as the duration of ramp increased from 15 to 1200 s.

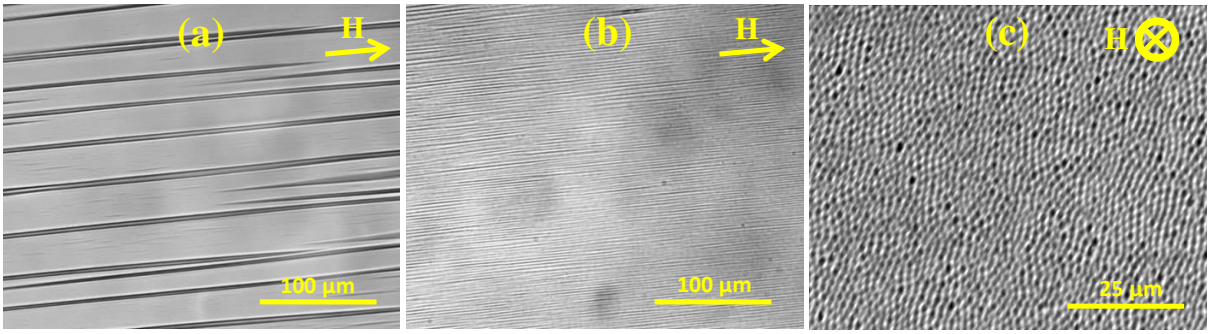

Figure 5.2: Phase contrast microscopy images showing the ferrofluid microstructure when subjected to (a) slow and (b) fast magnetic field quench of ~630 G. (c) The field induced aggregates formed during fast field quench (~300 G) viewed perpendicular to the direction of applied field.

From the microscopy images in **Fig. 5.2** one can see that the equilibrium structures are longer and coarser than the nonequilibrium ones and hence the higher yield stress for longer ramps. For slower ramps, initially only a small fraction of the dispersed phase composed of larger particles, with higher dipole moments, interact and involve in chain formation and since thermal energy is still greater or comparable to magnetic energy during the initial part of the ramp, the particles will be able to explore the energy landscape and settle into a lower energy

configuration. On account of the slowly increasing field, the neighboring single chains zipper and coarsen and at the same time other smaller sized particles begin to form single chains. Eventually, thick and long chains form, which do not deform or break easily in a shear field applied perpendicular to the external magnetic field. When the field ramp is high, particularly for higher field strengths, the rapidly increasing field forces a large fraction of the particles to interact and form chains immediately after the commencement of the ramp. Single chains also undergo zippering if the chains are in off-registry. If the volume fraction of particles is high enough, then faster ramps result in the simultaneous formation of a large number of short chains which then undergo zippering transitions. Then owing to the large number density of chains, structural arrest ensues since the aggregates cannot coarsen further easily. The compositions of the chain are such that large particles are concentrated in the cores of the chains, since they aggregate first, and small particles form coronae which means that the structure of a single chain does not correspond to the lowest-energy configuration. The effective interactions between the chains are screened by the coronae of small particles, and there is a large energy barrier precluding large-scale reorganization of the system on the experimental time scale. These short chains can be easily broken apart by shear and hence the observed lower yield stress. The difference in the yield stress with ramp rate is more pronounced for 1000 G than 5000 G. This is because for the same ramp duration, the rate of increase of field strength is higher for 5000 G than 1000 G (five times faster). For example, for a ramp duration of 60 s, the aggregates formed at 1000 G (ramp rate is ~17 G/s) are closer to equilibrium than those at 5000 G (ramp rate is ~83 G/s) since the increase in field magnitude is slower for the former. Zhu et al.[228] found that equilibrium columnar aggregates that form in a magnetorheological fluid during slow ramping possessed higher dynamic yield stress than the non-equilibrium bent wall aggregates which form

as a consequence of fast field quench. Chaker et al.[224] also obtained higher yield stress for slow ramping of applied field in magnetorheological fluids. Additionally, they observed that for higher field strength or larger volume fraction, the difference in yield stress as a function of magnetic field ramp rate became more prominent.

5.3.2 Mason number scaling

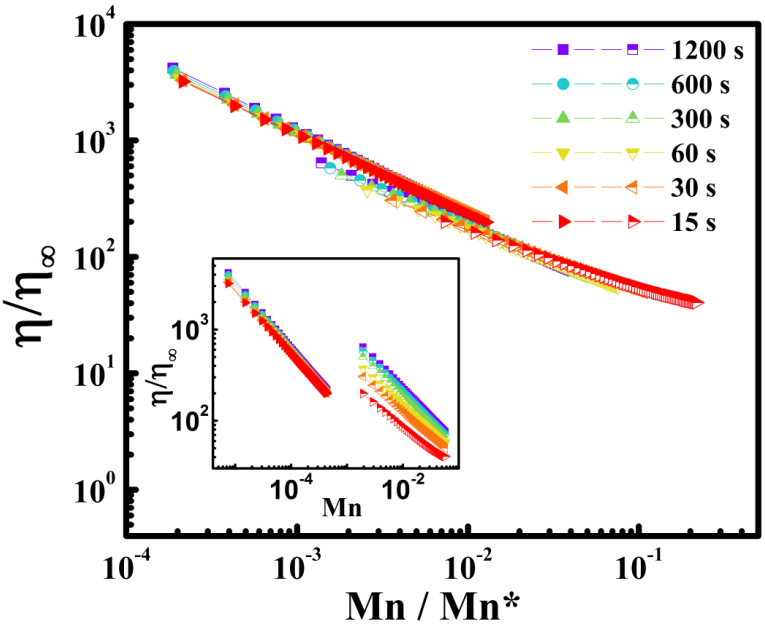

Figure 5.3: Dimensionless viscosity as a function of Mn/Mn* at different field quench rates of 1000 (half filled symbols) and 5000 G (solid symbols). All the curves superpose reasonably well. The inset shows the scaling of the same data with Mn.

Over the years it has become common practice to scale the performance of ferrofluids and magnetorheological fluids with a dimensionless entity called the Mason number (Mn), which is the ratio of hydrodynamic force to magnetic force[107]. The advantage of Mason scaling is that one can analyze the performance of the magnetic fluid without the tedious acquisition of data under different working conditions since the deformation due to the applied shear and

impact of strength of the applied field on the fluid can be characterized by Mn alone. Owing to its usefulness, Mn was modified to take into account surface forces in case of charged suspensions[229]. Becnel et al.[230] incorporated a temperature factor into Mn and the authors were able to collapse data acquired at different temperature onto a master curve. In the case of suspensions exposed to magnetic field strengths below saturation magnetization, Mn is given by eqn. (1.23) (section 1.5.1.1 in chapter 1). For strong magnetic fields, where the particles are closer to saturation, the mean magnetization of the dispersed particles is equal to the volume saturation magnetization of the particles, $M_{p,s}$. Here the Mason number becomes

$$Mn = \frac{72\eta_c\dot{\gamma}}{\mu_0\mu_c {M_{p,s}}^2} \tag{5.1}$$

Inset of **Fig. 5.3** shows dimensionless viscosity, $\frac{\eta}{\eta_\infty}$, as a function of Mason number for different ramp rates of applied field of strength 1000 and 5000 G. Here η_∞ is the field independent high shear viscosity. Since a high shear plateau was not obtained within the experimental window, the high shear viscosity was calculated using the expression, $\eta_\infty = \eta_c \left(1 - \frac{\Phi}{\Phi_{max}}\right)^{-2}$, where Φ is the volume fraction and Φ_{max} is the maximum packing fraction which is taken as 0.64 in this particular case. For 1000 G (moderate field strength) eqn. (1.23) and for 5000 G (high field strength where the particles are close to being magnetically saturated) eqn. (5.1) was used for Mason number calculation. Vast differences in the microstructure with increasing yield stress for different field quench rates for the same magnetic field strength leads to poor collapse of the curves with Mason scaling. So a simple Mason scaling is not enough and in this current scenario it is a requisite to involve the critical Mason number in the scaling since it brings yield stress into picture[231, 232]. The critical Mason number is defined as

$$Mn^* = \frac{72\tau_y\eta_c}{\mu_0\mu_c\eta_\infty\langle M_p\rangle^2} \quad (5.2)$$

Fig. 5.3 shows the dimensionless viscosity as a function of Mn/Mn*. All the curves show reasonable collapse onto a master curve.

5.3.3 Effect of magnetic field ramp rate on viscoelastic properties

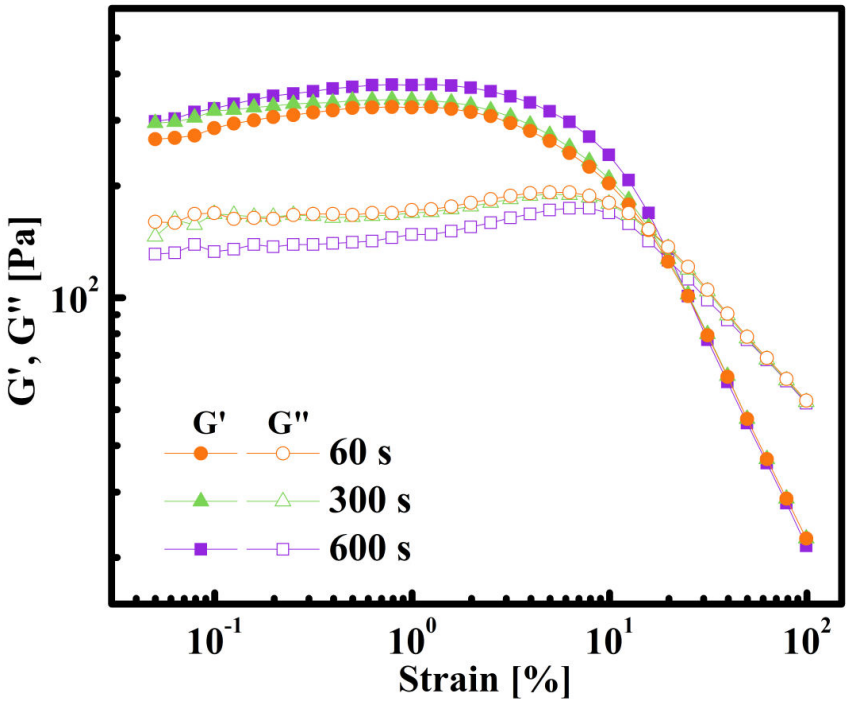

Figure 5.4: Variation of G' and G" with strain at field strength of 3500 G at different ramp durations of 60, 300 and 600 s.

Fig. 5.4 shows the response of the ferrofluid exposed to field strength of 3500 G applied at ramp durations of 60, 300 and 600 s, respectively, as a function of strain amplitude at a constant frequency of 10 rad/s. Below 1% strain amplitude, the storage modulus, G', and the loss modulus, G", are more or less independent of the applied strain. The storage modulus was found to be larger for slower ramp rates while the loss modulus decreased. This is another indication

that the field induced structures formed as a result of slow ramps are more rigid. Beyond ~1% strain G' shows a steep decrease with increasing strain while G" increases initially, reaches a maximum and then declines sharply indicating the onset of nonlinearity. The peak in G" is ubiquitous in many soft matter systems and is commonly attributed to maximum energy dissipation before destruction of microstructure[110, 233]. Further increasing the strain amplitude results in the destruction of the field induced aggregates and a cross-over of G' and G" is observed. The cross over strain was around 15.4, 16.6 and 21.3 % for 60, 300 and 600 s, respectively.

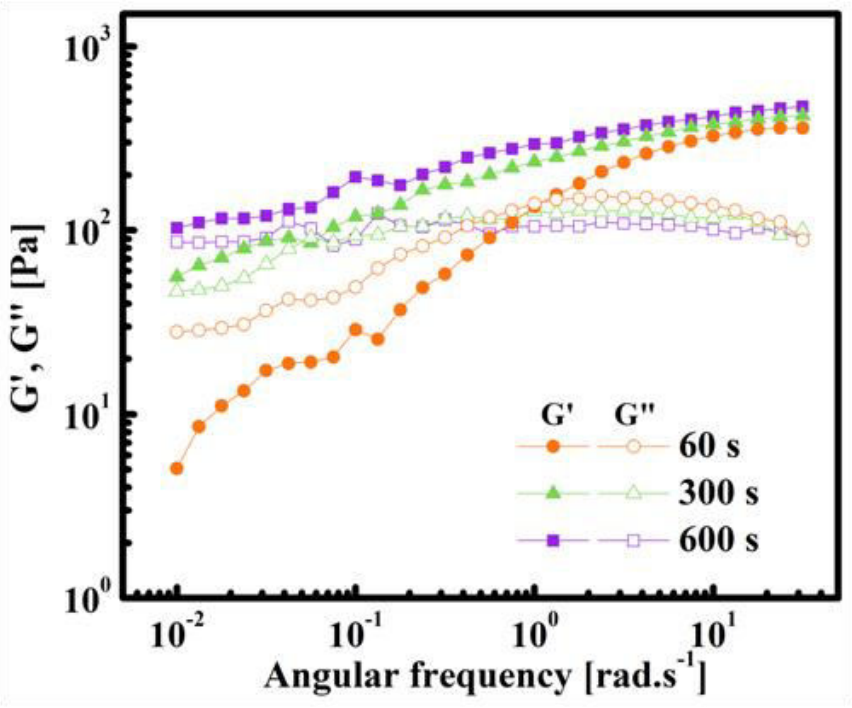

Figure 5.5: Variation of G' and G" with angular frequency at field strength of 3500 G at different ramp durations of 60, 300 and 600 s.

Fig. 5.5 shows the viscoelastic moduli of the ferrofluid exposed to magnetic field of 3500 G, as a function of frequency of applied strain of constant amplitude, 0.4 %. For all ramp

durations G' shows a monotonic decrease towards lower frequency, the decrease being more prominent for the shortest ramp duration. For the shortest ramp duration (60 s) a clear cross-over of G' and G" (t ~ 1 s) is seen with G' > G" at the higher end of the frequency spectrum, indicating the presence of a fast structural relaxation. With slower ramp duration similar relaxation could not be seen within the accessible experimental window though there is clear indication of imminent crossover at even lower frequency. It appears that the relaxation has been shifted to lower frequencies. Similar behavior was reported for aging colloidal glasses by Negi et al.[234] where the relaxation time increased with age. Analogous to increasing the quench time, aging the system moves it closer to equilibrium. Since the aggregates that form during slow quenching of magnetic field are closer to equilibrium, they exhibit slower relaxation than those that form during fast quench. Many soft matter systems exhibit high frequency relaxations as observed in our system for the fast magnetic field quench. In a glassy colloid, Peng et al.[235] reported similar crossover of G' and G" during frequency sweep with the cross over frequency shifting towards the lower end of the frequency spectrum with increasing volume fraction of particles due to slower dynamics owing to crowding. For polymers in the entanglement regime the fast relaxation is attributed to reptation[236]. Fast relaxation was also observed in the initial response of star polymer after rejuvenation which later shifted to longer time scales with aging[237]. This relaxation was attributed to exploration of cages by the star polymers. Fast relaxations were reported for metallic glasses, the source of which was attributed to motions of individual units occurring in less denser areas, popularly called "soft spots" or "islands of mobility" in a spatially heterogeneous arrangement[238]. This type of β-relaxation is called Johari-Goldstein relaxation, the time scale of which ranges from microseconds to seconds. The field induced aggregates vary in length and breadth and this diversity itself ensures the existence

of tightly and loosely packed areas. Zhu et al.[239] obtained direct experimental evidence of the intrinsic relationship of β-relaxation to spatial heterogeneity in hyper-quenched metallic glasses. Fast and slow relaxation was observed in the master curves of time-temperature superposition of Selenium and Selenium based inorganic glasses[240]. The slow relaxation was attributed to dynamics of Se bond while the fast relaxation is assigned to Johari-Goldstein relaxation. Wen et al.[241] probed the dynamics of a soft colloidal glass using time-concentration superposition and they attributed the frequency independent G" at the higher end of the frequency spectrum of the superposed master curve to in-cage rattling while the cross-over of G' and G" was attributed to cage escape. For the slow quench, the bulky structures are closer to equilibrium, in very deep potential wells. Consequently G" is nearly frequency independent (cage rattling) in the experimental window since cage escape is going to be more tougher than the fast quench case where the potential wells are less deep and the aggregates are less bulky. For the fastest quench G" exhibited a broad maxima which became less prominent for 300 s quench duration and was absent for 600 s quench duration. This peak is most likely to be associated with β-relaxation though further experiments are required for explicit assignment.

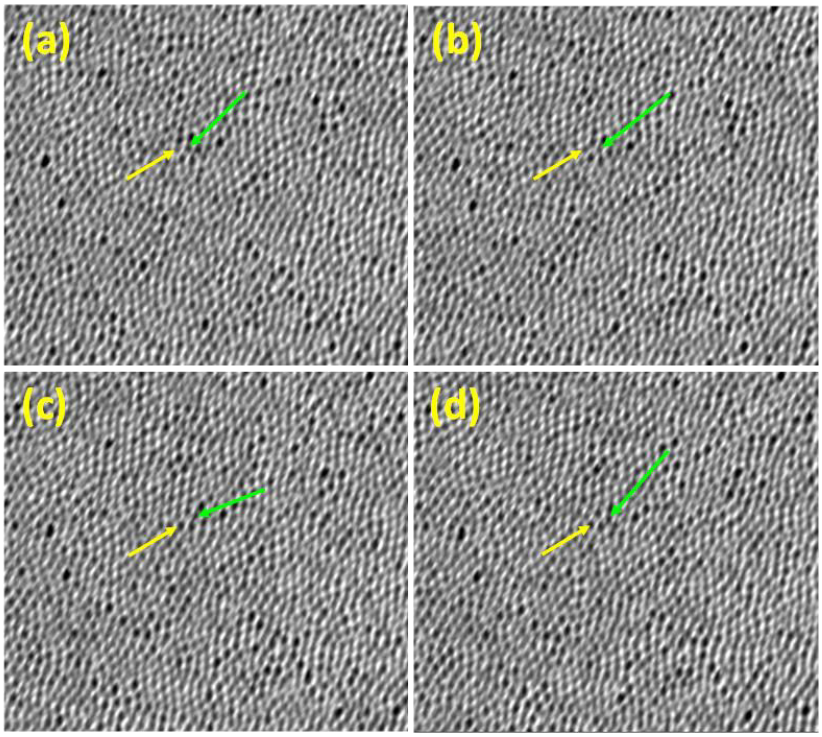

Figure 5.6: Snapshots of field induced microstructure for fast field quench at field strength of ~300 G viewed perpendicular to the direction of applied field. The aggregate taken as reference is indicated by the green arrow. In (a), the aggregate indicated by the yellow arrow is one of the nearest neighbors of the reference aggregate. In (b) and (c) it moves further away from the reference until it is no longer one of the nearest neighbors as observed in (d).

Fig. 5.6 shows snapshots of the microstructure at field strength of ~300 G, where the field of view is perpendicular to the applied field. The green arrow indicates the aggregate which is taken as reference and the yellow arrow indicates one of its nearest neighbors or in other words it is one among the six aggregates caging the reference. With time, the aggregate indicated by the yellow arrow moves away from the reference (**Fig. 5.6 (b)** and **(c)**) and is no longer the nearest neighbor of the reference (**Fig. 5.6 (d)**). Through computer simulations Ozawa et al.[242] reported that even in a deeply quenched glassy state localized excitations are possible in

relatively more mobile areas and also that rearrangements are more likely around units which have relatively fewer nearest neighbors with larger angles between adjacent units[243, 244].

5.3.4 Aging in the presence of magnetic field

To unravel the relaxation dynamics of ferrofluid in the soft glassy state, creep experiments were performed. Slow evolution of the microstructure towards equilibrium results in creep dynamics that depend on the time elapsed since the application of field and the beginning of rheological test. This results in the breaking of time-translational invariance from which one can infer that the system is non-ergodic. The rheological properties become a function of the waiting time, t_w due to the continuously evolving microstructure. For soft glassy materials, the time dependent relaxation time, $\tau_r(t_w)$ is observed to vary with t_w as a power law and is given by $\tau_r = A'\tau_m^{1-\mu'}t_w^{\mu'}$[245, 246], where τ_m is the microscopic relaxation time associated with aging and μ' is a positive exponent. In microgels, Cloitre et al.[247] observed that in creep tests, for probe stresses that are high enough to cause large microstructural rearrangements but lower than the yield stress, strain curves at different wait times collapsed over one another when scaled with $(t - t_w)/(t_w^{\mu'})$. If $\mu' < 1$, then the system is said to be in the sub-aging regime, $\mu' > 1$ indicates that the system is superaged and $\mu' = 0$ indicates that the system is not aging. The exponent is non-universal and is a function of the applied probe stress[248]. In this present work, to study aging, the following rheological protocol was adopted: The sample was sheared at 100 s^{-1} for 60 s to ensure repeatability of test. Then under quiescent condition the sample was subjected to field strengths of 1000 and 5000 G at two different ramp durations of 15 and 600 s. Then, again under quiescent condition, the field induced microstructure was allowed to evolve at waiting times of 60, 600 and 1800 s. At the end of the waiting time a constant stress, less than the yield stress,

was applied to the system and the rheological response was studied. The probe stress applied for 1000 and 5000 G are 3 and 20 Pa, respectively.

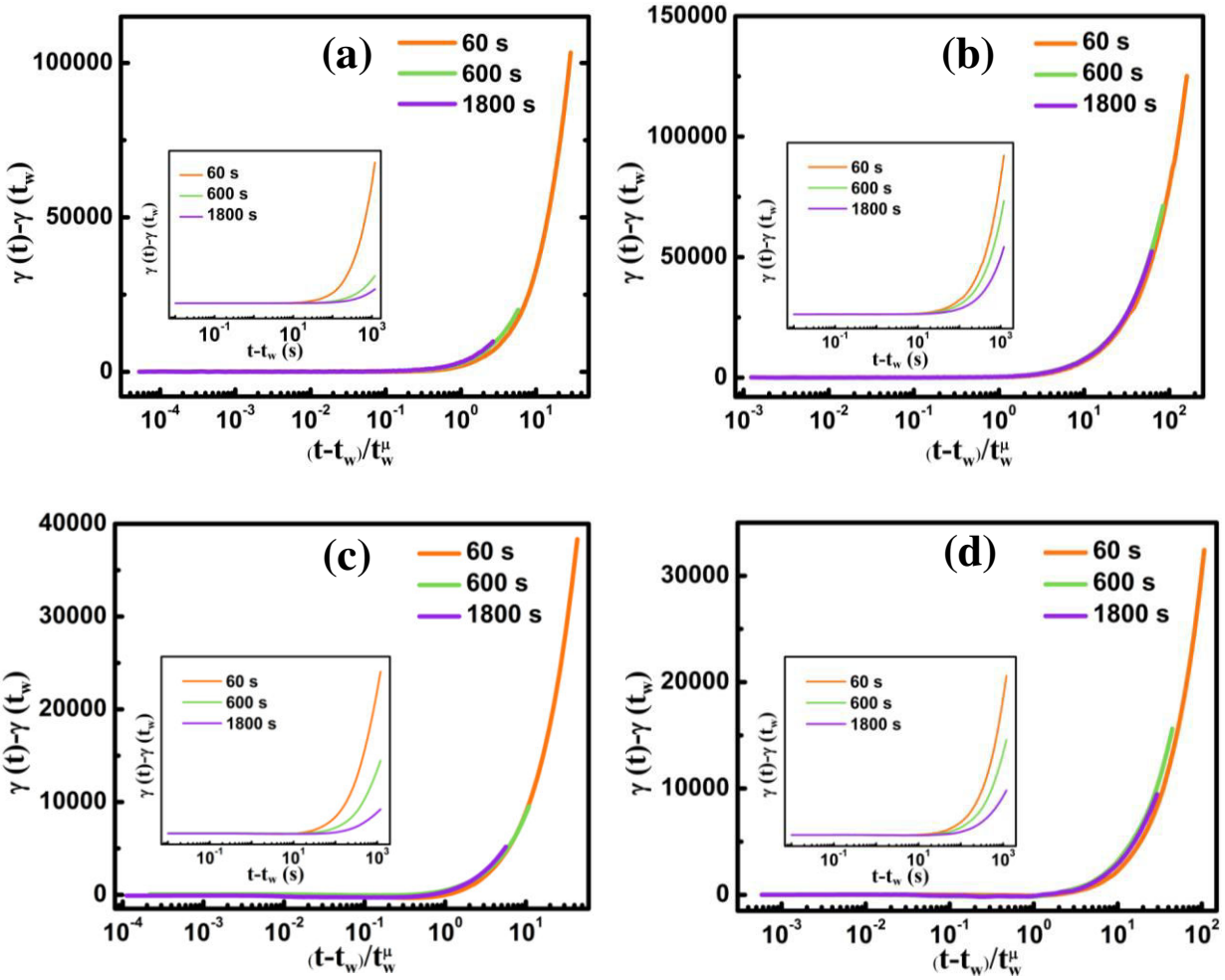

Figure 5.7: Strain response during creep measured at different waiting times as a function of $t - t_w / t_w^{\mu'}$ for (a & b) 1000 and (c & d) 5000 G. The left panel (a & c) is for ramp duration of 15 s and the right panel (b & d) is for duration of 600 s. The inset of all the graphs shows the corresponding creep curves as a function of $t - t_w$.

Inset of **Fig. 5.7 (a-d)** shows the strain response on application of probe stress after t_w and the response is found to be higher for the shortest waiting time for all field strengths. The

system has evolved more for longer wait times and hence the strain response is weaker. After the application of probe stress, strain remains constant for some time after which it shows a continuous increase which signifies strain recovery. On plotting the strain curves as a function of $t - t_w \Big/ t_w^{\mu'}$, all the curves collapse onto each other reasonably well for 1000 G (**Fig. 5.7 (a & b)**) and 5000 G (**Fig. 5.7 (c & d)**). The value of exponent μ' for 15 s ramp duration was 0.7 and 0.6 for 1000 and 5000 G, respectively. For faster ramps the aggregates are trapped in potential wells of their neighbors and their evolution towards equilibrium is very slow. For ramp duration of 600 s, the exponent obtained is 0.28 and 0.38 for 1000 and 5000 G, respectively. The exponent for 600 s ramp duration is less than that for 15 s for all field strengths since slower ramps allow the particles to settle into lower energy states and the resulting microstructure is therefore closer to equilibrium than the aggregates resulting from faster ramps.

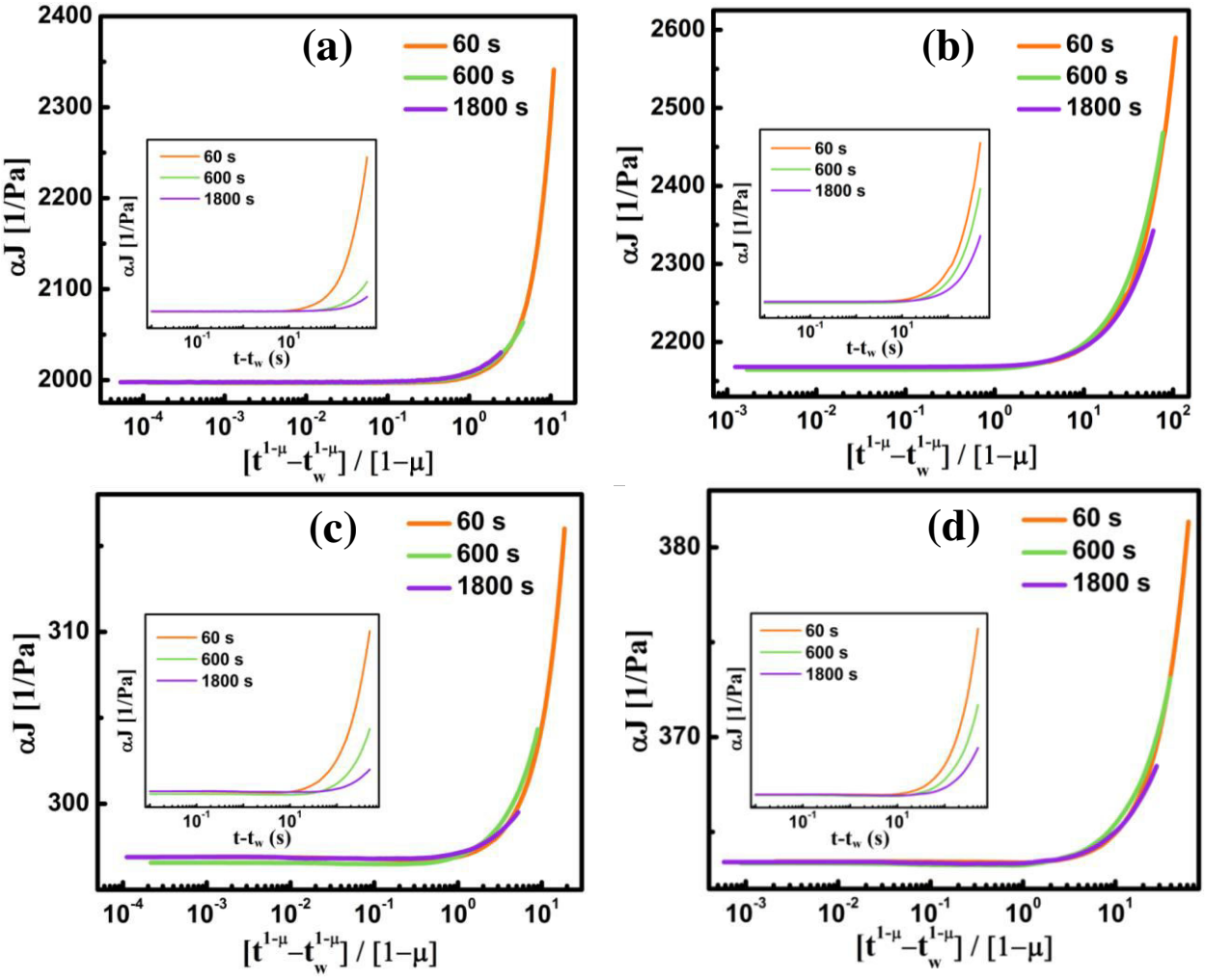

Figure 5.8: Vertically shifted creep compliance curves measured at different waiting times as a function of $\frac{(t^{1-\mu\prime}-t_w^{1-\mu\prime})}{(1-\mu\prime)}$ for (a & b) 1000 and (c & d) 5000 G. The left panel (a & c) is for ramp duration of 15 s and the right panel (b & d) is for duration of 600 s. The inset of all the graphs shows the corresponding creep curves as a function of $(t - t_w)$.

Another rheological variable that can be computed from creep test is the creep compliance. Soft materials which follow time translational invariance have a strain response that can be expressed as

$$\gamma(t) = \int_{-\infty}^{t} J(t - t_w) \frac{d\sigma*}{dt'} dt' \tag{5.3}$$

where the integration is over all past times, t', since the application of probe stress, upto the current time, t, J is the creep compliance, $\sigma*$ is the shear stress. For constant probe stress, the creep compliance of soft glassy materials does not follow time-translational invariance and it is a function of not just the time elapsed since the application of stress but also depends on the time at which the probe stress is applied. For aging soft glassy materials, creep compliance is expressed in terms of an effective time given by[249, 250]

$$\xi(t) = \int_{0}^{t} \tau_0 \frac{dt'}{\tau(t')} \tag{5.4}$$

where τ_0 is the constant relaxation time. In the effective time scale the strain response is given by

$$\gamma(t) = \int_{-\infty}^{t} J(\xi(t) - \xi(t_w)) \frac{d\sigma*}{dt'} dt' \tag{5.5}$$

Using the expression for $\xi(t)$ (eqn. 5.4), the effective time difference

$$\xi(t) - \xi(t_w) = \frac{\tau_0 \tau_m^{\mu'-1}}{A'} \left[\frac{t^{1-\mu'} - t_w^{1-\mu'}}{1-\mu'} \right] \tag{5.6}$$

Hence, the creep compliance is a function of $\frac{t^{1-\mu'} - t_w^{1-\mu'}}{1-\mu'}$ and plotting J in the effective time scale leads to superposition of all the creep compliance curves obtained at different waiting times[251, 252]. **Fig. 5.8 (a)** and **(c)** shows the creep compliance curves for ramp duration 15 s and **(b)** and **(d)** are for 600 s ramp duration and the inset shows creep compliance curves plotted as a function of $t - t_w$. The curves were vertically shifted by α whose value is close to 1. When

creep compliance is plotted as a function of $\frac{t^{1-\mu'}-t_w^{1-\mu'}}{1-\mu'}$ the curves superpose on each other reasonably well for the same value of μ' used for superposition of strain curves as (**Fig. 5.7**). Hence, the system follows time translational invariance in the effective time domain. The superposition of strain and creep compliance curves obtained for different waiting times in the effective time domain confirms that ferrofluid systems can be considered as soft glassy systems, provided that the volume fraction of magnetic nanoparticles and the strength of the applied field are high enough. Ferrofluids are exciting candidates to probe aging and glassy dynamics due to the advantage of being able to observe the rich dynamics directly in real space (using optical microscopy) and also because of the ease with which dynamics can be tuned by varying magnetic field strength, field quench rate, volume fraction and size of magnetic nanoparticles etc.

5.4 Conclusion

The effect of magnetic field quench rate on the rheological properties of a ferrofluid was probed. Slower quench rate resulted in the formation of long and coarse aggregates that are closer to equilibrium while faster quenches resulted in the formation of large number of out of equilibrium interlocked thinner and shorter columns. Consequently, the yield stress in the former case was found to be higher. The differences in microstructure were also captured by oscillatory rheology. In the linear viscoelastic region, for the fastest field quench rate, a fast relaxation was observed which was pushed to the lower end of the frequency spectrum with increase in ramp duration. This relaxation is probably due to motion of aggregates in less denser regions. In the presence of magnetic field, ferrofluid was found to disobey time translational invariance and underwent aging with continuous evolution of microstructure as a result of which strain and

creep compliance showed extra dependence on the waiting time before the beginning of rheological test. However, when the curves are scaled with respect to an effective time domain, time translational invariance was recovered, just like other soft glassy materials. For longer ramp durations, the microstructure is closer to equilibrium and hence the exponent used for scaling time domain to an effective time domain was found to be smaller than shorter ramps.

Chapter 6 Effect of particle size distribution on field induced deformation of sessile ferrofluid droplets

6.1 Introduction

Effect of particle size and volume fraction, polydispersity, strength and direction of magnetic field etc. on magnetic field induced changes in thermal, rheological and optical properties of ferrofluids have been thoroughly probed over the years. However, very few reports on field dependent wetting of ferrofluid droplets exist. Spreading and shape profile of ferrofluid droplet on a solid substrate can be easily manipulated by an externally applied magnetic field. In the presence of external magnetic field, the shape of a ferrofluid droplet is deformed and the equilibrium shape will be determined by the balance of gravitational, magnetic and surface energies[177]. Shape profile and spreading of ferrofluid droplets depend on nanoparticle concentration and orientation and magnitude of magnetic field[173]. Ferrofluid droplets of larger volume and high permeability were observed to deform more in the presence of magnetic field[179]. The mobility of ferrofluid droplets across a substrate can also be controlled using magnetic field and they can also be used as templates to control wetting properties of other liquids[183, 253]. Thorough understanding of spreading of ferrofluids on a solid substrate and their wetting properties are crucial for applications in microfluidics and magnetic actuation. Particle size distribution affects field induced physical properties of ferrofluids drastically. However, this particular aspect has not received much attention in terms of field induced spreading and droplet deformation. The objective of this study is to probe the effect of particle size distribution on aggregation kinetics and the ensuing changes in the field induced deformation of sessile ferrofluid droplets when the magnetic field is applied perpendicular to the substrate surface.

6.2 Materials and methods

Oleic acid coated magnetite nanoparticles were prepared by chemical co-precipitation technique which is detailed in section 2.1 of chapter 2. Three different ferrofluids, S2, S3 and S4, were employed in this study. The volume fraction of all three ferrofluids was fixed at 0.037 (corresponding to 20 wt.%). Table 6.1 summarizes the obtained results of ferrofluid characterization, details of which can be found in section 2.10 of chapter 2.

Table 6.1: Sample code and characterization details.

Sample code	Avg. Crystallite size [nm]	Most probable hydrodynamic size [nm]	Polydispersity index	Saturation magnetization [emu/g]	Surfactant weight loss [%]
S2	8.3 ± 0.8	18.2 ± 0.9	0.243	66 ± 0.7	21
S3	10.5 ± 1	21 ± 1	0.79	71 ± 0.7	19
S4	7.2 ± 0.7	11.7 ± 0.6	0.238	69 ± 0.7	24

The contact angle measurements were performed as described in chapter 2.

6.3 Results and discussion

6.3.1 Variation of contact angle with strength of magnetic field

Fig. 6.1 shows the image of 10 µl drops of S2, S3 and S4 in the absence and presence of magnetic field.

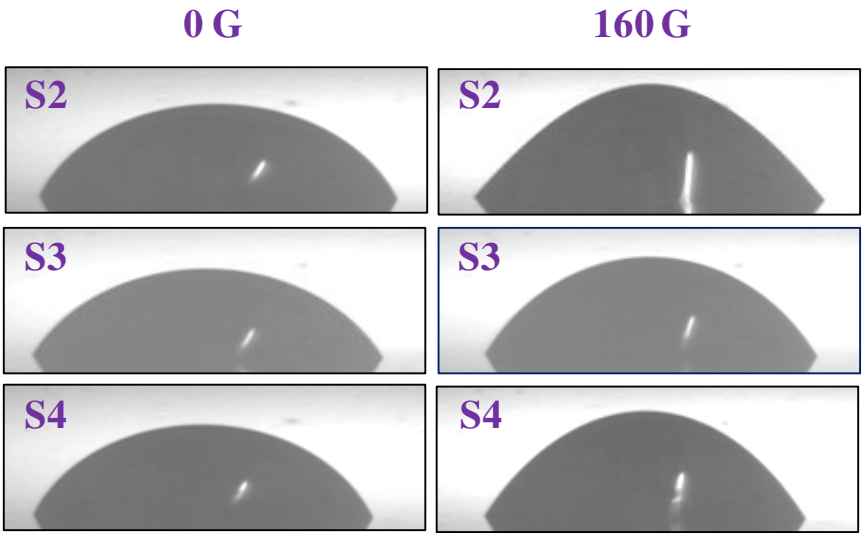

Figure 6.1: Images of sessile droplets of S2, S3 and S4 taken at 0 and 160 G.

Contact angle values of sessile droplets of ferrofluid samples, S2, S3 and S4, as a function of magnetic field strength is shown in **Fig. 6.2**. The zero field contact angle of S2, S3 and S4 are 63 ± 1.3, 59 ± 1.5 and 64 ± 1.2^0, respectively. S3 has a smaller zero field contact angle than S2 and S4 due to the presence of larger aggregates in it. As the magnetic field strength is increased from 0 to 160 G, S2 showed maximum deformation from 63 to 44^0. The contact angle of S4 decreased from 64 to 53^0 as the magnetic field was varied from 0 to 160 G. S3 displayed only a marginal decrease in contact angle from 59^0 at 0 G to 54^0 at 160 G.

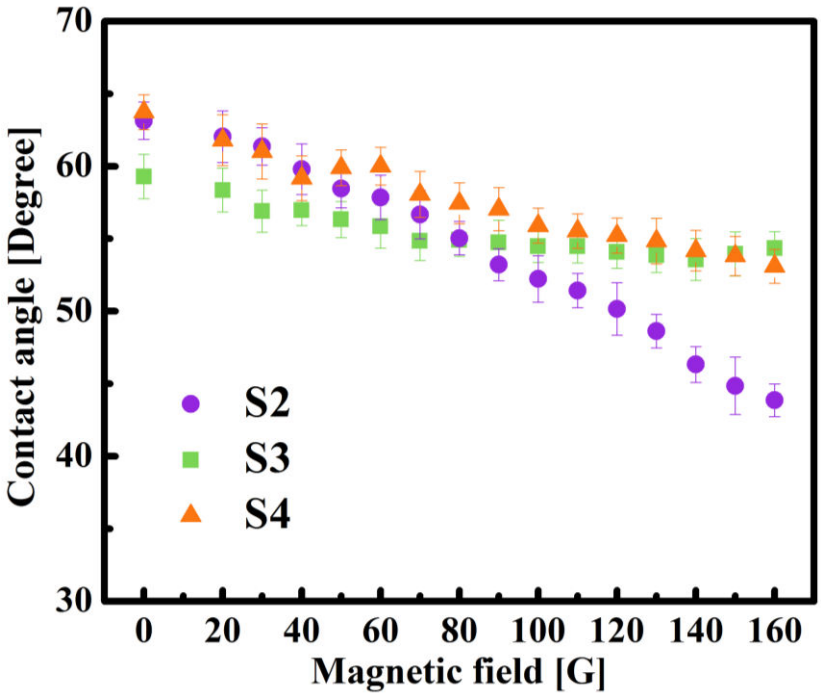

Figure 6.2: Variation of contact angle as a function of strength of applied magnetic field of sessile droplets of S2, S3 and S4.

When a ferrofluid droplet is placed on a smooth non-magnetic surface which is partially wetted by the base fluid, an elliptical meniscus with the semi-minor axis perpendicular to the surface is preferred under the combined action of gravity and surface tension. In the presence of an external magnetic field applied perpendicular to the solid surface on which the ferrofluid droplet is placed, the central portion of the droplet elongates along the field direction due to magnetic stress which is maximum at the tip of the droplet[175]. The external magnetic field alters the curvature and height of the droplet and the final shape will depend on the balance between surface energy and magnetic energy. The surface energy of a prolate ellipsoid is given by

$$E_S = \Upsilon' 2\pi a_d^2 K' [K' + \varepsilon'^{-1} \sin^{-1} \varepsilon'] \tag{6.1}$$

where Υ' is the interfacial tension, K' is the aspect ratio, a_d is the semi-major axis of the ellipsoidal droplet and $\varepsilon' = (1 - K'^2)^{0.5}$ is the eccentricity. The magnetic energy for low field strengths is given by[177]

$$E_M = -\frac{V_{drop} H^2 \mu_1}{8\pi} \frac{1}{\alpha" + n"} \tag{6.2}$$

where V_{drop} is the volume of the elliptical droplet, $\alpha" = \frac{\mu_1}{\mu_2 - \mu_1}$, where μ_1 is the permeability of the surrounding medium and μ_2 is the permeability of the ferrofluid droplet and $n" = K'^2(-2\varepsilon' + ln[(1+\varepsilon')/(1-\varepsilon')])/2\varepsilon'^3$. For certain values of $\frac{\mu_2}{\mu_1}$, ferrofluid droplets displayed discontinuous deformation and exhibited a first order transition accompanied by hysteresis[174]. Ferrofluids with high magnetic susceptibility $(\chi > 20)$ displayed such discontinuous deformation[254]. Experiments by Brancher et al.[178] revealed that droplet of a ferrofluid of low magnetic permeability $(\chi = 0.4)$ showed continuous deformation in the presence of magnetic field while for ferrofluid droplets with higher permeability $(\chi = 5)$ deformation was very small under low magnetic field strength but above a certain magnetic field, a sudden deformation occurred.

6.3.2 Effect of particle size distribution on field induced microstructure

The difference in variation of contact angle in the presence of magnetic field of S2, S3 and S4 is due to difference in particle size distribution and the associated changes in aggregation kinetics. The phase contrast microscopy images of all three ferrofluids taken at field strength of 625 G (**Fig. 6.3**) shows the drastic variation in aggregation kinetics in the samples.

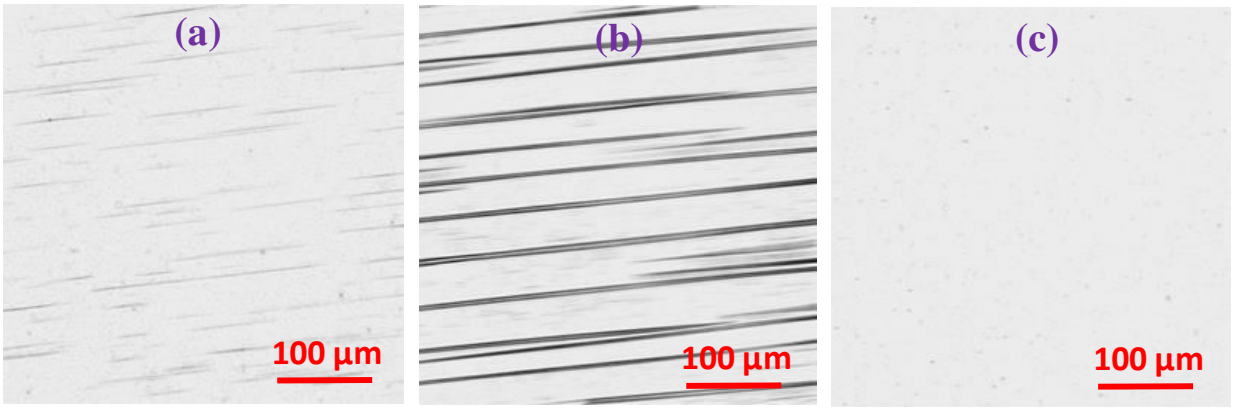

Figure 6.3: Phase contrast microscopy images of (a) S2, (b) S3 and (c) S4 in the presence of magnetic field of strength 625 G.

The volume distribution of S3 showed the presence of large aggregates which results in rapid aggregation and lateral coalescence (zippering) and consequently the number density of aggregates reduces drastically. Vafaei et al.[255] demonstrated that strong particle-base fluid interaction can bring about significant variation in contact angle. When a bottle containing stable ferrofluid is placed near a magnet, the magnetic nanoparticles move closer to the magnet dragging the base fluid along with them. Even when the bottle is upturned along with a magnet placed at its base, the interaction between the base fluid and particles is so strong such that the ferrofluid is able to hold its weight overcoming gravity without phase separating. However, decrease in number density of aggregates brought about by extensive zippering transitions can lead to a drastic decrease in base fluid-particle interaction which could be the cause for the minimal deformation shown by S3. Afkhami et al.[256] observed that the surface tension of certain commercially procured ferrofluids, when exposed to strong magnetic field, was very close to that of the base fluid and this was attributed to the retreat of particles away from the

surface. This supports the minimal deformation displayed by S3 in the presence of magnetic field.

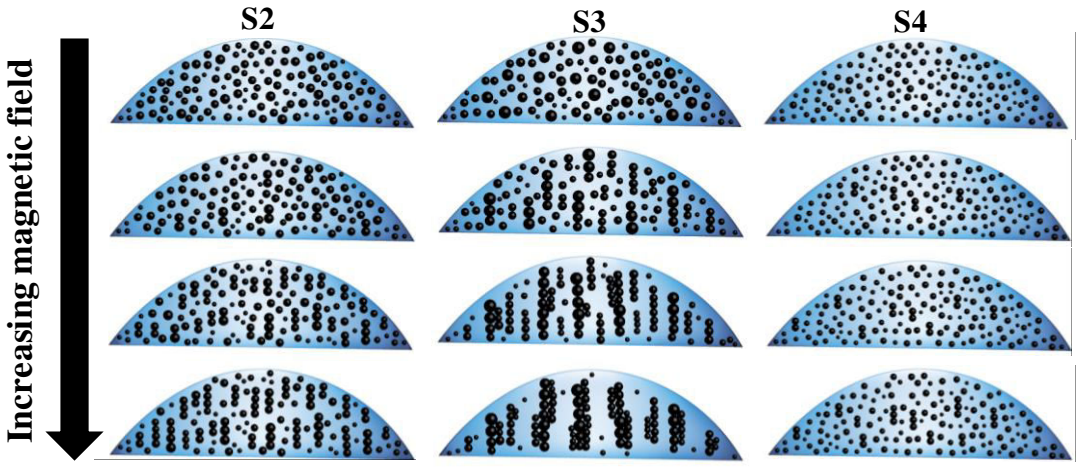

Figure 6.4: Schematic depicting differences in field induced aggregation as a function of magnetic field strength in S2, S3 and S4.

As the amount of smaller particles is more in S4 than S2 and S3, zippering transitions were severely hindered owing to the low dipolar interaction among small particles. Consequently, field induced aggregation is very slow in S4 as most of the aggregates are nanosized as evidenced by phase contrast microscopy images shown in **Fig. 6.3**. S2 contains more number of large particles than S4 but far less than S3 as a result of which the field induced aggregation is not as fast as S3 and zippering transitions are not hampered as much as in S4 which is evident from the presence of a few micron sized aggregates seen in the microscopy images. Hence in S2 the number density of chains is not too low and at the same time aggregation increases significantly with increasing field strength resulting in appreciable change in droplet profile with increasing field strength. A schematic showing the difference in aggregation in S2, S3 and S4 is shown in **Fig. 6.4**.

6.4 Conclusions

The effect of particle size distribution on field induced aggregation and field induced deformation of sessile ferrofluid droplets on a solid substrate was probed. S2 displayed maximum deformation with increasing magnetic field strength from 63^0 at 0 G to 44^0 at 160 G. S3 showed minimum deviation from 59 to 54^0 as magnetic field was increased from 0 to 160 G. S4 displayed a decrease in contact angle from 64 to 53^0 as the magnetic field was varied from 0 to 160 G. In S3 the significant fraction of large particles increased the rate of aggregation kinetics by lowering the energy barrier for chain formation and lateral coalescence resulting in the formation of large micron sized aggregates. Extensive zippering transitions reduced the number density of aggregates drastically resulting in a lower aggregate-base fluid interaction. Hence, only a slight decrease in contact angle was observed at low field strengths beyond which there was no significant variation. In S4 aggregation kinetics was very slow owing to the presence of significant amount of small particles that is detrimental to chain formation and lateral coalescence. As a result, even though number density of aggregates was high, S4 showed a small but steady decrease in contact angle with increasing field strength. In S2, field induced aggregation was faster than S4 but at the same time the number density of chains was high enough so as to not mask the interaction between the aggregates and the base fluid. Hence, significant variation in contact angle was observed in S2.

Chapter 7 Conclusions and recommendations for future work

7.1 Summary and conclusions

The effect of field induced aggregation dynamics on thermal, rheological and wetting properties of oil-based ferrofluids that are similar in chemical composition and volume fraction but differ in their size distribution was studied systematically. The important results are summarized below.

Particle size distribution was found to drastically affect field tunable thermal conductivity and rheology of ferrofluids. Ferrofluid containing nanoparticles with most probable hydrodynamic size 11.6 nm and PDI 0.225 gave the highest enhancement in thermal conductivity with minimal viscosity enhancement while another ferrofluid composed of particles with most probable hydrodynamic size 21 nm and PDI 0.79 did not show notable enhancement in field tunable thermal conductivity but displayed pronounced increase in viscosity with increasing field strength. This drastic difference in thermal and rheological properties of ferrofluids is due to differences in field induced aggregation brought about by difference in particle size distribution. Narrow size distribution, without large aggregates, results in the occurrence of nucleation, the first step towards chain/column formation, over longer time scales and at higher field strengths owing to larger energy barrier height for aggregation because of lower dipolar interaction. Additionally, presence of modest amount of smaller particles prevented extensive zippering transitions. Thereby, the reduction of heat conducting pathways is averted. In the optical microscopy images, even for field strengths as high as 625 G, observable aggregates were absent in ferrofluids with narrow size distribution without large aggregates, confirming that most of the aggregates were nanosized. At the same time, in such systems

notable viscosity enhancement was not observed as the field induced aggregates are fine. In ferrofluid systems with sizeable portion of larger particles, the nucleation stage is very short as the large particles themselves act as nucleation centers and micron sized aggregates were observed even at low field strengths in the optical microscopy images. Extensive zippering transitions lead to drastic decrease in the number density of aggregates and thermal conductivity did not show substantial improvement with increasing magnetic field strength. However, owing to the thick gap spanning columnar aggregates, viscosity enhancement in the polydisperse system was high with measurable yield stress. These results imply that by tailoring the particle size distribution efficient heat transfer can be achieved without viscosity enhancement and ferrofluids can serve as excellent coolants without increasing pumping power.

Magnetic field ramp rate is one of the factors influencing aggregation kinetics that has not received much attention. Faster magnetic field ramps results in simultaneous formation of large number density of fine aggregates which was found to improve field tunable thermal conductivity of ferrofluids owing to the large number density of aggregates. Slower ramps on the other hand, resulted in the formation of thicker aggregates via extensive zippering transitions than a fast ramp, leading to drastic reduction in the number density of aggregates. On sudden exposure to magnetic field, particularly for higher strengths, substantial improvement in thermal conductivity was observed in initially, though with time zippering transitions reduced the number density of chains and thermal conductivity decreased. However, for fast ramps, even after a time period of 30 min., thermal conductivity was still higher than the corresponding value obtained for a slow ramp rate. For higher field strengths, faster ramps was found to be more beneficial for thermal transport and for avoiding the decrease in thermal conductivity with time, alternate magnetic field on-off cycles was found to be effective. Additionally, with faster ramps

thermal conductivity in a system with moderate amount of larger particles can be significantly improved from the values obtained during slower ramps.

The applied magnetic field ramp rate, in addition to influencing field tunable thermal transport, significantly impacted rheological properties of ferrofluids as the microstructure was found to be very different for slow and fast field quenches. Slower field quench rates resulted in a microstructure of higher yield stress composed of very coarse long aggregates while fast quenches led to the formation of thinner and shorter aggregates, denied of the time to settle into lower energy states and thereby existing in a frustrated metastable configuration like a repulsive glass. For the fastest field quench the frequency sweep measurement showed a fast relaxation which is tentatively assigned to local mobility of aggregates in a spatially heterogeneous configuration. For slower ramp durations, such a relaxation could not be seen within the accessible experimental window, though there are clear indications of imminent crossovers at lower frequencies. Fast field quench leads to the buildup of internal stresses, giving rise to faster dynamics, and hence relaxation is shifted to lower frequency with increase in quench duration. In the presence of magnetic field, under fast field quenches, ferrofluid was found to disobey time translational invariance and underwent aging with continuous evolution of microstructure as a result of which strain response to constant stress and creep compliance became a function of the waiting time before the beginning of rheological test. However, when the curves are scaled with respect to an effective time domain, time translational invariance was recovered, just like other soft glassy materials. For longer ramp duration, the microstructure is closer to equilibrium and hence the exponent used for scaling the time domain to an effective time domain was found to be smaller than for faster ramps.

Thesis Highlight

Name of the Student: **Sithara Vinod**
Name of CI: **Indira Gandhi Centre for Atomic Research** Enrolment No.: **PHYS 02 2014 04 001**
Thesis Title: **Studies on the effect of magnetic field induced aggregation on physical properties of ferrofluids**
Discipline: **Physical Sciences** Sub-Area of Discipline: **Soft condensed matter**
Date of viva voce: **21/02/2020**

Ferrofluid, a smart magnetic colloid, alters its physical properties when exposed to magnetic field which inspired many innovative applications. The change in physical properties is brought about by field induced reversible aggregation of magnetic nanoparticles and a thorough understanding of this aggregation dynamics is a prerequisite to effective utilization of these fluids for various applications. The effect of particle size distribution on field induced aggregation dynamics and subsequent changes in thermal, rheological and wetting properties was systematically probed in this thesis.

Experimental results showed that differences in particle size distribution drastically affected the physical properties of ferrofluids in the presence of magnetic field. Ferrofluids containing large particles displayed very fast aggregation kinetics leading to the formation of thick and long field induced aggregates via extensive zippering transitions, thus drastically reducing the number density of aggregates which was found to be detrimental to heat transport but led to very high viscosity enhancement. On the other hand, ferrofluids with narrow size distribution, without large aggregates, displayed significant enhancement in thermal conductivity in the presence of magnetic field with negligible viscosity enhancement, owing to the large number density of fine aggregates, since in the absence of large particles tip-to-tip aggregation and zippering transitions occur over longer timescales and at higher field strengths due to the low dipolar interaction between smaller particles. Figure 1 shows a schematic representation of field induced microstructure that is favorable and detrimental to heat transport (Fig. 1 (a) and (c), respectively) and viscosity enhancement (Fig. 1 (d) and (b), respectively). Additionally, aggregation kinetics affected wetting properties of sessile ferrofluid droplets in the presence of magnetic field. Significant decrease in contact angle with increasing magnetic field was observed for ferrofluids without large aggregates as the number density of aggregates are high enough to ensure strong particle-base fluid interaction.

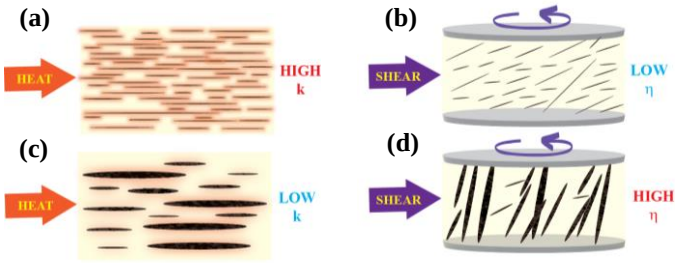

Fig. 1 Schematic representing the field induced microstructure (a) favorable and (c) detrimental to heat transport and the microstructure that is (b) detrimental and (d) favorable for viscosity enhancement.

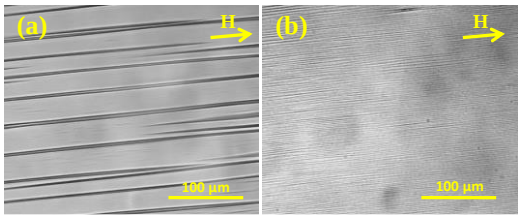

Fig. 2 Phase contrast microscopy images of field induced microstructure of a ferrofluid subjected to (a) slow and (b) fast magnetic field ramp rate to 630 G.

Magnetic field ramp rate was found to have a profound influence on thermal and rheological properties of ferrofluids. Microscopy images in Fig. 2 shows the difference in microstructure of ferrofluid exposed to slow and fast field ramps. Faster ramps result in simultaneous formation of large number density of aggregates which was found to be beneficial for heat transport (See Fig. 3). Under fast field quenches at sufficiently high field strengths, ferrofluids exhibit aging and glassy dynamics owing to structural arrest of field induced aggregates.

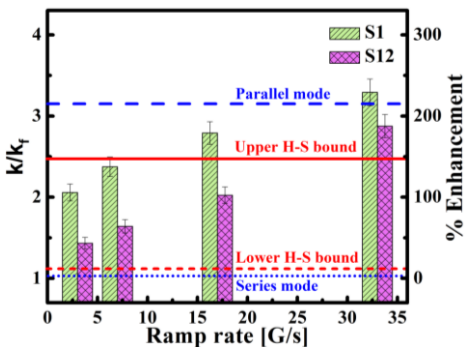

Fig. 3 Variation of k/k_f as a function of magnetic field ramp rate for 200 G. The solid and dashed red lines indicate the upper and lower H-S bounds, respectively and the dashed and dotted blue lines indicate k/k_f calculated using parallel and series models of conduction, respectively.

The findings reported in this thesis will provide better insight into aggregation dynamics and its effect on physical properties of ferrofluids that will aide in better utilization of these fluids in applications.

Thesis Highlight

Name of the Student: **Sithara Vinod**
Name of CI: **Indira Gandhi Centre for Atomic Research** Enrolment No.: **PHYS 02 2014 04 001**
Thesis Title: **Studies on the effect of magnetic field induced aggregation on physical properties of ferrofluids**
Discipline: **Physical Sciences** Sub-Area of Discipline: **Soft condensed matter**
Date of viva voce: **21/02/2020**

Ferrofluid, a smart magnetic colloid, alters its physical properties when exposed to magnetic field which inspired many innovative applications. The change in physical properties is brought about by field induced reversible aggregation of magnetic nanoparticles and a thorough understanding of this aggregation dynamics is a prerequisite to effective utilization of these fluids for various applications. The effect of particle size distribution on field induced aggregation dynamics and subsequent changes in thermal, rheological and wetting properties was systematically probed in this thesis.

Experimental results showed that differences in particle size distribution drastically affected the physical properties of ferrofluids in the presence of magnetic field. Ferrofluids containing large particles displayed very fast aggregation kinetics leading to the formation of thick and long field induced aggregates via extensive zippering transitions, thus drastically reducing the number density of aggregates which was found to be detrimental to heat transport but led to very high viscosity enhancement. On the other hand, ferrofluids with narrow size distribution, without large aggregates, displayed significant enhancement in thermal conductivity in the presence of magnetic field with negligible viscosity enhancement, owing to the large number density of fine aggregates, since in the absence of large particles tip-to-tip aggregation and zippering transitions occur over longer timescales and at higher field strengths due to the low dipolar interaction between smaller particles. Figure 1 shows a schematic representation of field induced microstructure that is favorable and detrimental to heat transport (Fig. 1 (a) and (c), respectively) and viscosity enhancement (Fig. 1 (d) and (b), respectively). Additionally, aggregation kinetics affected wetting properties of sessile ferrofluid droplets in the presence of magnetic field. Significant decrease in contact angle with increasing magnetic field was observed for ferrofluids without large aggregates as the number density of aggregates are high enough to ensure strong particle-base fluid interaction.

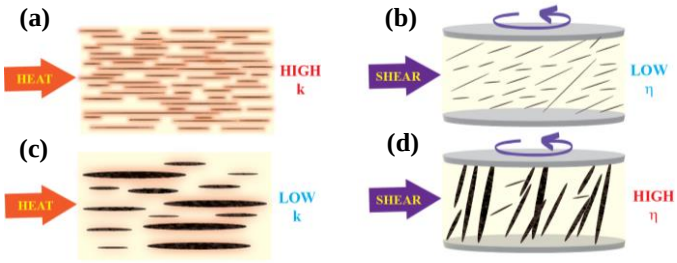

Fig. 1 Schematic representing the field induced microstructure (a) favorable and (c) detrimental to heat transport and the microstructure that is (b) detrimental and (d) favorable for viscosity enhancement.

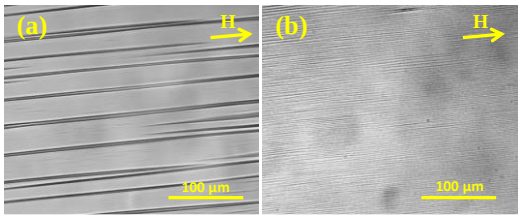

Fig. 2 Phase contrast microscopy images of field induced microstructure of a ferrofluid subjected to (a) slow and (b) fast magnetic field ramp rate to 630 G.

Magnetic field ramp rate was found to have a profound influence on thermal and rheological properties of ferrofluids. Microscopy images in Fig. 2 shows the difference in microstructure of ferrofluid exposed to slow and fast field ramps. Faster ramps result in simultaneous formation of large number density of aggregates which was found to be beneficial for heat transport (See Fig. 3). Under fast field quenches at sufficiently high field strengths, ferrofluids exhibit aging and glassy dynamics owing to structural arrest of field induced aggregates.

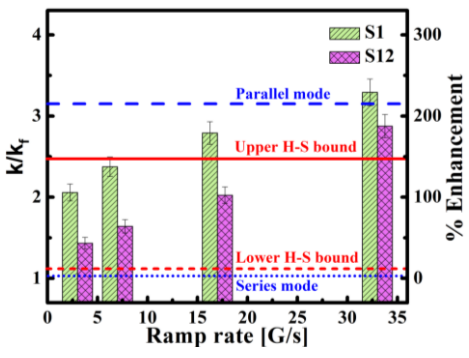

Fig. 3 Variation of k/k_f as a function of magnetic field ramp rate for 200 G. The solid and dashed red lines indicate the upper and lower H-S bounds, respectively and the dashed and dotted blue lines indicate k/k_f calculated using parallel and series models of conduction, respectively.

The findings reported in this thesis will provide better insight into aggregation dynamics and its effect on physical properties of ferrofluids that will aide in better utilization of these fluids in applications.